Visual Workflows for Oil and Gas Exploration

Thesis by

Thomas Höllt

In Partial Fulfillment of the Requirements

For the Degree of

Doctor of Philosophy

King Abdullah University of Science and Technology, Thuwal,

Kingdom of Saudi Arabia

April 2013

The thesis of Thomas Höllt is approved by the examination committee

ABSTRACT

Visual Workflows for Oil and Gas Exploration

Thomas Höllt

The most important resources to fulfill today's energy demands are fossil fuels, such as oil and natural gas. When exploiting hydrocarbon reservoirs, a detailed and credible model of the subsurface structures to plan the path of the borehole, is crucial in order to minimize economic and ecological risks. Before that, the placement, as well as the operations of oil rigs need to be planned carefully, as off-shore oil exploration is vulnerable to hazards caused by strong currents. The oil and gas industry therefore relies on accurate ocean forecasting systems for planning their operations.

This thesis presents visual workflows for creating subsurface models as well as planning the placement and operations of off-shore structures.

Creating a credible subsurface model poses two major challenges: First, the structures in highly ambiguous seismic data are interpreted in the time domain. Second, a velocity model has to be built from this interpretation to match the model to depth measurements from wells. If it is not possible to obtain a match at all positions, the interpretation has to be updated, going back to the first step. This results in a lengthy back and forth between the different steps, or in an unphysical velocity model in many cases. We present a novel, integrated approach to

interactively creating subsurface models from reflection seismics, by integrating the interpretation of the seismic data using an interactive horizon extraction technique based on piecewise global optimization with velocity modeling. Computing and visualizing the effects of changes to the interpretation and velocity model on the depth-converted model, on the fly enables an integrated feedback loop that enables a completely new connection of the seismic data in time domain, and well data in depth domain.

For planning the operations of off-shore structures we present a novel integrated visualization system that enables interactive visual analysis of ensemble simulations used in ocean forecasting, i.e, simulations of sea surface elevation. Changes in sea surface elevation are a good indicator for the movement of loop current eddies. Our visualization approach enables their interactive exploration and analysis. We enable analysis of the spatial domain, for planning the placement of structures, as well as detailed exploration of the temporal evolution at any chosen position, for the prediction of critical ocean states that require the shutdown of rig operations. We illustrate this using a real-world simulation of the Gulf of Mexico.

ACKNOWLEDGEMENTS

This thesis would not have been possible without the efforts of many people and institutions. The majority of the work resulting in this thesis and the related publications has been carried out at the center for Geometric Modeling and Scientific Visualization at the King Abdullah University of Science and Technology. In addition, before moving to KAUST, the first year of this work was conducted ad the VRVis Research Center.

Foremost, I want to thank my advisor Markus Hadwiger for giving me the opportunity to pursue a PhD, first at the VRVis and then at KAUST and for his continuous support over the last four years. Helmut Pottmanns' and the whole GMSV staffs' efforts to build the center from ground up and making it a great place to conduct research cannot be valued highly enough. I am extremely grateful to Helmut Doleisch and Chuck Hansen for giving me the opportunity to escape the desert heat and providing me with summer internships at SimVis and the SCI Institute, respectively.

None of my publications would have been possible without the help of my co-authors and project partners; Johanna Beyer, Guoning Chen, Helmut Doleisch, Wolfgang Freiler, Laura Fritz, Ganesh Gopalakrishnan, Fritz M. Gschwantner, Markus Hadwiger, Chuck Hansen, Gabor Heinemann, Ibrahim Hoteit, Ahmed Magdy, Philipp Muigg and Daniel Patel.

Working at VRVis, SimVis, SCI and KAUST over the last four years, I always found a great atmosphere, therefore I'd like to thank all my previous and current colleagues, especially Harald, I remembered your name, Matthias, Michael, Thomas, Waltraud, Wolfgang and the rest of the render chat for a continuous flow of entertainment, Fritz, Laura, Philipp, Wolfgang, thanks for the billiard lessons, Johanna, for being humble enough to not talk about her degrading tennis victories, Peter, I think we can go even smaller, Tom, Markus and Mathias.

Finally, I'd like to express my sincere gratitude to my family and friends back home for their continuous support.

[illegible]

Thuwal, KSA

April 2013

TABLE OF CONTENTS

Examination Committee Approval **2**

Copyright **3**

Abstract **4**

Acknowledgements **6**

List of Figures **10**

List of Tables **12**

1 Introduction **14**

1.1 Contributions of this Thesis 15

1.1.1 Subsurface Modeling and Seismic Visualization 16

1.1.2 Visual Analysis of Uncertainties in Ocean Forecasts 17

1.2 Subsurface Modeling 17

1.3 Analysis of Ocean Forecasts 22

2 Related Work **24**

2.1 Subsurface Modeling and Seismic Interpretation 24

2.2 Volume Visualization for Seismic Data 27

2.3 Image and Volume Segmentation 29

2.4 Volume Deformation 31

2.5 Ensemble Visualization 32

2.6 Uncertainty Visualization 33

3 Visual Subsurface Modeling **35**

3.1 Current Practice 36

3.1.1 Weaknesses and Proposed Enhancements 38

3.2 Joint Time/Depth Domain Visualization 39

3.2.1 Rendering Pipeline 41

3.2.2 On the Fly Deformation 44
3.2.3 Performance 47
3.3 Prism-Based Workflow 50
3.4 Horizon Extraction using Global Optimization 52
3.4.1 Requirements for Horizon Extraction 53
3.4.2 Local Horizon Extraction: Tracing Diffusion Tensors 55
3.4.3 Minimum Cost Circulation Network Flow 60
3.4.4 Extracting the Surface from the Saturated Graph 66
3.4.5 Cost Function 67
3.5 Results 74
3.5.1 Evaluation 74
3.6 Conclusion 84

4 Visual Parameter Space Exploration for Horizon Extraction 86
4.1 Ensemble Computation 87
4.2 Statistical Analysis 87
4.3 Ensemble Visualization 89
4.4 Computation and Visualization Pipeline 94
4.5 Results 98
4.6 Conclusion 103

5 Enhancing Seismic Visualization 104
5.1 Horizon Enhancing Shading 104
5.2 Exploded Views 109

6 Visual Analysis of Uncertainties in Ocean Forecasts 114
6.1 Ocean Forecast Simulation 115
6.2 Application Framework 118
6.3 Statistical Analysis 119
6.4 Ensemble Visualization 120
6.5 Computation and Visualization Pipeline 124
6.5.1 Performance 126
6.6 Results 129
6.6.1 Placement Planning 130
6.6.2 Final Placement / Operational Phase 132
6.7 Conclusion 134

7 Summary and Discussion **135**

References **138**

Appendices **150**

LIST OF FIGURES

1.1 Illustration of subsurface structures in the time domain and after depth conversion. 21

2.1 Illustration of the differences between shortest paths and minimal surfaces. 31

3.1 Conventional and proposed workflows for subsurface modeling. . . 37
3.2 Joint time/depth domain views. 40
3.3 The rendering pipeline for joint time/depth interaction. 41
3.4 Illustration of the surface deformation with computation of deformed boundaries. 45
3.5 Pseudo code for live volume deformation. 47
3.6 Volume renderings of the two datasets used for the performance measurements. 48
3.7 The original prism unfolded into a single slice. 51
3.8 Different steps through the diffusion based tracing pipeline. 56
3.9 Results of the different seismic horizon tracing methods we have implemented. 58
3.10 Correspondence between picture elements and items in the primal and dual graphs. 62
3.11 The horizon extraction computation pipeline. 64
3.12 Dual edges in 2D and 3D. 68
3.13 Comparison of the cost obtained via the components of the snappiness term. 70
3.14 Comparison of three horizon patches computed using our algorithm. 75
3.15 Screenshot of our subsurface modeling application. 76
3.16 Comparison of the horizons extracted during the expert evaluation. . 80
3.17 Results of the evaluation, compared to ground truth data. 81
3.18 Screenshot of the $1422 \times 667 \times 1024$ voxel dataset. 83

4.1 Cut sections of all surfaces of one ensemble rendered into a single slice view with reduced opacity. 89
4.2 Comparison of the maximum likelihood surface with synthetic mean surface of a seismic horizon ensemble. 91
4.3 Visualization of a horizon ensemble. 93
4.4 Pipeline for extracting and visualizing seismic horizon ensembles. . . 94
4.5 Comparison of the visualization of uncertain areas in an extracted horizon, using the cost and the variance of an ensemble. 99
4.6 Exploration of the parameter space of a seismic horizon ensemble. . 100
4.7 Different statistical properties extracted from a seismic horizon ensemble. 102

5.1 Comparison of different kernel sizes for the cost modulated shading. 105
5.2 An example of a visualization of a seismic cube highlighting reflections of positive amplitude. 106
5.3 Horizon extracted using the horizon enhancing shading. 107
5.4 Renderings with different parameters for cost function prototyping. . 108
5.5 Exploded view and clipping of an interpreted seismic cube. 110
5.6 Exploded view of an interpreted seismic cube. 111

6.1 The Gulf of Mexico simulation area covered by the presented dataset. 115
6.2 Overview of the ocean forecast visualization system. 118
6.3 Iso contouring and pdf volume rendering. 121
6.4 The Time-Series View in detail. 122
6.5 The glyph developed for visualizing the ensemble properties at a defined spatial position. 123
6.6 The extensions to the computation and rendering pipeline presented in Section 4.4. 124
6.7 Walkthrough for the placement planning for off-shore structures. . . 131
6.8 Comparison of the time series for two very close positions. 133

7.1 Different fault types. 136

LIST OF TABLES

3.1 Textures and buffers needed in our pipeline. 42
3.2 Surface deformation performance for the on the fly depth conversion. 49
3.3 Performance comparison of the live depth conversion. 50
3.4 Timings for the interpretation process. 82

5.1 Performance for horizon enhancing rendering vs. Phong shading. . . 109
5.2 Performance comparison of the exploded views. 113

6.1 Comparison of computation times between GPU (CUDA) and CPU. 127
6.2 Statistic computation times for 50 and 500 surfaces. 128

Chapter 1

Introduction

Most of today's energy demand is fulfilled by fossil fuels, and even though alternative and renewable energy sources are getting more important, the U.S. Energy Information Administration predicts that oil and gas will still account for more than 50% of the worldwide marketed energy in 2035 [104]. For efficient and safe operations the oil and gas industry relies strongly on the correct analysis of large amounts of data collected in various fields. Seismic surveys, resulting in large amounts data of diverse kinds, are conducted to understand the properties of the subsurface and locate oil and gas reservoirs. Based on these data, simulations are computed, for example, to study the flow of liquids in the subsurface, to predict the effects of exploiting an oil reservoir. But also in less obvious areas scientific computing is used to aid operations. Ocean forecasts are simulated to predict dangerous situations, requiring off shore rigs to be shut down. All these problems can profit from visual, interactive workflows. In this thesis we present research conducted to improve two of these workflows.

We present an interactive workflow for subsurface modeling in Chapter 3. The workflow is based on a novel joint time/depth visualization technique, to integrate data recorded in different domains, time and spatial depth, to guide extraction of subsurface layers from seismic reflection tomography data. We extend this work by a visual parameter space exploration technique for ensembles of extracted seismic horizons (Chapter 4) and techniques to enhance the visualization of the dense and noisy seismic reflection data (Chapter 5).

In Chapter 6 we present a novel, visualization driven workflow for planning the placement and operations of off-shore structures. Based on ensemble simulations of the ocean surface, the risk for an existing structure or an area for potential placement, can be predicted.

We implemented both workflows in a flexible visual analysis framework. We use multiple linked views, specific to the different applications, to present the data to the user and allow easy interaction and verification of results. The framework is integrated as a plugin into the SimVis framework [20].

Structure

In the remainder of this chapter we present the contributions of this thesis (Section 1.1) and give detailed introductions to the two application areas, subsurface modeling and the analysis of ocean forecasts (Section 1.2 and 1.3, respectively). We present the related work to both fields combined in Chapter 2. In Chapter 3 we present our workflow for subsurface modeling. Our technique for visual parameter space exploration of horizon ensembles is presented in Chapter 4. In Chapter 5 we present techniques to enhance the visualization seismic reflection data. Our visual workflow for the analysis of ocean forecasts is presented in Chapter 6. Finally we conclude with a discussion of the contributions and open questions in Chapter 7.

1.1 Contributions of this Thesis

This thesis introduces novel workflows for subsurface modeling and the analysis of ocean forecasts. Section 1.1.1 presents the contributions in the field of subsurface modeling and seismic visualization in detail. The details for the visual analysis of uncertainties in ocean forecasts are given in Section 1.1.2.

1.1.1 Subsurface Modeling and Seismic Visualization

We propose a novel workflow for subsurface modeling based on well positions and joint time-depth domain views (Chapter 3). We triangulate the spatial positions of all available wells, which divides the volume into a set of triangular prisms. Instead of interpreting the volume slice-by-slice in 2D, we propose performing full 3D seismic interpretation, going from prism to prism. The part of a horizon intersecting a given prism can be extracted by specifying as little as a single seed point, using global energy minimization techniques to compute a horizon surface of minimal "cost". We combine very fast 2D minimal cost path tracing for determining horizon intersections along the faces of the prisms resulting from well log triangulation with subsequent 3D minimal cost surface computation, which is constrained by the 2D contours on the prism faces. By combining the optimal surfaces from the individual prisms, we receive a piecewise globally optimized horizon. Extracting the horizon in a piecewise manner allows for an interactive algorithm which gives the user full control over adjusting the surface by setting an arbitrary number of constraints, forcing the surface to pass through specified locations. Our novel joint time/depth domain workflow, which integrates horizon extraction, velocity modeling and on the fly depth conversion, for the first time enables depth-domain ground-truth data to be integrated directly into a time domain-based workflow. Therefore well data can be used during the interpretation process to constrain the surface extraction.

Furthermore we present a framework for interactively analyzing the parameter space of the presented surface extraction technique (Chapter 4). We automatically sample the parameter space of the cost function used for horizon extraction, to compute ensembles of horizon surfaces. We provide an interactive system that enables analysis and visualization of the extracted ensemble data and facilitates real time exploration of the parameter space of these data.

Finally we present a novel shading technique, aimed at highlighting horizon structures in seismic volume data, as well as a technique for single pass exploded views based on extracted horizons (Chapter 5).

1.1.2 Visual Analysis of Uncertainties in Ocean Forecasts

We present a GPU-based interactive visualization system for the exploration and analysis of ensemble heightfield data, with a focus on the specific requirements of ocean forecasts. Based on an efficient GPU pipeline we perform on-the-fly statistical analysis of the ensemble data, allowing interactive parameter exploration. We present a novel workflow for planning the placement and operation of off-shore structures needed by the oil and gas industry. While we focus on the visualization and analysis of ocean forecast data, the presented approach could also be used for the exploration of heightfield ensembles from other areas, such as weather forecasting or climate simulation.

1.2 Subsurface Modeling

For the planning of production wells to drill into oil and gas reservoirs, one has to have an exact model of the subsurface structures. These include the different geological layers, the boundaries between these layers (*seismic horizons*), but also *faults*, as well as other structures. The basis for creating such a subsurface model is usually a *seismic survey*. A typical survey contains 3D seismic reflection data(*seismic cubes*), as well as additional data such as *well logs* and *well tops*.

Seismic Cube

The Seismic Cube is a regular grid of scalar values. It is acquired by sending seismic waves into the ground. At a seismic horizon, part of the waves will be reflected, while others will proceed. The reflected waves are then measured on the ground using a 2D grid of *geophones*. The result is a set of 1D traces along the z-axis, one for each geophone, with z corresponding to the two-way travel time of the seismic wave, and $f(z)$ being the measured amplitude. The seismic traces are then usually *time-* or *depth-migrated*. In this process, the actual lateral positions of the reflection events in the (x, y)-plane have to be computed, as in the original data one does not know from which direction the event actually arrived at the geophone. For a 3D survey, the migrated 1D traces are combined to form a 3D seismic cube. The dimensions of the resulting volume are lateral distances for the geophone grid, and time or depth on the z-axis, depending on the migration technique. Even though the depth migration delivers depth on the z-axis, this value does not directly correspond to actual spatial depth in the real world, because the so-called *provelocities* used in the depth-migration do not account for the horizontal energy in the seismic waves [22].

Well Data

Two kinds of data are aquired from exploration wells: *Well logs* are 1D datasets, containing detailed records of certain properties of the subsurface structures at the drill hole. Logs can be either geological or geophysical. The former are acquired by visually or chemically inspecting samples brought to the surface, but also contain live drilling parameters such as the speed at which the drill bit deepens the borehole (i.e., the rate of penetration), the latter by lowering a measurement device into the borehole. A comprehensive survey of a drilling usually contains several well logs, geological as well as geophysical. Typical properties besides the rate of penetration are for example weight, porosity or resistivity. *Well tops* contain exact information on the position of subsurface layer boundaries. While well log data is usually a continuous 1D data stream along the borehole, well top data consists only of a few discrete samples per well. A single well top is simply a point in 3D marking the depth for a defined horizon at the included (x, y)-position. Both, well logs as well as well tops, can function as ground truth data when interpreting the seismic cube. Well log and well top data come in three different types: (1) measured in spatial depth at the drill holes, (2) measured in spatial depth, and converted to the time- or depth-migration domain, or (3) measured directly in the time domain. Unlike well data available in the time domain, the much more common and also more accurate data only available in the spatial depth domain cannot be used directly for interpreting a time-migrated seismic measurement. In the conventional workflow for seismic interpretation, after finishing the interpretation, the extracted features are converted into the spatial depth domain. Only then can the interpretation be matched to the ground truth data available only in the spatial depth domain.

Seismic Horizons

Seismic horizons define the boundaries of subsurface layers. In the seismic cube they are represented by bands of locally extremal values, whereas most other structures like *faults* are primarily defined by their interaction with horizons.

Seismic Interpretation

The extraction of seismic horizons is one of the main tasks when interpreting the seismic cube to build a model of the subsurface structures. In most cases, the seismic interpretation is not based solely on the seismic cube. Usually, well log and top data from physical drillings provide additional information. However, since the seismic cube and the well data are usually in different domains the well data can not be used directly during the interpretation process, but only after a complete interpretation path with subsequent *depth conversion*. Interpreting the seismic cube is a cumbersome, time-consuming process. The data is dense, hard to visualize in 3D, noisy, and ambiguous. It may happen that after hours of interpretation work it becomes apparent during time-depth conversion that large parts of the volume were misinterpreted due to a single wrong decision in what seems to be a branching horizon. In current practice, which is mainly based on manual inline- and crossline-slice inspection, this is very tedious, as it requires manual correction of multiple slices. Additionally, these slices need to be adjusted according to well log information which usually is only available for very few slices, and might be located between interpreted slices where no interpretation has been performed.

Depth Conversion

Depth Conversion is the process of computing actual spatial depths for seismic structures. Etris et al. [22] explain the need for depth conversion of the seismic interpretation and why depth migration, even though resulting in a seismic cube in the depth domain is not sufficient to get a good subsurface model. Figure 1.1 illustrates why depth conversion is necessary to get a correct impression of the subsurface structures and why structural interpretation is hard in the time domain.

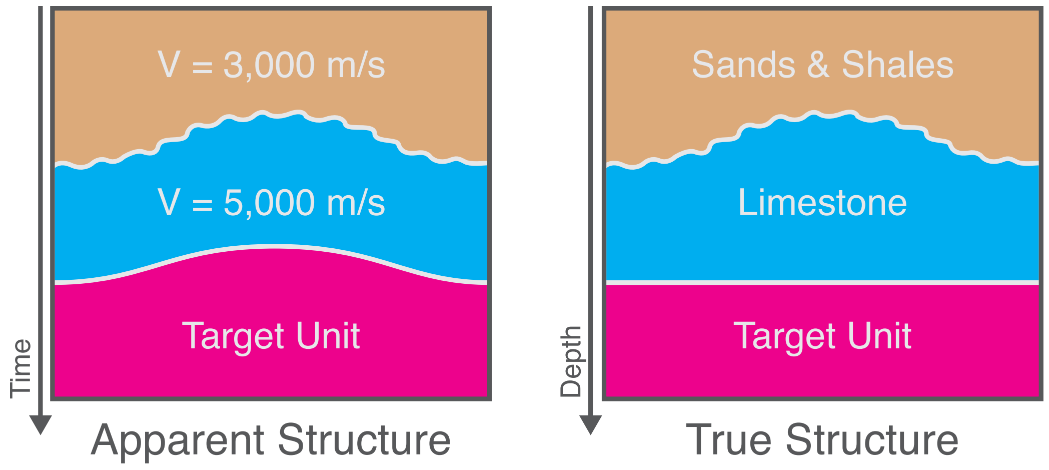

Figure 1.1: Illustration of subsurface structures in the time domain (right) and after depth conversion (left). Image adapted from Etris et al. [22].

While in the time domain it appears that the bottom layer is bulged, in the depth converted model it becomes apparent that it is actually flat and the bulging in the time domain is caused by the different velocities of the layers on top. The depth conversion is carried out using the extracted horizons and a velocity model. Each subsurface layer is assumed to consist of a single material only, or an equal distribution of a mixture of materials. This makes it possible to assign an average velocity value to each layer. In the same way subsurface layers do not intersect, neither do their boundaries. Here, we assume that boundaries do not fold over, and thus can be defined as a function over the lateral domain, i.e., a heightfield. According to our domain expert collaborators, this is a reasonable assumption that subsumes the largest part of seismic interpretation work. These two constraints make it possible to interpret the depth conversion process as a piecewise linear scaling of layers along the z-axis.

1.3 Analysis of Ocean Forecasts

Oil exploration in the deep Gulf of Mexico is vulnerable to hazards due to strong currents at the fronts of highly non-linear warm-core eddies [108]. The dynamics in the Gulf of Mexico are indeed dominated by the powerful northward Yucatan Current flowing into a semi-enclosed basin. This current forms a loop, called the Loop Current, that exits through the Florida Straits, and in turn merges with the Gulf Stream. At irregular intervals, the loop current sheds large eddies that propagate westward across the Gulf of Mexico. This eddy shedding involves a rapid growth of non-linear instabilities [17], and the occasional eddies detachment and reattachment make it very difficult to clearly define, identify, monitor, and forecast an eddy shedding event [16, 18, 40].

The predictability of loop current shedding events in the Gulf of Mexico poses a major challenge for the oil and gas industry operating in the Gulf. The presence of these strong loop currents with speeds exceeding 1 $m\,s^{-1}$ potentially causes serious problems and safety concerns for the rig operators. Millions of dollars are lost every year due to drilling downtime caused by these powerful currents. As oil production moves further into deeper waters, the costs related to strong current hazards are increasing accordingly, and accurate three-dimensional forecasts of currents are needed. These can help rig operators to avoid some of these losses through better planning, and avoid potentially dangerous scenarios. A three-dimensional ocean forecasting system for the Gulf of Mexico therefore becomes crucial and highly desired by the oil and gas industry, where accurate loop current forecasts over a time frame of one to two weeks provide a reasonable time window for planning the drilling operations.

Developing efficient tools to visualize and clearly disseminate forecast outputs and results is becoming a very important part of the forecasting process. Such tools have to be conceived in a way that allows users to easily extract and clearly identify the necessary information from large ensembles and the associated statistics representing the forecast and its uncertainties. In this paper, we present the first system for the visual exploration and analysis of these kinds of forecasts. Our system handles multivalued ensembles of heightfields comprising multiple time steps. A set of statistical properties is derived from the ensemble and can be explored in multiple linked views, while the complete ensemble is always available for detailed inspection on demand. Our system enables domain experts to efficiently plan the placement and operation of off-shore structures, such as oil platforms.

Chapter 2

Related Work

This thesis combines the work from several publications, covering diverse areas of research. In this chapter we present the most important previous work.

The major theme is visualization and feature extraction from seismic data. Section 2.1 gives an overview over applications, workflows and techniques, specific to subsurface modeling and seismic interpretation. The following Section 2.2 focuses on visualization in this area. A more general look at segmentation techniques, not specific to seismic data, is given in Section 2.3. We introduce volume deformation and exploded views to seismic visualization. Section 2.4 presents common techniques.

The simulations used for creating the ocean forecast data, just like the parameter sampling approach to horizon extraction, map uncertainty to variation in the resulting ensemble data. The final two sections give an overview over other applications and techniques for ensemble visualization (Section 2.5) as well as uncertainty visualization in general (Section 2.6).

2.1 Subsurface Modeling and Seismic Interpretation

The importance of oil and gas for today's societies has resulted in a considerable amount of previous work in the area of seismic interpretation and visualization, as well as commercial software packages, such as HydroVR [55], Petrel [100] or Avizo Earth [106].

One important area is seismic interpretation and seismic horizon extraction. Pepper and Bejarano [78] give a good overview over seismic interpretation techniques.

Gao [28] presents a complete workflow in four phases for visualization and interpretation of seismic volumes. The phases are data collection and conditioning, exploration, analysis, and finally design of well-bore paths. The exploration phase, which includes interpretation, carried by slicing the volume along the axes, results in a conceptual model. Gao guides through the workflow using several case studies.

A lot of work has focused on fully automatic approaches for horizon extraction. These techniques usually require the definition of some parameters, but afterwards work without user interaction. Keskes et al. [49] and Lavest and Chipot [52] show an abstract outline of such algorithms for fully automated 3D seismic horizon extraction and surface mesh generation. Tu et al. [103] present an automatic approach for extracting 3D horizons, based on grouping 2D traces. Faraklioti and Petrou [27] and later Blinov and Petrou [7] present real 3D surface reconstruction using connected component analysis parameterized by the local waveform and layer direction. However, processing the complete volume at once is a lengthy process, thus parameter tuning is inconvenient. Additionally, optimal parameters are not necessarily equal for all features in the volume.

Castanie et al. [15] propose a semi-automatic approach. Horizons are traced one by one from a user-defined seed point. Interactivity in these kind of methods is limited as the horizon extraction is costly, resulting in long waiting times between seeding.

Patel et al. [74] present a technique for quick illustrative rendering of seismic slices for interpretation. They use transfer functions based on precomputed horizon properties. Their method, however, only works on 2D slices. In a subsequent publication [76] they extended their illustration technique for rendering of 3D volumes to be used in a framework for knowledge-assisted visualization of seismic data. This method still relies on slice-based precomputation.

Borgos et al. [8], as well as Patel et al. [73], propose interactive workflows for the surface generation based on an automatic preprocessing step. Both extract surface patches from the volume in a preprocessing step by extrema classification and growing, respectively. This step lasts for several hours. In a second, interactive step the user then builds the horizon surface using the pre-computed patches. Where in the work of Borgos et al. the surface patches function as simple building blocks, Patel et al.'s approach is more sophisticated. The extracted patches are subdivided and stored hierarchically. The user starts the surface generation with a single seed patch and by climbing up the hierarchy adds connected patches. The authors themselves target their approach to quick extraction of horizon sketches which then need to be refined in a second step.

Kadlec et al. present a method for real-time calculation of channels [44] and faults [45] using level sets on the GPU, an approach which grows the seismic structures from a seed point according to local properties of the volume. In a subsequent publication [46] they present a user study to validate their techniques. Jeong et al. [42] implemented a method based on coherence-enhancing anisotropic diffusion filtering using the GPU to identify faults in real-time.

2.2 Volume Visualization for Seismic Data

Engel et al. [21] give a comprehensive overview of the basics of volume graphics, including slicing and ray casting-based approaches.

Kidd [50] presents basic ideas for seismic volume visualization. He argues that volume rendering can be used to gain an overview of a seismic cube without time consuming interpretation. Kidd proposes a fairly simple zone system that partitions the data range in six parts, to which then predefined colors are assigned automatically.

Castanie et al. [14, 15] were the first to use pre-integrated ray casting for seismic visualization. They give an overview of the special demands for visualization of seismic data and demonstrate the advantages of ray casting compared to slicing approaches for direct volume rendering of seismic data.

Meaningful visualization of 3D seismic data is a hard problem, since seismic volume data are very dense and noisy. Gradients cannot be used well in large parts of the volume, and generally have different semantics than for example in typical medical datasets. Where a strong gradient in a computed tomography (CT) scan usually corresponds to a material boundary, in seismic reflection data the subsurface boundaries are represented as local extrema, where the gradients are usually very small. This means that volume illumination with gradient-based approaches like the Blinn-Phong model [6] in combination with classical volume rendering approaches does not work well for these data.

Silva [102] shows that the gradient of the so called instantaneous phase attribute yields a better normal candidate, which is normal to the peak amplitudes. He then compares the renderings of volumes shaded with standard gradients with volumes shaded with the new gradients which give better results.

Patel et al. [73] present a volume rendering technique that employs gradient-free shading. They argue that local ambient occlusion as presented by Ropinski et al. [93], a common gradient-free shading approach, is not a good fit for seismic data. The reasons are not only time- and memory-intensive pre-computation, but also the high frequency and noisy nature of seismic data. Instead, they propose a technique called forward scattering. However, since their particular approach is based on slicing, their technique cannot easily be adapted to ray casting. Šoltészová et al. [107] investigate how shadows and shading relate to curvature and depth perception. In addition they introduce a shading technique that represents shadows with modified luminance rather than by darkening, to avoid conveying information by over darkening.

Besides shading, visibility is a big problem for visualizing dense data such as seismic volumes. There exist a lot of techniques to conquer this problem, most of them borrowed from illustration.

Ropinski et al. [94] introduce focus+context methods to seismic visualization. They employ different transfer function to different regions of the seismic cube. Furthermore their system is integrated into a virtual workbench, providing stereoscopic visualization for a more immersive experience.

A typical example for illustrative techniques are exploded views. Exploded views allow looking inside the data by cutting parts away, but instead of removing these parts, context is maintained by displacing the cut away objects. Bruckner et al. [13] present exploded views for volume data. In their approach, the dataset is first split into multiple convex parts which are then transformed using a force-directed layout. They render these parts one by one. Therefore, the parts have to be sorted according to their visibility and, after rendering, blended into a single buffer. Design Principles for cutaway illustrations for visualization of 3D geological models are presented by Lidal et al. [54]. Birkeland et al. [5] have created a cut plane that adapts to the volumetric data by acting like a deformable membrane. This works particularly well when cutting through seismic data along the depth axis. The membrane will then adapt itself and snap to strong reflectors as the membrane is pushed downwards.

2.3 Image and Volume Segmentation

We propose an interactive seismic interpretation workflow exploiting global energy minimization inspired by segmentation techniques employed in computer vision. Our method does not require any pre-computation and allows modification of computed surface patches by adding constraints. By applying the surface extraction on smaller chunks (i.e, prisms) instead of the complete volume at once, we maintain an interactive workflow for extracting piecewise global optimal horizon surfaces.

Typical image segmentation systems based on energy minimization can be divided into two classes, based on the types of constraints they provide. Approaches based on graph cuts [9, 10, 11] work by dividing the image in fore- and background elements. The boundary is then defined implicitly between neighboring fore- and background image elements. Consequentially, constraints can be set by defining specific elements as fore- or background. The second type of energy minimization algorithms for segmentation are algorithms like Live Wire/Intelligent Scissors [66, 68], which trace a line through a set of given points (the constraints) which is supposed to bound the feature which is to be extracted. Here constraints are explicit, giving the user full control over the boundary.

Depending on the application, both types of constraints have their advantages. For seismic interpretation it is crucial to be able to directly interact with the boundary (representing the seismic horizon), making explicit constraints a much better choice than implicit ones.

While graph cuts adapt naturally to 3D [3, 10], or higher dimensions in general (the cut in an n-dimensional graph is always of dimension n-1), the application of Live Wire/Intelligent Scissors will always produce a line. These lines can be used as a boundary for 2D objects, but not 3D objects, which are bounded by a surface. Poon et al. [84] exploit this property to track vessels in 3D. There are a number of publications dealing with the extension of Live Wire to 3D to create minimal cost surfaces. Falcão and Udupa [24, 26] propose automatic tracing in 2D using a user-defined trace on orthogonal slices as constraints. Their approach, however, requires considerable user supervision, especially when trying to segment objects with a topology different from a sphere. Schenk et al. [99] introduce a combination of Live-Wire and shape-based interpolation. Poon et al. [85, 86] present a technique similar to Falcão et al. [24, 26] which can handle features with arbitrary topology, by defining inner and outer contours. However, all these methods are based on creating some kind of network of lines computed using the classical 2D Live Wire algorithm, which has several drawbacks; A set of minimal cost paths in a 3D image does not necessarily assemble a minimum cost surface. Consider two circles. A minimal surface connecting the circles will be a catenoid. The shortest path connecting any two points from the two circles will however be a straight line and will thus not lie on the surface of the catenoid (compare Figure 2.1). Another major problem is that the placement of the *key paths* is crucial for the quality of the resulting surface, especially if the topology changes between slices as might be the case for concave objects. Additionally, from a user perspective it can be much

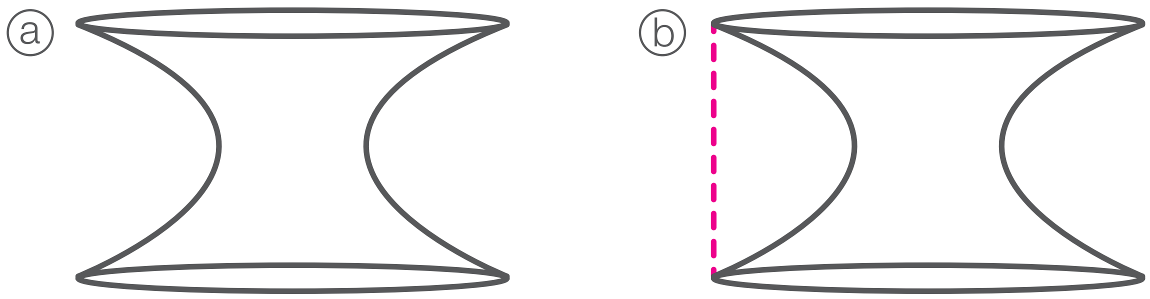

Figure 2.1: Illustration of the differences between shortest paths and minimal surfaces. ⓐ shows the catenoid forming a minimal surface between two circles. The shortest path (magenta in ⓑ) connecting two points on the two circles does not lie on the surface of the catenoid. (Figure reproduced from Grady [30])

harder to edit a network of minimal cost paths. For example, a constraint set in one slice will not necessarily propagate to the next slices, etc.

The only method we know of, to find minimum cost surfaces in 3D with explicit constraints like in the Live Wire approach was proposed recently by Grady [29]. This work formulates the minimal cost surface problem as an extension of the original 2D minimal cost path problem and shows that it can be solved with linear programming. In later work, Grady [30] presents an optimized solution for regular 6-connected lattices using minimum-cost circulation network flows. This approach results in the real minimal cost surface and is also independent of topology. The algorithm requires a single arbitrarily shaped closed contour as input and allows discretionary closed contours as constraints.

2.4 Volume Deformation

Westermann and Rezk-Salama [110] propose a method for free-form volume deformation on graphics hardware. A key element of their approach is to not deform the volume itself, but rather the mapping into the volume. Rezk-Salama et al. [90] describe an approach for volume deformation that works by adaptively subdividing the volume into blocks which can be linearly deformed. They reached interactive rendering speeds for small datasets on then-available programmable graphics hardware. Their approach, however, does not work when using advanced memory layouts like bricking. Schulze et al. [101] have presented an approach for non-physically-based direct volume deformation. They resample the volume during deformation and render the deformed volume with standard volume rendering. Their technique allows deformation of moderately-sized volumes, at voxel resolution, at interactive frame rates, but the affected area must be limited. Lampe et al. [51] present a technique to deform and render volumes along curves. They illustrate two applications, one of which is the visualization of seismic data along well logs.

2.5 Ensemble Visualization

Early work on visualization of ensemble data was conducted by Pang, Kao and colleagues [47, 48, 56, 58]. While the authors did not use the term ensemble, these works deal with the visualization of what they call spatial distribution data, which they define as a collection of n values for a single variable in m dimensions. These are essentially ensemble data. The authors adapt standard visualization techniques to visualize these data gathered from various sensors, e.g. satellite imaging or mutli-return Lidar. Frameworks for visualization of ensemble data gained from weather simulations include *Ensemble-Vis* by Potter et al. [89] and *Noodles* by Sanyal et al. [97]. These papers describe fully featured applications focused on the specific needs for analyzing weather simulation data. They implement multiple linked views to visualize a complete set of multidimensional, multivariate and multivalued ensemble members. While these frameworks provide tools for visualizing complete simulation ensembles including multiple dimensions, to solve the problem presented in this work we focus on 2.5D surfaces, i.e. heightfield ensemble data.

Matković et al. [61] present a framework for visual analysis of families of surfaces by projecting the surface data into lower dimensional spaces. Piringer et al. [83] describe a system for comparative analysis of 2D function ensembles used in the development process of powertrain systems. Their design focuses on comparison of 2D functions at multiple levels of detail. Healey and Snoeyink [33] present a similar approach for visualizing error in terrain representation. Here, the error, which can be introduced by sensors, data processing or data representation, is modeled as the difference between the active model and a given ground truth.

2.6 Uncertainty Visualization

A good introduction to uncertainty visualization is provided by Pang et al. [72], who present a detailed classification of uncertainty, as well as numerous visualization techniques including several concepts applicable to (iso-)surface data, like fat surfaces. Johnson and Sanderson [43] give a good overview of uncertainty visualization techniques for 2D and 3D scientific visualization, including uncertainty in surfaces. For a definition of the basic concepts of uncertainty and another overview of visualization techniques for uncertain data, we refer to Griethe and Schumann [31]. Riveiro [92] provides an evaluation of different uncertainty visualization techniques for information fusion. Rhodes et al. [91] present the use of color and texture to visualize uncertainty of iso-surfaces. Brown [12] employs animation for the same task. Grigoryan and Rheingans [32] present a combination of surface and point based rendering to visualize uncertainty in tumor growth.

There, uncertainty information is provided by rendering point clouds in areas of large uncertainty, as opposed to crisp surfaces in certain areas.

Recently, Pöthkow et al. [87, 88] as well as Pfaffelmoser et al. [80] presented techniques to extract and visualize uncertainty in probabilistic iso-surfaces. In these approaches for visualizing uncertainty in iso-surfaces, a mean surface is rendered as the main representative surface, while the positional uncertainty is represented by a 'cloud' based on the variance around this surface. Pfaffelmoser and Westermann [81] describe a technique for the visualization of correlation structures in uncertain 2D scalar fields. They use spatial clustering based on the degree of dependency of a random variable and its neighborhood. They color-code the clusters, but also allow the visualization of primary information like the standard deviation, for example by extruding clusters into the third dimension.

Lundström et al. [57] propose the use of animation to show the effects of probabilistic transfer functions for volume rendering. A system which models and visualizes uncertainty in segmentation data based on a priori shape and appearance knowledge has been presented by Saad et al. [96].

Chapter 3

Visual Subsurface Modeling

This chapter is based on the papers *Interactive Seismic Interpretation with Piecewise Global Energy Minimization* [35] and *SeiVis: An Interactive Visual Subsurface Modeling Application* [37] as well as the poster *Seismic Horizon Tracing with Diffusion Tensors* [38].

Creating a subsurface model from a seismic survey consists of several steps. The major tasks are extracting the relevant features from the seismic cube, followed by the creation of a velocity model, based on the extracted features and corresponding to the speed of the seismic waves in the subsurface. Finally using the velocity model the extracted features can be converted from time into spatial depth. In this chapter we describe how these steps are carried out in current practice (Section 3.1). Even though we use the same three modules, using our joint time/depth visualization (Section 3.2) results in a completely different workflow. The joint time/depth visualization in combination with our prism based workflow (Section 3.3) allows direct use of depth domain based well data during the time domain based horizon extraction. In Section 3.4 we discuss the weaknesses of common horizon extraction techniques based on local solvers and present our approach to a horizon extraction using global optimization. The results and evaluation of this work can be found in Section 3.5.

3.1 Current Practice

The following description of the current practice is based on the industry standard software Schlumberger Petrel [100]. While implementation details might vary for different software tools, to our knowledge the workflow description reflects the common practice in the industry.

Horizon Extraction

The horizon extraction is usually carried out as a combination of 2D segmentations on the axis-aligned slices of the seismic reflection data. The user manually, or using semi-automatic growing techniques, tags the important horizons as lines on the slice. The auto tracer of Petrel, which is used for the semi-automatic growing, uses a local approach, which cannot be forced through constraint points and stops at ambiguous areas. Depending on the variation in the data, up to ten slices are skipped between 2D segmentations, and filled by interpolation or automatic growing. The horizon extraction process is very lengthy and accounts for the major part of the time in the typical workflow. Tagging several horizons on tens to hundreds of slices takes at least several hours but can easily keep an interpreter busy for multiple days, if the structures are not clearly visible or ambiguous. The output of the horizon extraction module is a set of surfaces describing the boundaries of the subsurface layers.

Velocity Modeling

After the horizon extraction is finished, the resulting horizon surfaces are used as a basis for creating a velocity model. The velocity model is defined in a table view, where for every subsurface layer the corresponding top and bottom boundaries (horizons or other surfaces), as well as velocities are set. Once all desired layers are defined, a volume containing per-voxel velocities (the so-called *velocity cube*) can be computed off-line.

Depth Conversion

Finally, based on the velocity cube, the depth conversion can be computed. Using the per-voxel velocities, the original volume and the extracted horizons can be resampled, again off-line, from top to bottom into a new, depth-converted dataset.

Integration

Creating the velocity cube, as well as the final depth conversion, requires the user to manually create a new derived dataset, as well as lengthy computations. In addition, the derived datasets are not coupled. An update in one of the modules does not automatically trigger the re-evaluation of subsequent modules. Instead, a new derived data set has to be set up manually. This results in the linear workflow illustrated in Figure 3.1ⓐ, where each module requires the result of the previous module as input. Due to the lengthy computations in between, usually no interme-

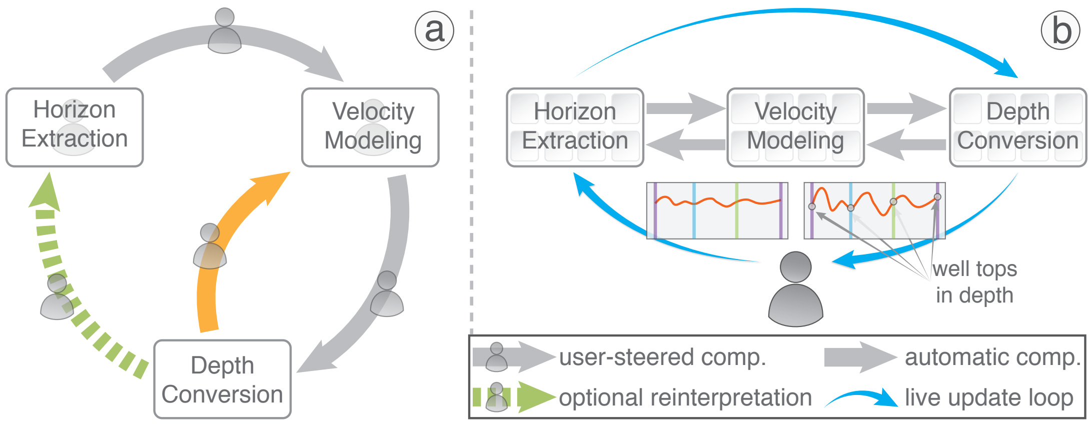

Figure 3.1: The conventional workflow ⓐ with multiple user-steered computations, compared to our novel joint time/depth modeling workflow ⓑ with a fully integrated, automatic live update loop.

diate results are pushed to the next module in the pipeline. A major drawback of this approach is that mistakes that occur during the horizon extraction often only become visible after finishing the complete pipeline, when matching the depth converted data to the ground truth data, which is available only in depth. In an ideal workflow, the interpreter would go back to the interpretation and fix mistakes (indicated by the green arrow in Figure 3.1ⓐ). More commonly, however, a shortcut is taken to save time, by locally "hot fixing" the velocity cube to match the features, accepting a possibly unphysical velocity model.

3.1.1 Weaknesses and Proposed Enhancements

The traditional workflow has two major shortcomings.

1. The precise ground truth data gathered from drillings and only available in the depth domain is not available while interpreting the seismic cube in the time domain, but only after a complete interpretation cycle.

2. Since re-interpreting the seismic data after a complete interpretation cycle is very tedious and time consuming often a shortcut is taken after a few cycles, by 'hot fixing' the velocity model locally to match the ground truth data (indicated by the orange arrow Figure 3.1ⓐ).

Proposed Enhancements

In this work, we propose a novel integrated workflow as shown in Figure 3.1 ⓑ. This workflow consists of the same three modules as the traditional workflow; horizon extraction, velocity modeling and depth conversion, however, we propose several modifications, which drastically alter the overall workflow, to eliminate the weaknesses, described above.

Our most important goal is to integrate the spatial ground truth data, gathered from wells, into the time domain-based horizon extraction. This allows the creation of a correct model in a single pass, eliminating the need to go through multiple iterations. Therefore we propose two modifications to the traditional workflow:

1. Provide the user with a joint time/depth domain workflow, which integrates the ground truth data gathered from wells into the interpretation workflow. Therefore we propose side by side views of the time and depth domains, where the depth domain view provides on the fly updates based on the intermediary results from the horizon extraction and velocity modeling.

2. To make as much use as possible of the well data, we subdivide the seismic cube into prisms based on well positions for the horizon extraction, rather than axis aligned slices. Each of the prisms will allow access to data from three wells, while the availability of well data on axis aligned slices is mostly random.

In addition, to ease the surface extraction itself, we propose the use of an interactive, user-steered global optimization technique instead of local solvers.

3.2 Joint Time/Depth Domain Visualization

To allow matching features extracted in the time domain to the ground truth well data in the depth domain, we propose the use of side by side views of the data in both domains as illustrated in Figure 3.2. The goal of these side by side views is to allow the user to modify the interpretation in one view and immediately provide the results of the modifications on the depth converted model in the other view.

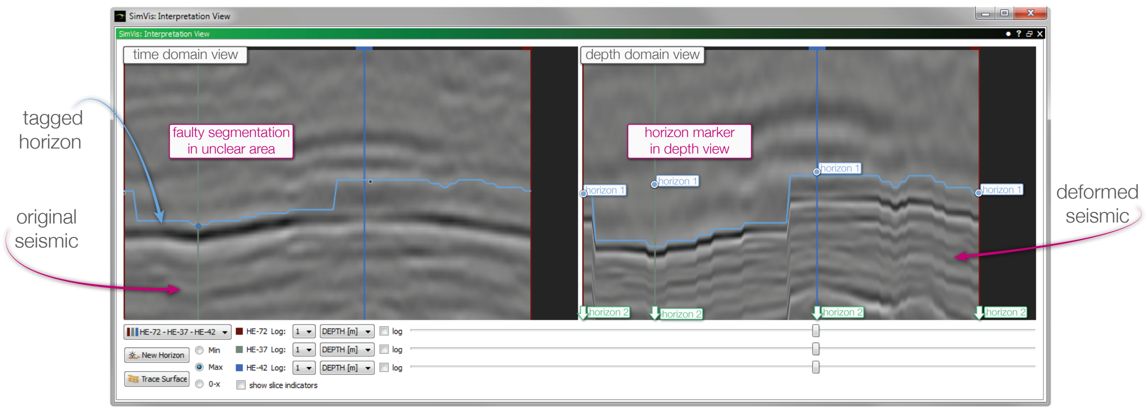

Figure 3.2: An example for our joint time/depth domain views. The left view shows the original data in the time domain. A horizon was tagged wrongly in an unclear area. The right view shows the depth converted data. Well tops are available in this view to guide the segmentation. The user can now fix the horizon in the time domain view and get live updates on the fit to the well top in the depth domain view.

Interactive updates in both views are essential for this joint time/depth domain workflow to work properly.

Converting the complete data from one domain into the other at interactive rates is not a trivial task. State of the art commercial software, like Schlumberger Petrel [100] convert the data from one domain into the other by resampling the complete dataset in an off-line process. Converting the whole seismic cube can take from several seconds to minutes, even for small datasets. Such a process makes interactive updates impossible.

To enable interactive updates in our joint time/depth domain views, we implemented a visualization pipeline specifically optimized to handle frequent updates of the extracted horizon surfaces, as well as a volume deformation approach where

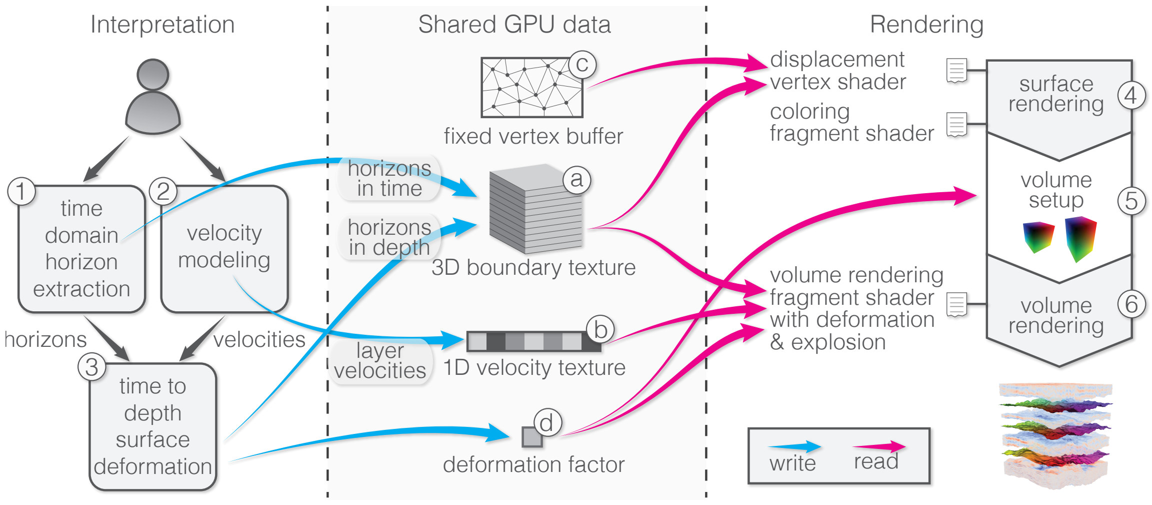

Figure 3.3: Rendering pipeline for joint time/depth interaction. Horizon extraction ①, velocity modeling ② and deformation ③ modules constantly update the texture data ⓐ,ⓑ. The data is shared over all views and the different steps ④, ⑤ and ⑥ in the rendering pipeline.

only the extracted features are deformed and saved, while the actual volume data is converted from the time domain to spatial depth on the fly during rendering.

3.2.1 Rendering Pipeline

Figure 3.3 shows our integrated pipeline for rendering seismic volume data and horizon surfaces with the application of deformation and exploded views. In the remainder of this section, circled numbers and letters refer to this figure. While the figure illustrates the pipeline for the volumetric case, we use the same pipeline for 2D views to provide depth conversion during interpretation. The main difference is that the heightfield geometry ⓒ, as well as the boundaries texture ⓐ, are of one dimension lower (compare Table 3.1). The pipeline is divided into two major blocks: the interpretation block on the left, and the rendering block on the right.

	Texture / Buffer	Dim. 3D/2D	Type	Function	Size 3D	Size 2D
ⓐ	bounds	3D/2D	luminance α texture	layer boundaries in original (.r) and deformed (.a) space	$x{\cdot}y{\cdot}\#\mathrm{B}{\cdot}2$	$x \cdot \#\mathrm{B} \cdot 2$
ⓑ	velocities	1D	luminance texture	layer velocities	#L	#L
ⓒ	heightfield geometry	2D/1D	vertex buffer	generic vertex buffer for horizons	$x \cdot y \cdot 3$	$x \cdot 2$

Table 3.1: Textures and buffers needed in our pipeline in addition to basic volume rendering. ⓐ, ⓑ, and ⓒ correspond to Figure 3.3. #B and #L represent the number of boundaries and the number of layers, respectively. Sizes are given in number of 32-bit floating point entries.

Interpretation

Interpretation comprises three modules. The horizon extraction module ①, and the velocity modeling module ②, which comprise the actual surface extraction and the definition of the velocity values for the corresponding layers. The output of the horizon extraction is a 2D heightfield that covers the complete volume domain, plus a 1D heightfield for the boundary of the current prism. Both are constantly updated during the interpretation process. Each heightfield corresponds to a single horizon, and is stored as a layer in the first channel of the 3D or 2D boundaries texture ⓐ on the rendering side, and is also available to the depth conversion module on the interpretation side.

The velocity modeling module ② outputs a velocity value for each layer, which is stored into the 1D velocities texture ⓑ.

The surface deformation module ③ takes the updated heightfields from the horizon extraction module ①, and converts the values from the time to the depth domain using the velocity model from the velocity modeling module ②. Compared to recomputing the deformation for the complete volume, very little data needs to be processed, allowing real time updates (compare Table 3.2 in the performance discussion in Section 3.2.3).

The resulting depth-converted heightfields are stored in the second channel of the 2D or 3D boundaries texture ⓐ. In addition, the depth conversion module outputs the maximum scaling factor ⓓ needed to cover the depth conversion at any (x, y)-position.

Rendering

The data is shared between all views and steps in the visualization pipeline. Table 3.1 gives an overview of the shared textures and buffers. Basically all of our views make use of vertex and fragment shaders to exploit the possibilities of the programmable OpenGL pipeline. We used this, for example, to streamline the horizon surface rendering part ④ of the pipeline. Instead of creating geometry for each horizon, we use a single generic vertex buffer ⓒ, covering the complete (x, y)-domain, but without the depth (z) information at the vertices. We render the surfaces one by one and use the boundaries texture ⓐ in the vertex stage to assign the appropriate z-values to each vertex.

Invalid fragments, i.e., the fragments belonging to triangles in the mesh that are not yet covered by the interpretation, are discarded. Additionally, we use the fragment shader to compute several properties of the surfaces on the fly. Using the data which is already available for the other rendering stages on the GPU, several properties can be plotted directly onto the surface without precomputing a separate texture. The amplitude can be looked up directly from the volume texture. Cost or deviation from the target amplitude can be computed on the fly based on data from the same texture. The distance to other surfaces can be evaluated using the boundaries texture.

3.2.2 On the Fly Deformation

The volume deformation required for the depth conversion is highly constrained. Deformation only needs to be applied to the depth axis of the volume, in order to convert its unit from time to spatial depth in the subsurface. We represent horizons as heightfields, and we can safely assume that no horizons intersect. Thus, every two adjacent horizons enclose one subsurface layer. Furthermore, the velocity for each layer in the volume can be assumed to be constant, using an average value. Thus, the deformation can be simplified to a piecewise linear stretching or compression of the volume between each two adjacent horizons. Taking these constraints into account, it is possible to implement the deformation in a simple and efficient manner. This enables depth conversion at real-time frame rates during volume and slice rendering, without precomputing a deformed volume.

Concept

Our approach is inspired by the work of Westermann and Rezk-Salama [110]. Conceptually, we never deform the original volume, but render a virtually deformed volume, converting the look-ups in this volume into the original volume space on the fly in the fragment shader. We do that by converting only the layer boundaries (which are the result of the interpretation in progress) from time to depth. The n-th deformed boundary b'_n can be computed as

$$b'_n(x,y) = \sum_{k=1}^{n} (b_k(x,y) - b_{k-1}(x,y)) \cdot v_k \tag{3.1}$$

from the time domain boundaries b_n and velocities v_n. Figure 3.4 illustrates the deformation with this simple iterative computation of the deformed boundaries. The boundaries have to be recomputed only when a velocity value is changed or a horizon is modified. Computational complexity is $O(n)$, with n the number of vertices that need to be updated. Since the computation is independent for each (x, y)-position, we have parallelized it using OpenMP. We measured computation times for several surfaces and even for larger surfaces consisting of roughly a million quads, the update time for a couple of horizons is interactive (see Table 3.3 in the performance discussion in Section 3.2.3).

For volume rendering, we use a single-pass ray caster. The ray caster is set up to cast into a virtual volume, resized with the scaling factor ⓓ, which is set to the maximum value of the bottom boundary to fit the deformed volume. During ray casting, the depth-converted boundaries are used to compute the actual look-up in

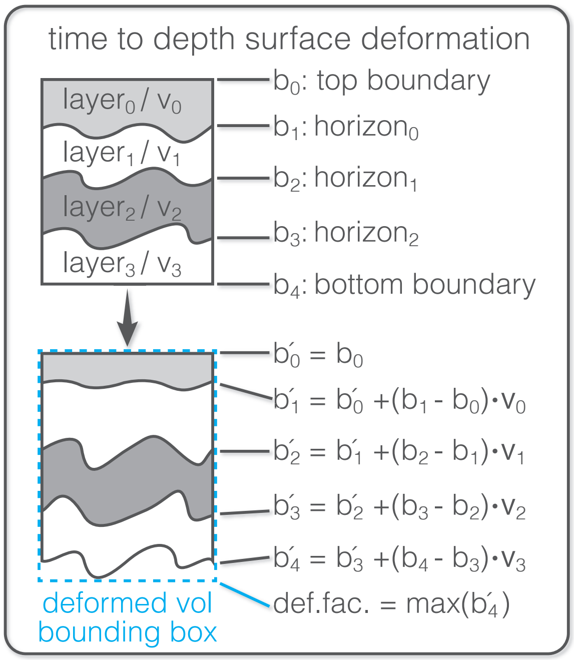
time to depth surface deformation
$layer_0$ / v_0
$layer_1$ / v_1
$layer_2$ / v_2
$layer_3$ / v_3
b_0: top boundary
b_1: $horizon_0$
b_2: $horizon_1$
b_3: $horizon_2$
b_4: bottom boundary
$b'_0 = b_0$
$b'_1 = b'_0 + (b_1 - b_0) \cdot v_0$
$b'_2 = b'_1 + (b_2 - b_1) \cdot v_1$
$b'_3 = b'_2 + (b_3 - b_2) \cdot v_2$
$b'_4 = b'_3 + (b_4 - b_3) \cdot v_3$
deformed vol bounding box
def.fac. = max(b'_4)

Figure 3.4: Illustration of the surface deformation (Fig. 3.3 ③) with computation of deformed boundaries.

the original volume. Rendering the unfolded prism sides can be done in a similar manner. For each side, we set up a quad that fits the size of the deformed side, and the same indirect texture look-up as described for volume rendering is used for the slice rendering.

Rendering Setup

In the setup step of the ray caster ⑤, the extents of the bounding geometry have to be adapted to fit the deformed volume. This is done by scaling the z-axis of the bounding geometry with the deformation factor ⓓ.

Fragment Shader

In the ray casting stage ⑥ the coordinates for the volume texture look-up have to be modified in the fragment shader. The pseudo code in Figure 3.5 illustrates the conversion of the virtual (deformed) coordinates to the actual sampling position in undeformed volume coordinates in the fragment shader. The sample position in the deformed space is used to look up the id of the current layer. Using the layer id, the layer's upper boundary is fetched for each (x, y)-position in original and deformed space. Using the layer's velocity, the z-position in the layer is then transformed back into undeformed volume space, resulting in the sample position in volume space.

The same principle is used for the main interpretation view containing the unfolded prism sides. To apply the depth conversion to the slice views, we simply scale the side of the quads corresponding to the volume's z-axis, and use the same fragment shader code shown in Figure 3.5 to compute the position for the texture look-ups.

3.2.3 Performance

We have measured the rendering performance for the live deformation with two different datasets: The first dataset, shown in Figure 3.6a is moderately sized with $240 \times 240 \times 1509$ voxels, and at 330MB fits completely into GPU memory. The second dataset (Figure 3.6b) comprises $1422 \times 667 \times 1024$ voxels, resulting in roughly 4GB, meaning the dataset does not fit the GPU memory of our test system described below. Therefore, for rendering the second dataset, we use a multi-resolution approach as presented by Beyer et al. [4]. This approach allows rendering different parts of the data at different resolution levels with smooth transitions using a

```
uniform sampler1D velocities;
uniform sampler3D boundaries;
uniform float scaleFactor;

convertSamplePosToVolumeSpace( x, y, z )
{
   // scale from [0..1] to deformed volume coordinates
   z *= scaleFactor;

   // get the id of the current layer
   float layerId = getLayerId( x, y, z );

   // lookup layer offset in undeformed and deformed volume coordinates
   vec2 layerOffset = texture3D( boundaries, vec3( x, y, layerId ) ).xw;

   // distance to layer boundary in deformed volume coordinates
   float posInLayer = z - layerOffset.y;

   // distance to layer boundary in deformed volume coordinates
   float velocity = texture1D( velocities, layerId );
   posInLayer /= velocity;

   // update z coordinate to sample in volume coordinates
   z = layerOffset.x + posInLayer;

   return vec3( x, y, z );
}
```

Figure 3.5: Pseudo code for live volume deformation. Virtual (deformed) coordinates are converted to undeformed coordinates on the fly during rendering in the fragment shader. The syntax is similar to GLSL.

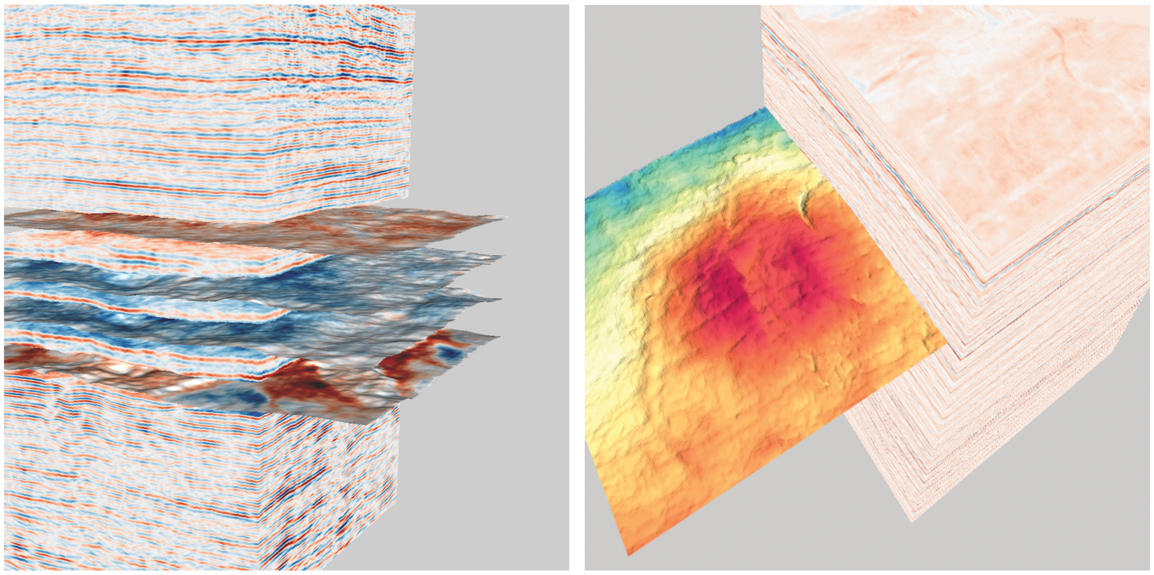
(a) Dataset 1 **(b)** Dataset 2

Figure 3.6: Volume renderings of the two datasets used for the performance measurements.

multi-resolution hierarchy. We extended the system os that it can provide different resolutions levels of the same data to different parts of the pipeline. I.e. we allow the visualization part to fall back on lower resolution levels, if GPU memory is low, but provide the surface extraction module always with the highest resolution data. The surfaces cover the complete (x, y) extents of both datasets with a resolution of one vertex per voxel resulting in $57,600$ and $948,474$ quads, respectively. Computation of the deformed surfaces was done on the CPU using a dual six-core Xeon X5680 at 3.33Ghz. Rendering was done on a NVIDIA Geforce GTX 580 with 1.5GB of memory, with the volume rendered screen-filling into a 1024×1024 viewport with two samples per voxel.

Table 3.2 shows the performance of the surface deformation algorithm. For the smaller dataset we can easily achieve interactive update rates with 9 and 12ms per update for three and five surfaces, respectively. Since the performance is mostly dependent on the size of the surface, computation for the larger dataset is signifi-

Dataset		Samples per Surface	Number of Surfaces	Computation Time
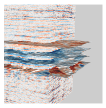	$240 \times 240 \times 1509$	$57,600$	3	9ms
			5	12ms
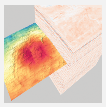	$1422 \times 667 \times 1024$	$948,474$	3	144ms
			5	174ms

Table 3.2: Surface deformation performance for the on the fly depth conversion.

cantly slower. Computation time of 144ms for three surfaces, however still allows for seven updates per second. While this does not quite allow updates in real time during the surface deformation, it should be noted that the computation only needs to be carried out when the surface geometry or the velocity model is modified and thus does not have an impact on rendering speed during regular interaction. In addition in a typical workflow, where surfaces are extracted top to bottom only the last layer needs to be updated, meaning that the case for three surfaces is basically the worst case.

Performance for the ray casting algorithm with live depth conversion, as presented in Section 3.2.2, is shown in Table 3.3. In comparison to the standard ray casting algorithm used for rendering the undeformed volume, this technique requires three additional texture look-ups and four floating point operations per sample to compute the sample position in the original volume (compare the source-code in Figure 3.5). In addition, to get the layer id of the current sample, a number of additional texture look-ups have to be performed. The actual number depends on the search algorithm used. Right now we step through all layers from top to bottom until reaching the current sample point. This results in the performance loss shown in Table 3.3, when adding more layers.

Dataset		Number of Surfaces	Base	Depth Conversion	% of Base
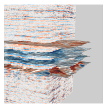	$240 \times 240 \times 1509$	3	117fps	99fps	85%
		5		87fps	66%
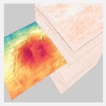	$1422 \times 667 \times 1024$	3	101fps	81fps	80%
		5		77fps	76%

Table 3.3: Performance comparison of the live depth conversion. We used standard ray casting without illumination for the comparison.

Overall, performance stays well within the limits needed for interactivity for both datasets. For the larger dataset it can be seen that rendering speeds scale very well, using the multiresolution representation. Since the surfaces are deformed at full resolution there is a bigger performance penalty, however, update rates are still interactive and updates are only needed when surfaces or the velocity model is updated. In addition our visualization pipeline, described in Section 3.2.1 basically decouples the resolution of the extracted surfaces from the geometry. Thus one could imagine a similar multi-resolution approach for the deformation as for rendering, in case surface resolution becomes too big to handle at interactive rates.

3.3 Prism-Based Workflow

With the on the fly depth conversion in place we can now show the original and depth converted data side by side to allow adjusting the time domain based interpretation to the depth domain based well data. However the well data is very sparse and thus, in a slice based workflow only available on a few slices. To maximize the availability of the additional data during the interpretation we propose a workflow that is based on well positions rather than axis-aligned slices.

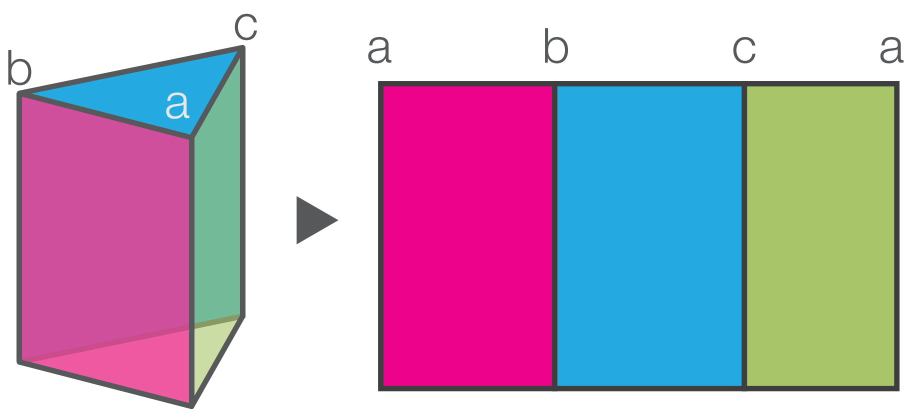

Figure 3.7: The original prism (left) unfolded into a single slice (right).

Conceptually, we always work on the sub-volume that is defined by three well positions that make up a triangle on the geological surface and form a triangular prism through the seismic volume along the z-direction. Since this approach requires a unique (x, y)-coordinate for each prism corner only well logs that are roughly orthogonal to the surface are used for creating prisms. For using well tops, these limitations do not apply. We simply treat each well top separately, even when several tops correspond to a single well and create prisms using all unique (x, y)-coordinates.

To compute the seismic horizons, we have developed an algorithm that combines the advantages of semi-automatic 2D and 3D global minimal cost path and surface algorithms. We separate the horizon extraction algorithm into a 2D minimal cost path tracing on prism faces orthogonal to the (x, y) plane, and a subsequent 3D minimal cost surface computation, which is initialized by the previously computed 2D contour. For more details on the tracing process refer to Chapter 3.4.

User interaction in this approach is mostly limited to the 2D optimization on the sides of the prism. Therefore the prism sides are unfolded into a single 2D slice as shown in Figure 3.7.

This approach was proposed by our collaborating domain experts. The main advantage of this approach is that the horizon can easily be adjusted directly at the well position, which is the point where errors in the interpretation become visible when adjusting the horizon to the ground truth data from the well log during time/depth-conversion of the seismic volume. In combination with our joint time/depth domain workflow this allows direct interaction with well data from three positions on each slice during the interpretation. After extracting a horizon surface patch for one well prism, the horizon can then be extended by processing the neighboring prisms, creating a set of horizon surface patches that constitute the horizon surface. The result from one prism will therefore be transferred to the neighbors. As a result, the interpretation itself is done triangle (prism) by triangle (prism), instead of slice by slice, making ground truth data from three wells available in every working set. To extend the horizon trace to areas not covered by wells, additional points of interest (e.g. the corners of the volume) can be added to the triangulation.

3.4 Horizon Extraction using Global Optimization

As discussed in Section 3.1 we identified several shortcomings in the current practice of horizon extraction. We presented the joint time/depth domain visualization in combination with the well based workflow above, to solve the issue of integrating the depth domain-based well data into the time domain-based horizon extraction workflow. In the following sections we will present a global optimization technique to enhance the feature extraction itself.

In Section 3.4.1 we discuss the requirements for the horizon extraction. We exemplarily present a horizon extraction technique based on a local solver in Section 3.4.2 and discuss the problems of the local solver in general as well as the weaknesses with regard to our defined requirements. In the following Sections 3.4.3 – 3.4.5 we present our proposed approach to horizon surface computation which is implemented in the presented workflow.

3.4.1 Requirements for Horizon Extraction

Horizon surface extraction using the conventional workflows of available state of the art software is a very tedious process. It is done either manually or semi-automatically using local solvers on axis-aligned slices. Fixing a mistake with these approaches is very tedious, as it requires manual correction of multiple slices. On the one hand, this is caused by the noisy and ambiguous seismic data, which causes big problems for automatic solvers, on the other hand the local solvers which are usually used, limit the possibility for semi-automatic adjustments. To enhance the process we define a set of specifications, which are desired for a semi-automatic horizon extraction workflow, based on the presented joint time/depth domain views as well as the prism-based workflow:

1. The solver should always extract a complete path/surface.
2. It must be possible to force the path/surface through desired positions.
3. The user should be able to directly interact with the surface.

The first point can be achieved with local, as well as global solvers. However, some local solvers, like ant tracking [77], which is commonly used in seismic applications, do not guarantee a complete surface. Other techniques, like level set methods [71] do not have the same problems.

Forcing the path or surface through a desired positions, as required by the second point is necessary to make sure that the tracing on the prism sides results in a closed curve, but also to allow the user to easily adjust a faulty segmentation. This is, however, not achievable with local solvers. Since only the local neighborhood is evaluated, it is not possible to guarantee that any point will be part of the final path or surface, except for the seed point. Global approaches, such as shortest path algorithms, allow this. These shortest path algorithms always find the optimal path between two points. If a third point is desired to be part of the path, the algorithm can simply search for two optimal segments, one from the start to the added point and a second from the added point to the target.

Recently, graph based image segmentation approaches, like the described shortest path algorithms, became very popular in computer vision. These approaches can be divided into explicit and implicit boundary approaches. The difference between these approaches lies in the objects which are segmented. Implicit boundary approaches, for example graph cuts [9], segment fore- and background, the result is a set of pixels/voxels that belong to the segmented object, the boundary is implicit. The result of explicit boundary approaches is a curve or surface, which encloses the segmented object. Explicit boundary approaches map naturally to the third requirement described above. While implicit boundary approaches can be constrained by fore- or background pixels/voxels, the explicit boundary approaches can be constrained by curve or surface segments, meaning that user-defined positions, which need to be part of the contour or surface map directly to constraints for the optimization.

3.4.2 Local Horizon Extraction: Tracing Diffusion Tensors

In this section we present a horizon extraction approach based on tracing a diffusion tensor based vector field derived from the seismic cube. Based on this technique we show the weaknesses, common to most local approaches.

Implementation

Edge-enhancing anisotropic diffusion [109] is a non-linear smoothing technique which preserves edges by computing an edge direction vector for every sample and using this vector as a parameter for the smoothing operation

$$\partial u_t = \mathbf{div}(D \cdot \nabla u), \tag{3.2}$$

where D is the diffusion tensor, and ∇u is the gradient of the intensity volume $u(x, y, z)$. Together, $D \cdot \nabla u$ determines the direction which the divergence operator uses to smooth the image. In the general 3D case, the diffusion tensor is computed as

$$D = [v_1 v_2 v_3] \begin{bmatrix} \lambda_1 & 0 & 0 \\ 0 & \lambda_2 & 0 \\ 0 & 0 & \lambda_3 \end{bmatrix} \begin{bmatrix} v_1^T \\ v_2^T \\ v_3^T \end{bmatrix} . \tag{3.3}$$

Based on the edge-enhancing diffusion tensor, in our system the first basis vector v_1 is computed by applying a $7 \times 7 \times 7$ Gaussian derivative kernel to the volume at each sample point. This results in the smoothed gradient ∇u_σ at position (x, y, z) (Figure 3.8ⓑ). A vector orthogonal to v_1 is then chosen as v_2, and v_3 is a vector orthogonal to both, v_1 and v_2. λ_1, λ_2, and λ_3 are scaling factors, which are responsible for rotating the gradient in the direction of the edge in order to prevent smoothing across it. We define λ_1 as the diffusivity $g(||\nabla u||)$, and $\lambda_2 = \lambda_3 = 1$. To compute the diffusivity, we use the Perona-Malik model [79]:

$$g(||\nabla u||) = e^{-\left(\frac{||\nabla u||}{k}\right)^2}, \tag{3.4}$$

where k is a parameter to adapt the filter to the noise in the image. For our horizon tracing approach, we only need the vector field computed by $D \cdot \nabla u$ (Figure 3.8ⓒ). However, even though we compute the vector field for each side of the interpretation prism using the whole neighborhood in 3D, the tracing itself is done only on the 2D slices. For this, the vectors need to be projected onto the sides of the prism (Figure 3.8ⓔ). The whole procedure of creating the vector field is done in real-time on the GPU with a shader written in the Cg language [59].

The tracing itself is then performed by numerically integrating the vector field from a user-selected seed point. For this integration, we have implemented a second-order Runge-Kutta method in the given vector field.

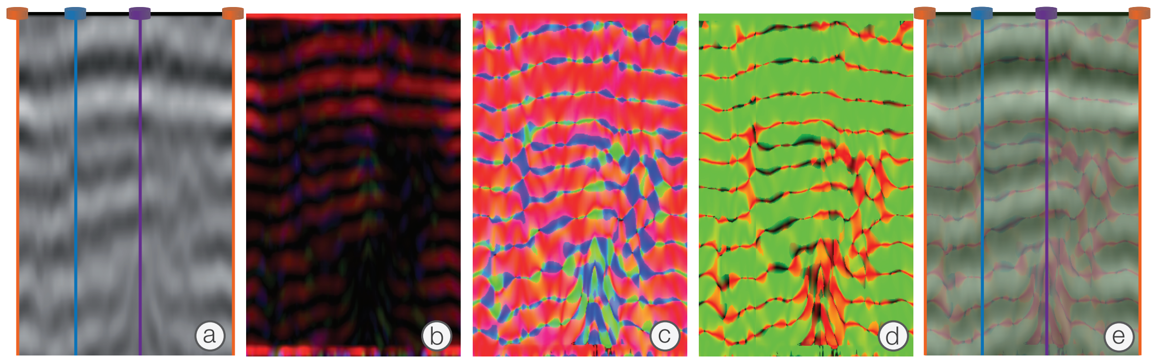

Figure 3.8: The different steps through the diffusion based tracing pipeline. ⓐ shows the unfolded sided from an exemplary prism, ⓑ the corresponding smoothed gradient map, ⓒ the gradients multiplied with the diffusion tensors, ⓓ shows the result from ⓒ projected to the 2D image plane and ⓔ the result from ⓓ blended over ⓐ. For ⓑ and ⓒ the color channels map to the volumes axes, red to the depth axis (y in the image) and green and blue to the (x, y)-plane, x in the image. For ⓓ and ⓔ red maps to the images' x-, green to the y-axis.

Jeong et al. [42] use coherence-enhancing anisotropic diffusion filtering as basis for fault detection in seismic data. In that work, the tensor is computed as shown in Equation 3.3. However, instead of directly using the smoothed gradient to create the diffusion tensor, here the Eigenvectors of the structure tensor $J(\nabla u_\sigma) = \nabla I_\sigma \otimes \nabla I_\sigma$ of the smoothed image $I_\sigma = K_\sigma * I$, with I the input image, $*$ the convolution operator and K_σ a Gaussian

$$K_\sigma(x) = \frac{1}{\sqrt{2\pi}\sigma} e^{-\frac{\|x\|^2}{\sigma^2}}, \tag{3.5}$$

are used as v_1, v_2, and v_3, in order of their contribution. The smoothed matrix J_ρ is computed by smoothing the structure tensor with another Gaussian

$$K_\rho(x) = \frac{1}{\sqrt{2\pi}\rho} e^{-\frac{\|x\|^2}{\rho^2}}, \tag{3.6}$$

resulting in

$$J_\rho(\nabla I_\sigma) = K_\rho * (\nabla I_\sigma \otimes \nabla I_\sigma). \tag{3.7}$$

Additionally $\lambda_1 \approx 0$ and $\lambda_i = e^{-\frac{(v_i \cdot \nabla I)^2}{k^2}}$, for $i = 2, 3$, where v_i is the i-th eigenvector of the structure tensor J and k is a user adjustable parameter to adjust to the contrast of the image.

For comparison, we have also implemented a variant of our approach using the coherence-enhancing diffusion tensor. Results showing the tracing, both with the coherence-enhancing, as well as the edge-enhancing diffusion tensor are shown in Figure 3.9ⓐ.

Finally, as horizons are marked by local extrema in the scalar data, we have implemented an additional version of both approaches that incorporates searching the scalar field for a local maximum or minimum in the tracing algorithm. Rather than using the result of an integration step directly as input for the next step, the neighborhood of a user-defined size in the $-z$ and $+z$ directions is scanned for the highest or lowest scalar value, respectively. The location of this value is then used instead of the integration result as support for the traced horizon, as well as input for the next integration step. Results for this method are shown in Figure 3.9ⓑ.

Results and Discussion

Figure 3.9 shows some exemplary results of the different tracing algorithms for three reflections in a seismic dataset. It can be seen that overall the traces match the reflections (or ridge-lines in this case) quite well. Comparing tracing using the edge-enhancing diffusion tensor with the coherence-enhancing tensor (Figure 3.9ⓐ) shows that the former is a little closer to the actual areas of maximum amplitude and more responsive to changes in the horizon direction. The difference between both incorporating the snapping to maximum intensity values is very small (Figure 3.9ⓑ) and for both the correctly traced parts are closest to the actual horizon of all compared methods. However, the deviation from the vector

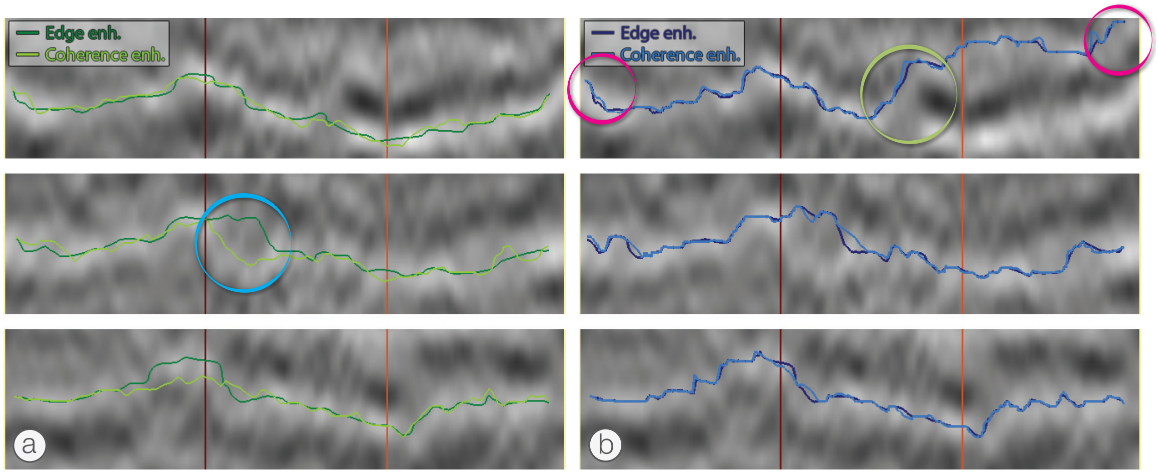

Figure 3.9: Results of the different seismic horizon tracing methods we have implemented. ⓐ edge-enhancing vs. coherence-enhancing diffusion tensor and ⓑ, just as ⓐ, but with snapping to the largest scalar value.

field there introduces a much higher chance of false classification, as can be seen on the right side of the uppermost image.

Even though promising, the results exhibit some of the typical weaknesses of local approaches. The area highlighted by the green circle in Figure 3.9ⓑ shows an area where integrating the vector field, which is based on a single sample at each step, results in a segment, where a path which is locally better, is followed (upper part of the image), resulting in the miss of the clear reflection in the lower part of the image, which would be the correct solution. With a global approach, a reflection this strong would usually not be missed. A similar behavior can be seen in the area highlighted by the blue circle in Figure 3.9ⓐ.

The magenta circles in Figure 3.9ⓑ show another problem, caused by the local nature of the approach. Since the next segment of the path is only influenced by the current sample, it is not possible to force the segmentation through any desired points. This means that we can not guarantee a closed cycle around the prism sides when using a local solver in our prism based workflow. In Figure 3.9ⓑ this can be seen at the left and right sides of the slice, which correspond to the same well position. Ideally, the segmented path should join here, however, as indicated by the magenta circles, the positions at both sides varies strongly. The fact that it is not possible to force the segmentation through desired positions also makes it very hard to edit the computed paths. When a segmentation is faulty, the only way to fix it is to remove the faulty part from the segmentation and then retrace this area, or even do the segmentation completely manually in this area.

We have shown that at least the second and third requirements set in Section 3.4.1 can not be fulfilled using this approach. The biggest problem is the fact that it can not be guaranteed that the trace results in a closed contour. In addition it is not clear how to extend the approach to three-dimensional surfaces from the extracted contours. In slice based approaches typically the gap between interpreted lines on neighboring slices is interpolated. With our well prism-based approach the area inside a prism is usually larger than the area between interpreted slices. Simply interpolating would most likely lead to very imprecise results.

3.4.3 Minimum Cost Circulation Network Flow

Instead of interpolating the horizon surfaces in between two dimensional curves, we propose performing full three dimensional optimization. The part of a horizon intersecting a given prism can be extracted by specifying as little as a single seed point, using global energy minimization techniques to compute a horizon surface of minimal cost. We combine very fast two dimensional minimal cost path tracing with subsequent three dimensional minimal cost surface computation. The path tracing computes horizon intersections along the faces of the prisms, which are then used to constrain the surface computation. By combining the optimal surfaces from the individual prisms, we receive a piecewise globally optimized horizon. Extracting the horizon in a piecewise manner allows for an interactive algorithm which gives the user full control over adjusting the surface by setting an arbitrary number of constraints, forcing the surface to pass through specified locations, while the global optimization can help fixing mistakes with very little interaction by placing a few constraints.

Algorithm

Our approach for computing horizon surfaces using global energy minimization is based on previous work of Grady [29, 30]. In his work, Grady formulates the minimization problem for *boundary constrained* 3D minimum cost surface computation and shows that minimal-cost circulation network flow (MCNF) is an optimized solution for the dual of this particular problem. By circulating the maximum possible amount of flow in the dual graph through any initial surface z_0 fulfilling the boundary constraints, eventually a set of edges will be saturated. This forms a cut, which corresponds to the minimal cost surface in the primal. The process is similar to the maximum flow, minimum cut method used for graph cuts, with the type of constraints being the main difference. Graph cuts define fore- and background elements in the image as constraints, which then form the source and sink nodes in the graph, whereas for MCNF, with no source or sink nodes present, the constraints are added as the boundary of the initial surface z_0. Hence the MCNF approach naturally matches the third requirement from Section 3.4.1.

Our algorithm for computing minimal horizon surfaces consists of the following main steps:

1. A closed contour bounding the desired surface within a prism has to be computed. This is done in a flattened representation of the prism's sides (see Figure 3.7).

2. Next, the volume contained in the prism has to be represented as a weighted, directed graph.

3. The initial surface z_0 fitting the boundary acquired in the first step needs to be inscribed in the graph.

4. The MCNF through z_0 is computed.

5. The minimal-cost surface is constructed from the set of saturated edges of the circulation, bounded by the initial contour.

6. If the surface is not satisfactory, it can be forced through desired points by placing additional constraints. These constraints are then added as additional (inner) boundary patches in step 3. Steps 4 and 5 need to be reapplied.

Below, the steps of our algorithm are explained in more detail.

2D Contour Creation

The initial closed contour for each prism is computed as a minimal-cost path on the prism sides. For any prism, the three sides are re-sampled from the volume using texture mapping with tri-linear interpolation, and stitched together into a single image. This image, superimposed with selected well log data from the prism corners, is shown in the main interpretation view and also used to construct the graph used for the minimum cost path computation. Figure 3.10 shows the mapping of an image to primal and dual graph elements. In contrast to standard approaches in image segmentation [25, 67], where the minimal-cost path/surface computation is done on the dual graph, resulting in a boundary in between image elements, the seismic horizons we want to extract are represented in the data by bands of extremal values. Thus, for seismic interpretation we do not compute the minimal-cost path in between the voxel grid but directly on the grid. The underlying graph

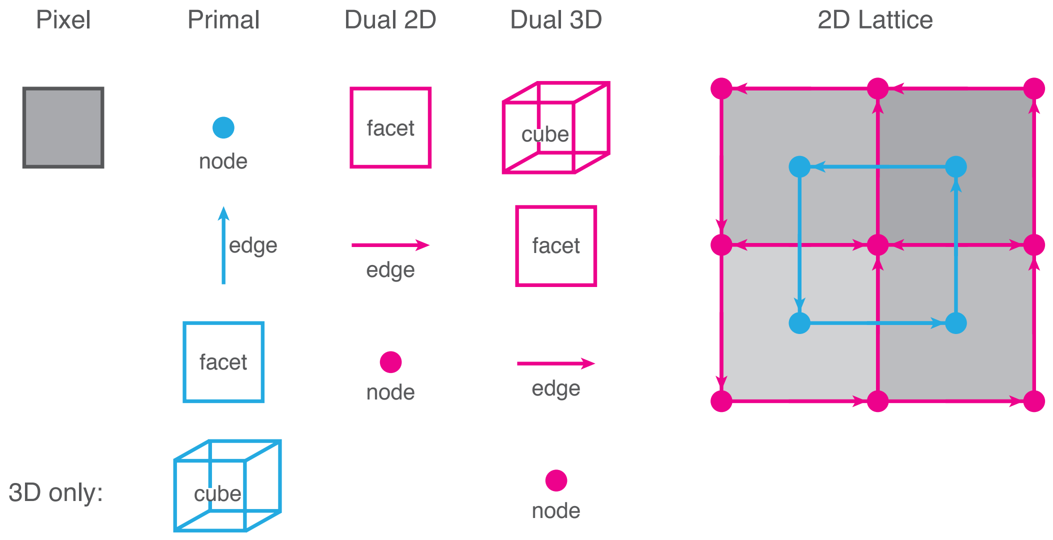

Figure 3.10: Correspondence between image/volume elements and items in the primal and dual graph. In the primal an n-dimensional pixel always maps to a node, whereas in the dual the mapping changes depending on the dimension.

then has to be the primal graph, instead of the dual graph. The resulting minimal cost path will be a set of edges connecting pixels in the image instead of dividing pixels.

Despite working on the primal instead of the dual graph, our approach is very similar to the well known live-wire workflow [66, 68]. We have implemented the minimal cost path computation in CUDA [69] on the GPU using a parallel variant of Dijkstra's algorithm [19] called delta stepping [63, 64]. The algorithm is applied on the primal graph constructed, as a 4-connected lattice according to Figure 3.10, from the stitched image of the prism sides. Edge weights are defined using the cost function defined in Section 3.4.5. The minimal path has to be bounded by at least two nodes, otherwise it will not contain any edges. To be able to compute the minimal cost path using just a single seed point, the cyclic nature of the prism sides has to be taken into account when creating the graph. Therefore all nodes in the rightmost column are connected to their counterparts in the leftmost column of the lattice. The path is forced around the prism by removing all arcs pointing to nodes in the same columns as the seed point. That way, the single seed point simultaneously functions as start- and endpoint of the path and it is ensured that the path completely encircles the prism.

Dijkstra's algorithm cannot handle constraints directly. However, constraints can be added simply by dividing the problem. Instead of trying to compute the complete path at once, the path can be coerced through any node (the constraint) in the graph by computing the minimal cost path in segments. Every constraint will then bound two connected segments, one as a start- and one as a target-node.

3D Graph Initialization and MCNF

MCNF describes the problem of putting as much flow as possible through the edges of a network at minimal cost, without adding or draining flow with dedicated source or sink nodes. Therefore, a capacity and a cost is assigned to every edge. As the graph does not contain a source or a sink, the incoming and outgoing flow at every node must be equal, thus flow can only circulate in the graph. The cost is always prioritized over the capacity of edges. If a cycle adds cost to the total flow network, it will not be used, regardless of its capacity. The capacity of a cycle is defined by the lowest capacity of the edges it consists of and the total flow in the graph is defined by the accumulated flow of all cycles.

To compute the maximum flow in a prism, the dual graph is created by using all voxels contained in the prism, according to the volume-graph scheme shown in Figure 3.10. The graph is constructed in two steps: first, the basic graph structure of the dual is created (Figure 3.11ⓐ), and costs and capacities are assigned to

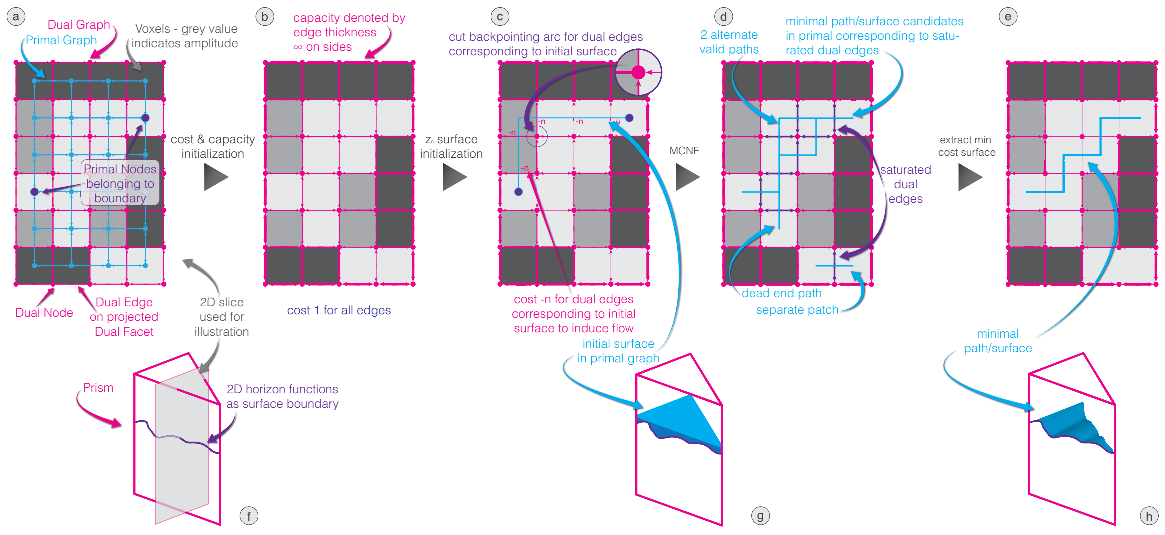
a
Dual Graph
Primal Graph
Voxels - grey value indicates amplitude
Primal Nodes belonging to boundary
Dual Node
Dual Edge on projected Dual Facet
2D slice used for illustration
cost & capacity initialization
b
capacity denoted by edge thickness ∞ on sides
cost 1 for all edges
z₀ surface initialization
c
cut backpointing arc for dual edges corresponding to initial surface
-n
cost -n for dual edges corresponding to initial surface to induce flow
initial surface in primal graph
MCNF
d
2 alternate valid paths
minimal path/surface candidates in primal corresponding to saturated dual edges
saturated dual edges
dead end path
separate patch
extract min cost surface
e
minimal path/surface
Prism
2D horizon functions as surface boundary
f
g
h

Figure 3.11: The computation pipeline for our global optimization based horizon extraction approach. The pipeline consosts of five major steps. The graph structure is defined as shown in ⓐ, costs and capacities for the edges are defined in ⓑ. The initial surface is created as shown in ⓒ, ⓓ shows the result of the MCNF computation and finally ⓔ the resulting optimal surface.

each edge (Figure 3.11ⓑ). In this step, a cost of 1 is used for all edges (not indicated in the figure). The capacities of the dual edges correspond to the costs of the primal facets and are computed using Equation 3.19 in Section 3.4.5. The edges contained in the outer facets in the graph, have to be treated separately. These edges do not have all four adjacent voxels and thus the cost cannot be computed using the cost function. We initialize these edges with infinite capacity. Edge capacities are indicated in Figure 3.11ⓑ by the thickness of the edge. At this point, there will be no flow in the graph, because all edges have positive cost. In the second step, the initial surface z_0 is added to the graph. The initial surface is a set of facets in the primal, bounded by the closed contour obtained from the prism sides. In Figure 3.11ⓒ, the boundary is indicated by the two purple primal nodes, the initial surface by the path between these nodes. To induce flow through the initial surface, negative costs are assigned to the dual edges corresponding to the primal facets of z_0. To allow all possible paths, the cost is the negative of the sum of all positive costs in the graph, such that every path through z_0 is negative and thus reducing total cost for the circulation. Additionally, we allow flow through the surface only in one direction by cutting all edges in the opposite direction. This guarantees that no cycles going back and forth through the surface are generated. Here it becomes obvious why we assign infinite capacity to the outer edges in the first step. All allowed cycles will go through the initial surface and the inner edges in one direction, and come back on the (much fewer) edges on the faces of the prism. If the capacity of these edges were limited, the algorithm would most likely terminate, delivering a set of saturated edges on the outside of the prism, which would not be helpful for finding the minimal-cost surface.

For most image segmentation approaches, the initial 2D trace will be performed on one slice in the volume, resulting in a planar boundary. In that case, the part of the slice bounded by the obtained 2D trace is the simplest match for the initial surface z_0. The 2D trace in our approach, does not result in a single planar boundary, however, a very simple initial surface can be constructed dividing the surface into four planar parts. First we cut the prism above the highest point in the trace with an orthogonal slice, resulting in a triangle shaped boundary in that slice. This triangle functions as the cover of our surface. The other three parts are on each side of the prism, bounded by the initial trace on the bottom, the cover slice on the top and the prism edges on the sides. Figure 3.11ⓖ shows a sketch of an initial surface fitting a 2D horizon path on the sides of a prism, the cover is depicted in light, the sides in dark cyan, the 2D trace on the prisms sides by the purple curve.

For the actual MCNF computation, we use the LEMON C++ graph library [1], which can compute the flow for all edges in the graph. This is used to identify the saturated edges in the graph.

3.4.4 Extracting the Surface from the Saturated Graph

The set of saturated edges does not translate directly to the desired minimal cost surface. In real world datasets, usually a certain amount of edges not contributing to the minimum cost surface are saturated. Figure 3.11ⓓ shows the cases of saturated dual edges which have to be removed. Dual edges/primal facets not connected to the initial boundary could simply be avoided by growing the surface from the initial boundary. However, dead end paths/surface patches, connected to the surface would not be removed by growing.

Instead, we prune facets by checking that all four of the facet's edges are either shared with another facet candidate, or are part of the initial boundary. By iterating over all facets and discarding facets which do not fit these criteria, the set of surface candidates is gradually reduced. Once a pass over all facet candidates finishes without finding any more facets that need to be discarded, the remaining facets form the minimal-cost surface and the algorithm returns (Figure 3.11ⓔ/ⓗ). If two alternate surfaces bounded by the initial contour exist (top left part of the path in Figure 3.11ⓓ), both must be of the same cost and thus are equivalent solutions. As the user can always force one of these we just use the first complete closed surface found by the algorithm.

3.4.5 Cost Function

For the global optimization to produce meaningful results, a proper cost function must be designed to assign low costs to pixels/voxels with a high probability of belonging to a seismic horizon and high costs otherwise. Horizons are marked by strong reflections in the seismic data. These can be identified by the scalar value only, or more precisely by looking at the local neighborhood. The seismic cube is constructed by a set of one dimensional traces or waves. Horizons are indicated in this data by local extrema of the waveform. In the following, we construct a cost function which is based on the scalar values as well as the local waveform. We use the same cost function for the contour extraction in 2D by assigning the cost to each edge, derived from the pixels at the two ends of the edge, as well as for the surface extraction in 3D by assigning the cost to the capacity of the dual edges. The dual edges correspond to facets in the primal graph, connecting four voxels. The cost is thus derived from the gray values as well as the local waveform of all four corners of the facets.

We define edge and facet weights using a cost function containing two major components. The first component g_{snap} defines the *snappiness* of the surface to ridge and valley lines/surfaces in the image/volume. The snappiness term defines the likeliness of each of the corresponding pixels/voxels belonging to a horizon surface based on the scalar value, as well as the local waveform at that pixel/voxel. The second component g_{smooth} of the cost function is important for the *smoothness* of the traced line/surface. The smoothness term is supposed to avoid large jumps of the scalar value within a single edge or facet. Therefore it is defined by the similarity of the voxels belonging to the edge/facet in question. The higher the difference of voxel grey values, the higher the cost. Both components are combined using a linear combination. If needed, the relative weight of the two cost function components can be adjusted to reach a smoother result or one that is closer to the strongest reflection.

For n-dimensional images the dimensionality of the boundary items in the primal graph are always of dimension $n - 1$. In 2D the boundary is defined by a start and end node, in 3D by a set of edges forming a closed contour. In the dual, however, the bounding item is always an edge. Thus, we define the cost using the scalar values $f(x, y, z)$ of the set of pixels/voxels (x, y, z) in the neighborhood $\mathcal{N}(e)$ of an edge e in the dual graph. The neighborhood is defined by the pixels or voxels, which share the edge e as an outer edge (compare Figure 3.12). For the two dimensional case $\mathcal{N}(e)$ contains two pixels, in 3D four voxels.

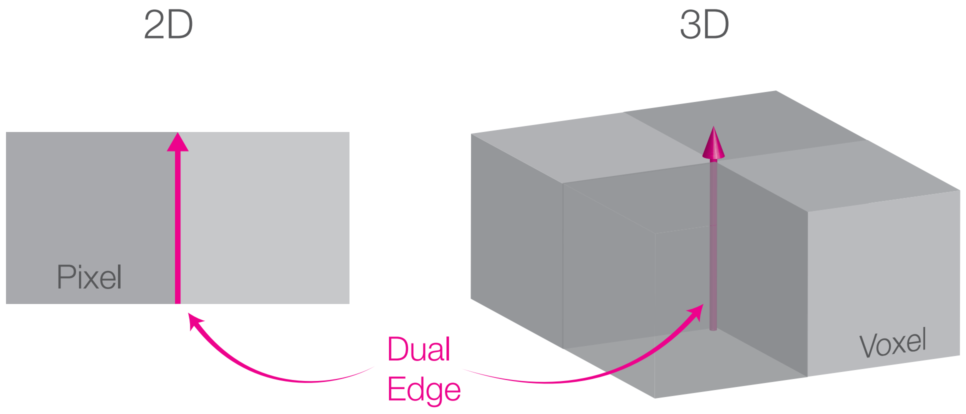

Figure 3.12: The dual edges in 2D and 3D. In 2D the two adjacent pixels are used to compute the cost for the edge, in 3D the four neighboring voxels.

As described above, we define the snappiness component by a combination of the scalar value as well as the local waveform. We define a scalar value-based term g_{gray} as well as a waveform-based term g_{wave}. The cost $g_{\text{gray}}(e)$ for an edge e is simply defined by the difference of the scalar values of the neighboring voxels and a predefined target value t:

$$g_{\text{gray}}(e) = \sum_{(x,y,z)\in\mathcal{N}(e)} \left|t - f(x,y,z)\right|, \tag{3.8}$$

where $t = 1$ for tracing maxima and $t = -1$ for tracing minima, assuming a scalar value range of $[-1..1]$. Figure 3.13ⓐ shows a plot of the scalar value and the corresponding normalized cost for an exemplary seismic trace.

The cost $g_{\text{wave}}(e)$ is supposed to map local extrema of the seismic trace to low costs. The obvious approach to such a term would be to compute the derivative, e.g., via central differences, to find extrema, and then use the result of the central difference computation as the cost. In addition, one could modulate the result to enhance the extrema; for example, using a smooth bump function such as:

$$\phi(v) = \begin{cases} \exp^{-\frac{1}{1-v^2}} & \text{for } |v| < 1 \\ 0 & \text{else,} \end{cases} \tag{3.9}$$

where v is set to the derivative $f_z(x,y,z) = \partial f(x,y,z)/\partial z$ scaled with a user-defined scale factor α to define the threshold for mapping the result to zero. Figure 3.13ⓑ shows the plot of the cost defined as:

$$g_{\phi}(e) = \sum_{(x,y,z)\in\mathcal{N}(e)} \Big(1 - \phi\big(\alpha \cdot f_z(x,y,z)\big)\Big). \tag{3.10}$$

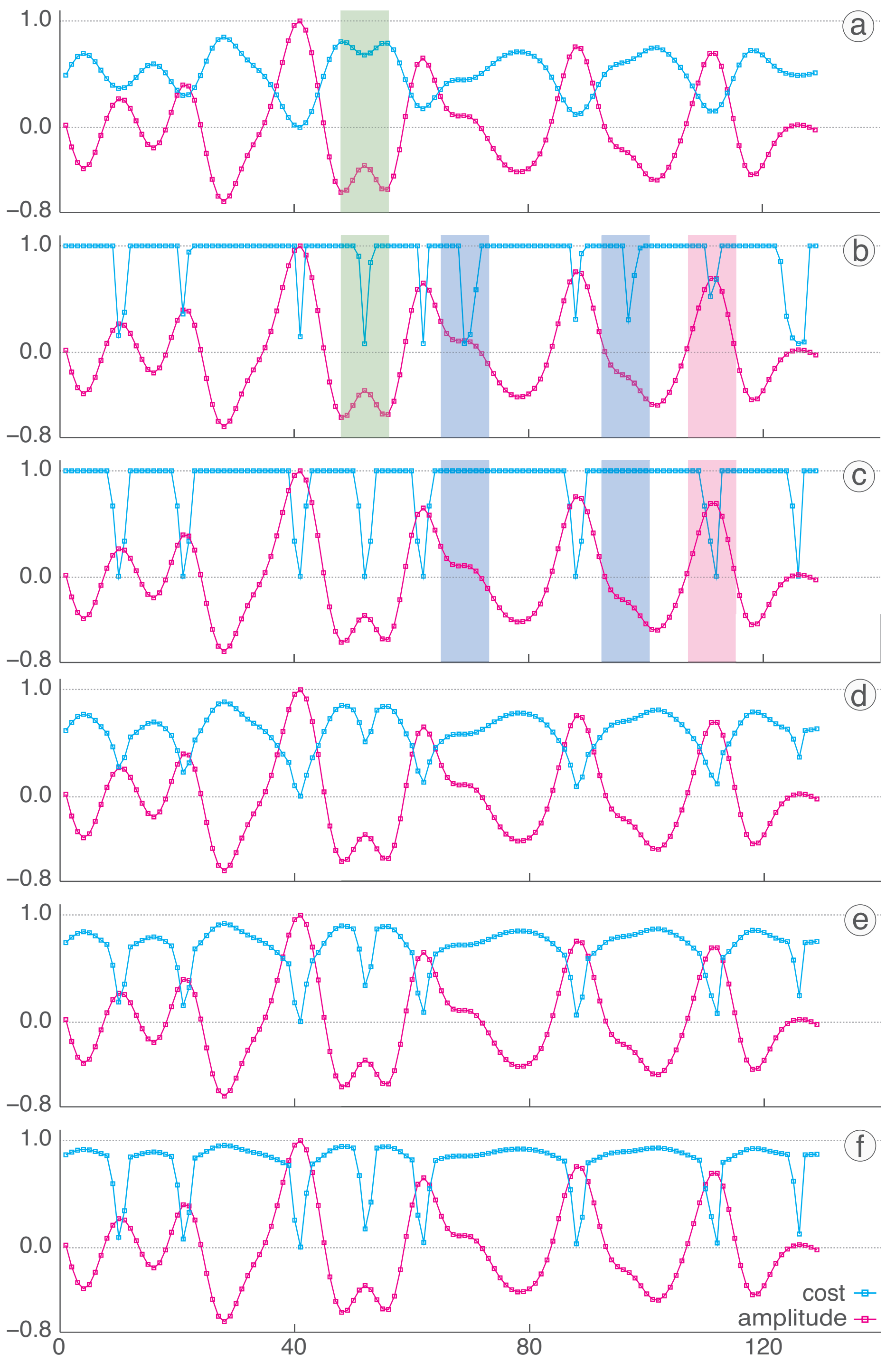

Figure 3.13: Comparison of the cost obtained via the components of the snappiness term. ⓐ shows the gray value based component g_{gray} (Equation 3.8). The derivative-based term is shown in ⓑ (Equation 3.10), and the final non-linear term for g_{wave} in ⓒ (Equation 3.11). ⓓ - ⓕ show the final snappiness term (linear combination of ⓐ and ⓒ, Equation 3.15) with $p_0 = 0.25$, $p_0 = 0.5$ and $p_0 = 0.75$, respectively.

For the plot, minima are canceled out using the second derivative. This is already a good result. The sharp features are desired and some local maxima, that are not assigned a low cost using g_{gray} are tagged correctly (compare for example the small local maximum marked by the green box). However, some problems become obvious in the plot. While minima can be canceled out effectively using the second derivative, this is not true for saddles, resulting in undesired low costs at the two areas highlighted by the blue boxes. In addition, the strong maximum marked with the magenta box was assigned a relatively high cost due to the fact that it has two samples on its peak which results in an asymmetry of the samples around the peak.

These shortcomings can be removed by the use of the following non-linear waveform-based term to replace g_{ϕ}:

$$g_{\text{wave}}(e) = \sum_{(x,y,z)\in\mathcal{N}(e)} \left(1 - \sum_{k=1}^{m} \varphi_s(x,y,z,k)\right), \tag{3.11}$$

where m is a predefined 1D neighborhood size, and

$$\varphi_s(x,y,z,k) = \begin{cases} \varphi(x,y,z,k) & \text{if } (k \geq s) \text{ or} \\ & \quad (k < s \text{ and } \varphi(x,y,z,k+1) \neq 0) \\ 0 & \text{else,} \end{cases} \tag{3.12}$$

with

$$\varphi(x,y,z,k) = \begin{cases} \frac{1}{n} & \text{if } f(x,y,z-k) < f(x,y,z) \text{ and} \\ & \quad f(x,y,z+k) < f(x,y,z) \\ 0 & \text{else,} \end{cases} \tag{3.13}$$

for maxima, or

$$\varphi(x,y,z,k) = \begin{cases} \frac{1}{n} & \text{if } f(x,y,z-k) > f(x,y,z) \text{ and} \\ & \quad f(x,y,z+k) > f(x,y,z) \\ 0 & \text{else,} \end{cases} \tag{3.14}$$

for minima, respectively. This cost function is a simple step function which basically returns a smaller value the closer the current sample point is to a local extremum in the predefined neighborhood, and 1 if there is no extremum in the neighborhood. The additional constraint in φ_s provides an implicit smoothing, using s to define the minimal feature size.

The resulting cost-plot is shown in Figure 3.13ⓒ. As can be seen, the problems for the derivative-based term are canceled out in this plot, while the sharp features for the maxima are retained as desired.

With g_{gray} and g_{wave} in place, g_{snap} is now simply computed by a linear blending of both normalized terms, with a user adjustable parameter p_0 between 0 and 1:

$$g_{\text{snap}} = p_0 \cdot g_{\text{gray}} + (1 - p_0) \cdot g_{\text{wave}} \tag{3.15}$$

Figures 3.13ⓓ - ⓕ show results for p_0 equaling 0.25, 0.5 and 0.75 respectively. While the sharp features of g_{wave} are very desirable when the data is clear, the fact that the cost is always 1.0 in between the detected features can lead to unpredictable results in unclear regions. Adding g_{gray} to the cost function provides additional guidance in these areas.

The smoothness component is much simpler. It simply describes the similarity of all pixels/voxels adjacent to the current edge, similar to the standard deviation, by computing the average

$$\text{avg}(e) = \frac{1}{|\mathcal{N}(e)|} \sum_{(x,y,z)\in\mathcal{N}(e)} f(x,y,z) \tag{3.16}$$

with $|\mathcal{N}(e)|$ the number of pixels/voxels adjacent to the edge (two in 2D, four in 3D) and building the sum of the differences.

$$g_{\text{smooth}}(e) = \sum_{(x,y,z)\in\mathcal{N}(e)} \left| f(x,y,z) - \text{avg}(e) \right|. \tag{3.17}$$

Just like the snappiness term before, g_{smooth} and g_{snap} are normalized and combined according to a user adjustable parameter p_1 between 0 and 1:

$$g_{\text{combined}} = p_1 \cdot g_{\text{snap}} + (1 - p_1) \cdot g_{\text{smooth}}. \tag{3.18}$$

Finally we introduce a third parameter p_2, to influence the effect of the length of the path or the area of the surface on the total cost. The path length (or surface area) is encoded implicitly in the global optimization. Since the cost for the complete path is the sum of all its segments, a longer path with the same average cost for each segment is always more costly than the shorter path. p_2 is designed to let the user modify the implicit cost of the path length. Since we compute heightfields the number of horizontal segments is constant, while vertical segments are variable and thus define the length of the path. By adjusting the weight of vertical segments we can effectively adjust the cost of longer paths and thus influence the flexibility. The final cost function is thus

$$\text{cost}(e) = \begin{cases} g_{\text{combined}}(e) & \text{when e is horizontal} \\ p_2 \cdot g_{\text{combined}}(e) & \text{when e is vertical,} \end{cases} \tag{3.19}$$

or in its complete form

$$\text{cost}(e) = p_1 \cdot \big(p_0 \cdot g_{\text{gray}} + (1 - p_0) \cdot g_{\text{wave}}\big) + (1 - p_1) \cdot g_{\text{smooth}} \tag{3.20}$$

for the horizontal case and

$$\text{cost}(e) = p_2 \cdot \Big(p_1 \cdot \big(p_0 \cdot g_{\text{gray}} + (1 - p_0) \cdot g_{\text{wave}}\big) + (1 - p_1) \cdot g_{\text{smooth}}\Big) \tag{3.21}$$

for the vertical case.

3.5 Results

Figure 3.14 shows some exemplary surfaces extracted with the presented system, as well as comparisons to reference surfaces extracted manually by our domain expert partners. While the extracted surfaces seem to be very promising results we conducted an expert evaluation as described below to find out how well our system performs under real world conditions.

3.5.1 Evaluation

We have evaluated our system in a real-world scenario with our domain expert partners, in order to compare our workflow with the industry standard as described below.

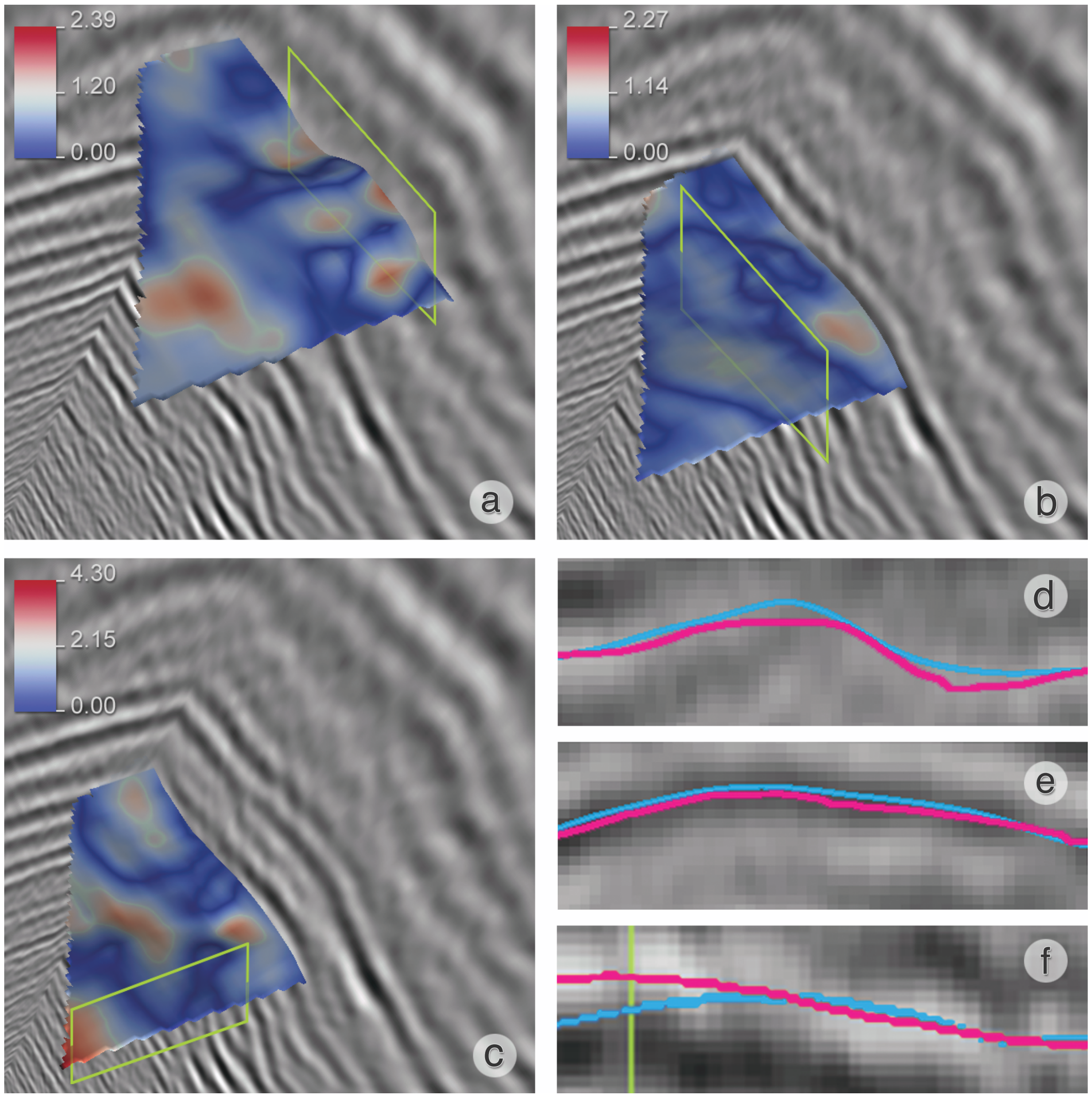

Figure 3.14: Three horizon patches computed using our algorithm. ⓐ, ⓑ and ⓒ show the distance in pixels from a manual trace of the same horizon. ⓓ, ⓔ and ⓕ show detailed slice view cutouts of the surface indicated by the green boxes in ⓐ, ⓑ and ⓒ. Manual traces are in cyan, traces computed with our method in magenta. ⓓ shows a region of the first horizon, with > 2 pixel difference, where the manual trace is clearly better than the automatic trace, manual and automatic traces in ⓔ are very similar. ⓕ shows a part of the horizon with > 4 pixel difference. Here, the automatic trace is closer to the actual ridgeline.

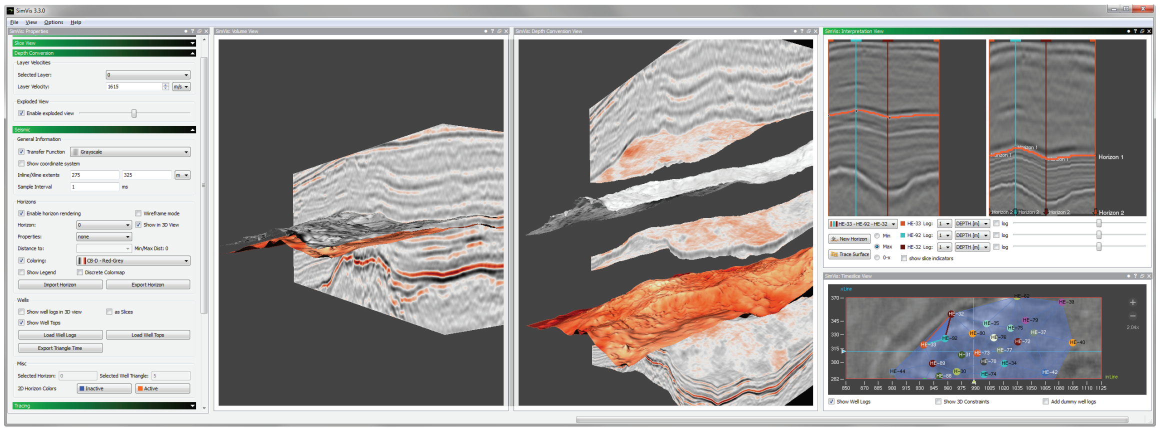

Layer Velocities
Selected Layer: 0
Layer Velocity: 1615 m/s
Exploded View
[✓] Enable exploded view
General Information
[✓] Transfer Function: Grayscale
[ ] Show coordinate system
Inline/Xline extents: 275 325 m
Sample Interval: 1 ms
Horizons
[✓] Enable horizon rendering
[ ] Wireframe mode
Horizon: 0
[✓] Show in 3D View
Properties: none
Distance to:
Min/Max Dist: 0
[✓] Coloring: CB-D - Red-Grey
[ ] Show Legend
[ ] Discrete Colormap
Wells
[ ] Show well logs in 3D view
[ ] as Slices
[✓] Show Well Tops
Misc
Selected Horizon: 0
Selected Well Triangle: 5
2D Horizon Colors: 🟦 Inactive 🟧 Active

Figure 3.15: A screenshot of our application illustrating our novel joint time/depth domain visualization for a seismic reflection dataset with two interactively interpreted seismic horizons. The two 3D views on the left show volume renderings of the seismic in time and depth domain, respectively, cut open at the horizons. The two 2D views on the top right show our interpretation views in time and depth as well. The 2D slice view on the bottom right shows the reflection data from the top in combination with well positions.

Setup

For comparison, we asked our partners to provide us with a typical application scenario. To avoid an interpretation session over several days with our expert partner we asked for a rather small dataset. We were provided with a moderately-sized dataset consisting of 325 inlines and 275 crosslines at 151 samples per trace. The dataset covers an area of roughly 7.5×6.5km in western Hungary. Time between samples was 4ms. In addition to the seismic cube, we were provided with a total of 39 well positions, with well tops for two horizons each, of which five were available in depth and time, and the remaining 34 in depth only. A large part of the dataset was covered by the resulting triangulation. We added 10 more positions so that it is possible to create the interpretation up to the volume's boundaries without falling back to a slice-based approach. A screenshot of our application with the data described above loaded is shown in Figure 3.15.

The task for the interpreter was then to interpret the horizon defining the top boundary of a clay layer throughout the volume. Well tops indicating the top and bottom boundaries of this layer were provided. Velocity modeling is usually done using well logs. Using our joint time/depth workflow, the interpreter could simply adjust the velocity values such that the well tops available in time and depth were matching. For comparison, we gave the expert one hour with our workflow, and one hour with the standard workflow using the Petrel [100] software framework, and asked to create an interpretation, as complete as possible, without sacrificing exactness. A comparison of the resulting interpretations is shown in Figures 3.16 and 3.16. Table 3.4 shows timing comparisons of the different steps. For quality comparison, we were provided with the actual interpretation of the same horizon used for production, which was created manually over several working days.

Before starting the evaluation, we gave our partners an in-depth introduction to our framework and provided guidance during a test drive with a different dataset for several hours. Even though we also supervised the actual evaluation run, the expert was able to work on his own and did not ask for any further assistance.

We conducted a second evaluation session to get an indication of how well our approach scales to larger datasets. For this test, we had two students with basic knowledge in seismic interpretation interpret a horizon in the large dataset introduced above. The dataset measures $1422 \times 667 \times 1024$ voxels and covers an area of roughly 17.8×8.3km. The sampling distance in depth was 2ms. We were provided with 15 well tops in spatial depth and six in time, covering the center of a salt dome. The outer region was covered by triangulating arbitrary positions defined by the students. The task was to interpret a horizon above the salt dome. The resulting area of interest was a rectangle above the salt dome, measuring roughly 800×600 pixels. For comparison, we were provided with a production surface of the same area which was created in roughly two working days by our domain experts.

Joint Time/Depth Domain Workflow

After the test drive, the domain expert decided to approach the interpretation task in the following way: First, he adjusted the velocity model to match the well tops available in the time as well as depth domain. Then he started with seeding a horizon at one prism and adjusted the 2D curve on the prism side. Using the live depth conversion, he was able to directly match the interpretation to the well tops regardless of the domain they were available in. In the background, our system would use the intermediate interpretation to recursively create interpretations on the neighboring prisms as well as compute the optimal surface on the inside. After being satisfied with the current prism, the expert would then proceed to a neighboring prism and check the precomputed curve and adjust it if necessary. The expert was able to go over all prisms in well under one hour. After finishing the complete horizon, he quickly checked the result by skimming inlines and crosslines and looking at the extracted horizon overlaid with the amplitude. He then proceeded to adjust a few imprecisions resulting from the 3D optimization. After the last change, the expert had to wait only for a few seconds for the final result, as the optimization runs continuously in the background.

Conventional Workflow

For the comparison run, the expert interpreted the same horizon using Petrel, which is the industry standard software for geological modeling. The software offers automated tracing on 2D slices, as well as in 3D. From what we could gather, from testing these automated approaches are both local. Starting from a seed in

2D, or an interpreted slice in 3D, the horizon is propagated into as many neighboring pixels/slices as possible. When the data is ambiguous, the auto-tracer stops. It is also not possible to set constraints besides the initial seed. If the interpretation is wrong, it needs to be fixed manually and 3D traces between two interpreted slices do not necessarily connect these slices. When doing the interpretation, the expert started out with a single slice and fully tagged the horizon on this slice using a combination of piecewise auto-tracing and manual intervention for corrections, as well as to connect the automatically traced parts at areas where the automatic approach stopped. After that he used the 3D auto-tracer for a first result. Besides the described disadvantages of using a local approach, a big advantage compared to our global approach is that the auto-tracer computes a result nearly instantly. However, according to our expert the resulting surfaces are far from complete and need thorough inspection. As a result they are used mostly for guidance during a manual interpretation rather than for directly producing final results. After this first slice, the expert gradually refined the interpretation by manually adjusting every tenth slice followed by another 3D trace. After 60 minutes, the expert finished 18 slices in steps of ten slices, covering roughly 60% of the dataset.

Comparison

Figures 3.16 and 3.17 show comparisons of the created surfaces. For the manually interpreted part, it can be seen that the results of both approaches are quite similar. The lower third shows the part that was not reached within the time frame. There, large holes and also a phase jump can be seen, which clearly shows that the automatic tracing alone is not sufficient to reach acceptable results with the conventional workflow. After the 60 minutes, we also measured the time for computing the velocity model and the deformed seismic cube (see Table 3.4).

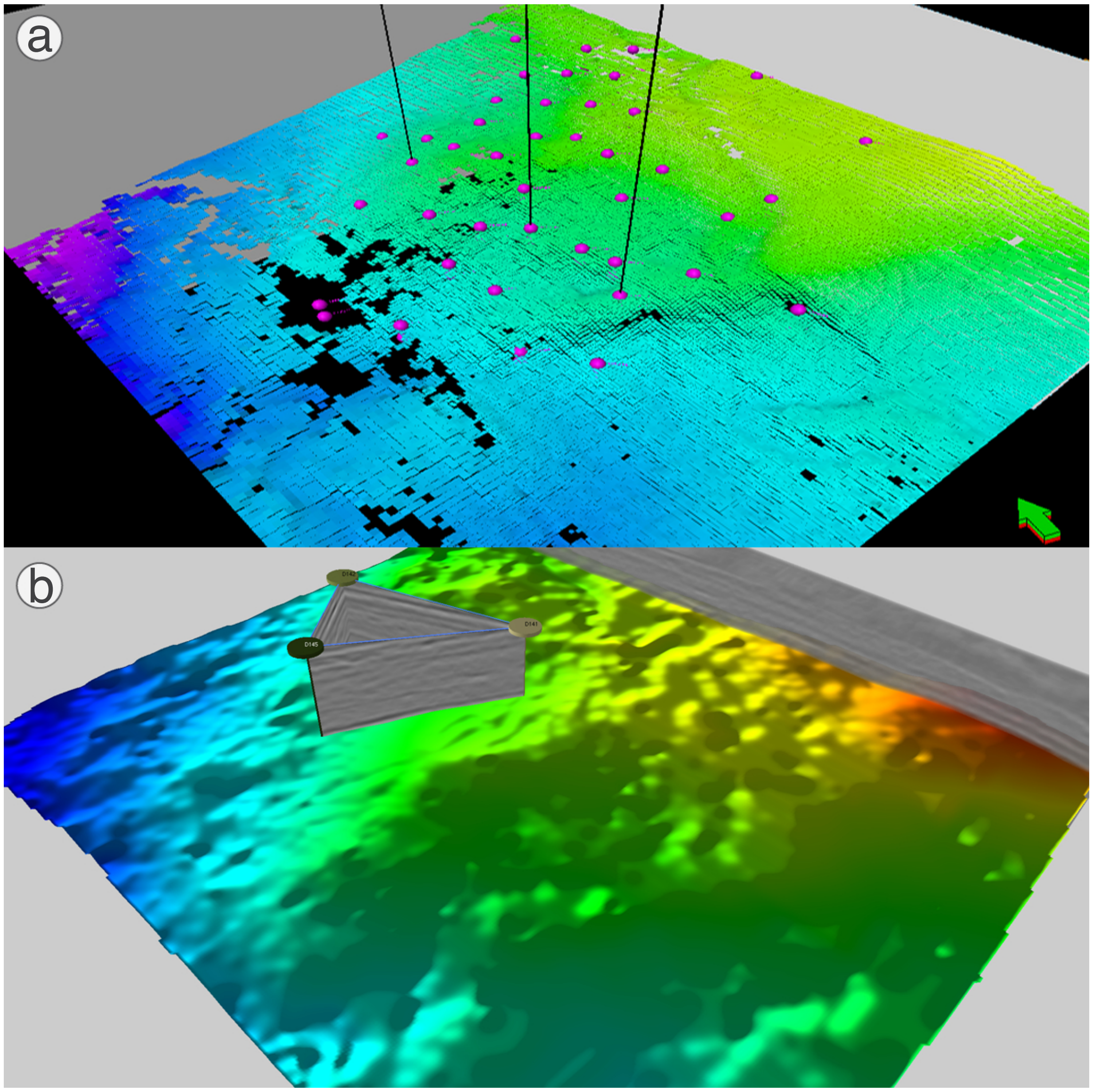

Figure 3.16: Comparison of the horizons extracted during the expert evaluation. ⓐ shows a screen capture of Petrel with the extracted surface using the conventional workflow. ⓑ shows the result using our workflow. The relative height is encoded in the surface coloring, but with slightly different colormaps for ⓐ and ⓑ. We imported the result from Petrel into our application to compare it to our result (see Figure 3.17).

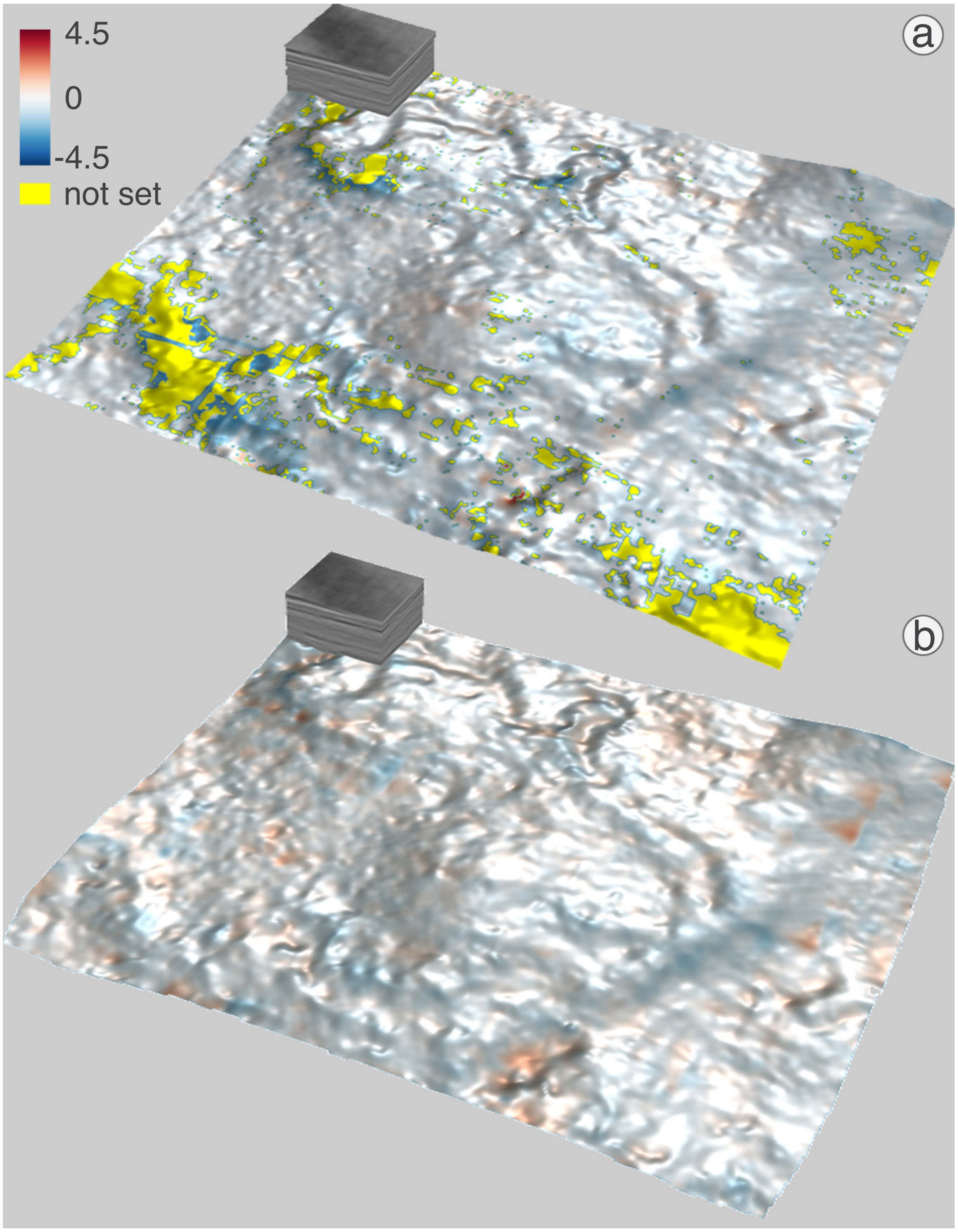

Figure 3.17: The results shown in Figure 3.16 compared to a ground truth interpretation. ⓐ shows the result from Petrel, with gaps in the surface marked in yellow, ⓑ shows our result.

Task	**Petrel**	**SeiVis**
Initial Interpretation	> 60min*	≈ 45min
Velocity Computation	21s	on the fly
Depth Conversion	29s	on the fly
Refine	n/a+	< 10min
#Slices/Prisms	18*	63
Avg. Time per Slice/Prism	3:20min	43s

*With the Petrel software the expert was able to finish 18 slices (about 60% of the dataset) before the time limit of 60 minutes.
+Not reached before the time limit of 60 minutes.

Table 3.4: Timings for the interpretation process. Initial Interpretation corresponds to a first complete extraction of the horizon. Velocity- and DC Computation correspond to the time needed to compute the velocity cube and the depth conversion, respectively. Refine describes the time used by the expert to refine the automatic interpretation between the manually interpreted slices and inside prisms after the first complete run.

After the interpretation, we conducted a brief interview with the expert. The expert was impressed by the live depth conversion in combination with the prism-based workflow. Having three well tops on each 2D slice and being able to match the interpretation directly to the tops in the depth domain was really helpful in finding the correct surfaces. A big advantage of the global optimization used for the automatic tracing is the possibility to set constraints and force the auto-tracer through defined points. Also, it will always result in a closed surface even when the data is unclear. A point that we did not expect was made by the expert that the prism-based approach was also very motivating in contrast to the standard approach of going from slice to slice. The data on nearby slices is often very similar, making slice-based interpretation a very tedious process so that subtle, but important, changes are sometimes missed by the interpreter.

Student Evaluation

Since the second evaluation session was carried out by students rather than experts we do not want to make any claims regarding the quality of the extracted surfaces besides the fact that all important structures were found by the students and are visible in the resulting surface (compare Figure 3.18).

After a brief introduction, both students were able to work on their own. The two students approached the dataset slightly differently. Student 1 added 25 additional pseudo well positions to cover the area of interest outside the provided well tops. The result were rather large prisms used for the surface extraction. Student 2 added roughly 100 additional points resulting in much smaller prisms. As a result, Student 1 spent only about two and a half hours on the extraction of the horizon on the prism sides, but had to wait about an hour for the computation of the 3D

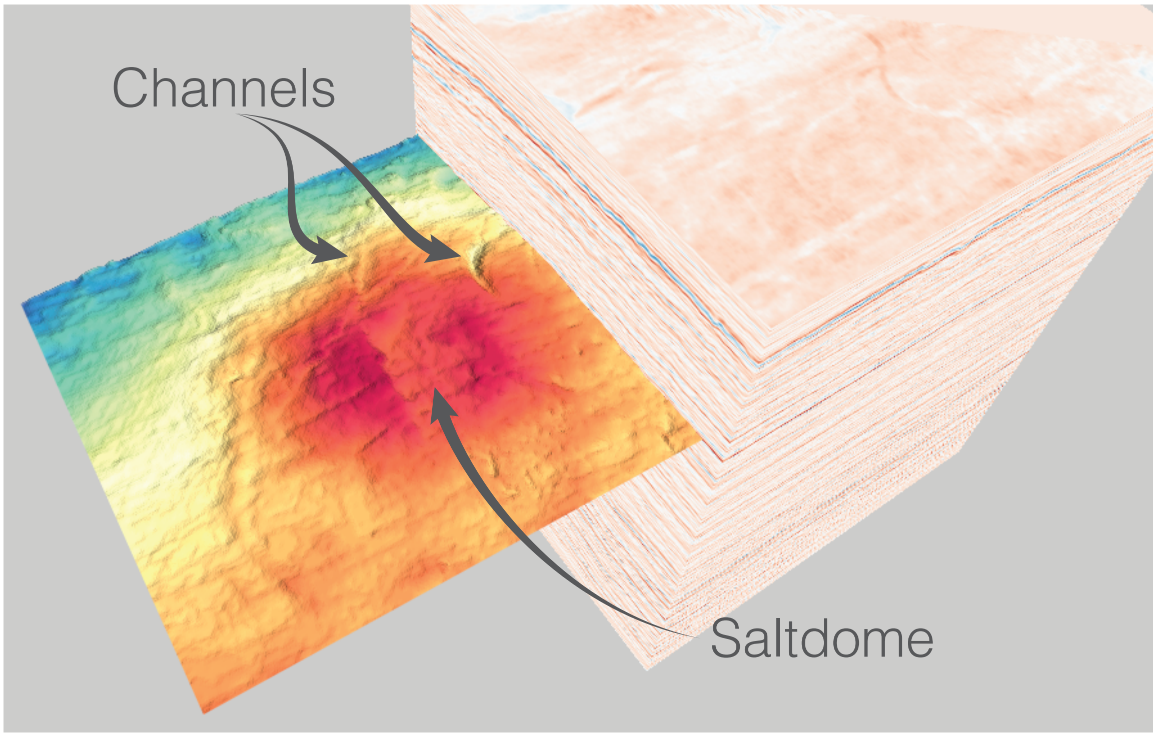

Figure 3.18: Screenshot of the $1422 \times 667 \times 1024$ voxel dataset. The horizon surface, which was interpreted during our evaluation, clearly shows the important features, a large saltdome in the center and adjacent two channels, of the dataset.

surface. Student 2 on the other hand spent about four hours tuning the horizon on the large amount of prisms, but since the computation on the smaller prisms ran much faster, Student 2 barely had to wait for the computation.

Conclusion

We can say that the expert was able to work with our system on his own after a short introduction. He was able to extract surfaces close to manual interpretations in a very short time. While we used a small dataset with the domain expert, we show that the presented approach scales well for larger datasets with the additional student evaluation. Being able to match an interpretation in the time domain to ground truth data in the depth domain has two advantages. First it speeds up the interpretation process significantly and secondly it allows for very exact results without tedious back and forth between the different domains. By using asynchronous computations in the background, it is also possible to minimize waiting times for the interpretation, even though the global optimization technique is much more computationally demanding than local approaches. Following the evaluation, our partners installed our application on a testing system where it is now used for experimental projects.

3.6 Conclusion

In this chapter we have presented an interactive workflow for rapid interpretation of seismic volumes using a combination of 2D and 3D cost minimization techniques. The main contributions are a novel joint time/depth domain workflow for creating subsurface models, merging time and spatial depth domains using on-the-fly volume deformation, and the integration of these techniques into an integrated workflow for seismic interpretation and depth conversion. The workflow guides the user through the interpretation process using a combination of multiple linked 2D and 3D views. The prism-based workflow, instead of working along inline and crossline directions only, was received very well by our collaborators. It bounds the size of the working volume, and allows incrementing the piecewise optimal horizon surface bit by bit, by subsequently appending additional optimal surface patches that were created by processing neighboring prisms. For the actual horizon extraction, we presented a global optimization technique that integrates very well into our workflow. Decoupling the interaction in 2D and the eventual computation in 3D was also perceived very well by the experts, as it simplifies user interaction and time expenditure considerably. Additionally, our approach is scalable to large seismic volumes, because the time needed for computing minimal-cost paths and surfaces depends on the size of the selected prism instead of the volume size. We conducted an expert evaluation that clearly shows the advantages of this new workflow.

Chapter 4

Visual Parameter Space Exploration for Horizon Extraction

This chapter is based on the short paper *Extraction and Visual Analysis of Seismic Horizon Ensembles* [36], and in parts on the paper *Visual Analysis of Uncertainties in Ocean Forecasts for Planning and Operation of Off-Shore Structures* [39].

In the previous chapter, we introduced a novel workflow for extracting seismic horizons. Since seismic data is very noisy and often exhibits ambiguous features, the workflow is specifically designed to allow the user to interact with the results of the automatic computations at any time, for example by placing constraints or changing the parameters for the cost function, triggering immediate updates of the computed surface patches. One weakness of this approach is arguably the complicated cost function. While it is very powerful, and allows the creation of very good segmentations with the right parameter settings, tweaking three parameters to find a good fit can overburden the user. For this reason, we propose to sample the parameter space of the cost function automatically, and create an ensemble of surfaces for each horizon.

Section 4.1 gives an overview of the ensemble computation. In Section 4.2 we present the statistical analysis which builds the foundation for the visualization of the ensemble data (Section 4.3). The computation and rendering pipeline is explained in Section 4.4 in detail. Results can be found in Section 4.5.

4.1 Ensemble Computation

To start the ensemble computation, only a single seed point is required. However, an arbitrary number of points can be defined as additional constraints to force the resulting surfaces through user-specified positions. The same seed point and set of constraints are used to compute all surfaces in the ensemble. Once the seed point and constraints are defined, the user can define a range and sampling rate for each parameter to compute the ensemble. For each parameter setting, the seed point and constraints, as well as the parameterized cost function, are given to the surface extraction algorithm. The surface extraction is then carried out for each parameter set as described in the previous chapter, however without any user interaction. Since the surfaces for each parameter setting are computed independently from all others, the ensemble computation can easily be parallelized for faster computation of the ensemble data.

The result of each surface extraction step is a single horizon surface represented as a height field or function $f : \mathbb{N} \times \mathbb{N} \mapsto \mathbb{R}$, mapping each (x, y)-position on a regular grid to a single depth value. Even though we focus on height fields in this work, our approach would also be applicable to generic surfaces, as long as correspondences between the ensemble members can be established. Here we assume that the (x, y)-position defines this correspondence.

4.2 Statistical Analysis

To analyze the results of the ensemble computation, we compute a range of basic statistical properties. The basis for these computations is provided by a 3D histogram, $h : \mathbb{N} \times \mathbb{N} \times \mathbb{N} \mapsto \mathbb{N}$, mapping each volume position (x, y, z) to the number of surfaces passing through that position. With the (x, y)-position as the correspondence between ensemble members, as described above, this 3D histogram resembles a set of 1D histograms mapping each depth value at any given (x, y)-position to the number of surfaces passing through that depth. As such, after normalization this histogram can also be interpreted as a probability distribution. Due to the fact that all surfaces in an ensemble share the same domain, we know that the sum of all surfaces passing through all depth values at any (x, y)-position equals the number of ensemble runs. We can therefore directly derive a probability for each voxel being part of a horizon surface, by dividing the number of surfaces passing through that voxel by the number of ensemble runs.

In addition, we estimate the probability density distribution for each (x, y)-position by computing the kernel density estimate. Based on this data, we compute a *maximum likelihood surface*. This surface is an actual surface from the ensemble, which is chosen according to an overall likelihood value assigned to each of the surfaces. This likelihood value is computed by taking the height- or function-value $f(x, y)$ at each (x, y)-position of the surface f, and summing over all the individual probabilities on the surface, which result from a look-up in the probability density function (pdf) at each position:

$$\text{likelihood}(f) = \sum_x \sum_y \text{pdf}(x, y, f(x, y)). \tag{4.1}$$

The ensemble member with the highest likelihood value is then defined as the maximum likelihood surface. This surface corresponds to a global measure, in contrast to a surface such as the mean surface, where each point is only locally the point of highest probability.

By interpreting the 3D histogram as a set of 1D histograms, we can also compute a complete set of statistical properties per (x, y)-position, such as mean, standard deviation, or kurtosis. These properties can be divided into two sets. Mean and median depth value, as well as the maximum mode of the pdf result in a height value for each (x, y)-coordinate. By combining these additional surfaces can be synthesized. Other properties, such as variance or skewness result in scalar values which are not part of the original domain. These can be used to augment the surfaces, for example by texturing the surface with the color-mapped scalar field or by extracting iso contours.

4.3 Ensemble Visualization

The surface distributions resulting from the ensemble computation have significantly different properties than distributions common for ensemble data resulting from simulations or, for example, the probabilistic iso-surfaces presented by Pfaffelmoser et al. [80, 81] or Pöthkow et al. [87, 88]. Whereas the distributions of the

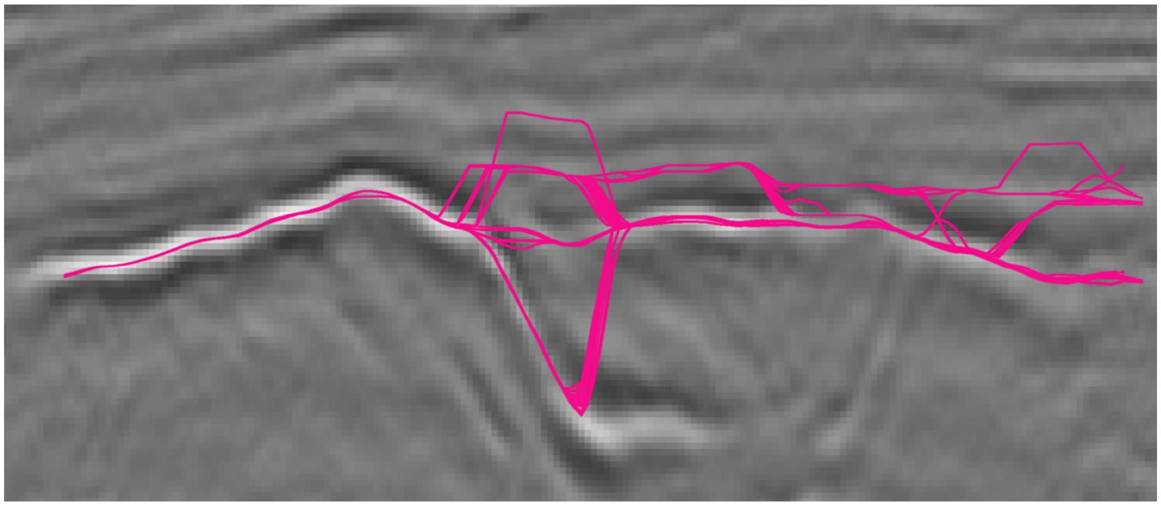

Figure 4.1: Cut sections of all surfaces of one ensemble rendered into a single slice view with reduced opacity. It is clearly visible that on the left side there is close to no variation. On the right side, the surfaces spread and form several clusters of very similar surfaces. This behavior is very different from a Gaussian distribution, which is often assumed by probabilistic approaches. Here, however, a mean surface, which would be the perfect representative for a Gaussian distribution, would lie between the clusters and would not correspond to any desired horizon surface.

latter can usually be modeled as a Gaussian distribution, each parameter setting in our approach can produce a completely different surface. In fact, typically there is very little variation as long as the surfaces tag the same horizon. In uncertain areas, however, it often happens that different parameter settings lead to surfaces tagging different horizons, which results in disconnected clusters of very similar surfaces in each cluster. This behavior is clearly visible in the example shown in Figure 4.1. Here cut sections of all surfaces from one ensemble are blended on top of a seismic slice. The clustering is clearly visible. Thus, the visualization techniques presented by Pfaffelmoser et al. and Pöthkow et al. [80, 87] are not applicable for our ensembles. That is, the mean surface used in these approaches as a representative surface would not correspond to a horizon surface, since it would likely result in a surface in between two possible segmentations, but tag neither one correctly.

Instead of synthesizing a surface, we have decided to extract the maximum likelihood surface for use as the representative of the ensemble, as described in Section 4.2. A comparison of the maximum likelihood surface and a mean surface can be seen in Figure 4.2. Figure 4.2a shows an example of a maximum likelihood surface. Even though there is a somewhat large variance in the ensemble, the maximum likelihood surface fits the underlying data quite well. In contrast, the mean surface shown in Figure 4.2b is basically a mixture of two large clusters of surfaces and does not fit either one of the tagged horizons for large parts of the surface. Even though the median surface is typically very similar to the maximum likelihood surface, we prefer the maximum likelihood surface for another reason. As this surface is an actual result of the optimization, we can use it as a basis to further edit the surface, e.g. by adding constraints, without recomputing large parts of the surface.

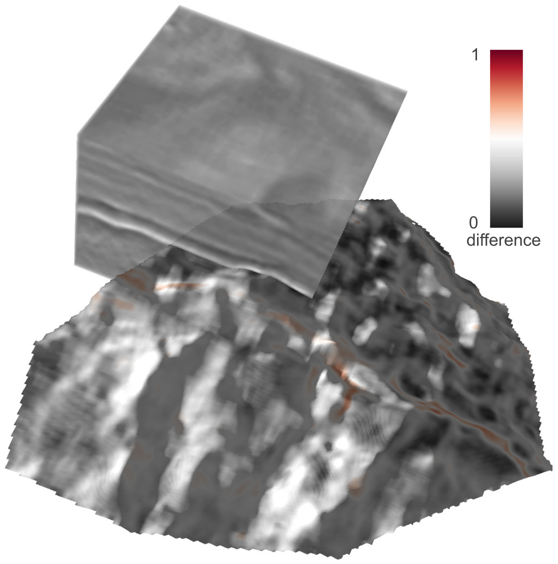

(a) Maximum likelihood surface

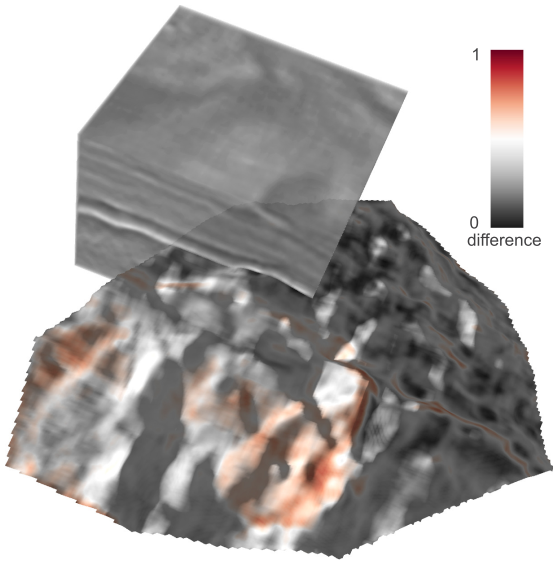

(b) Mean surface

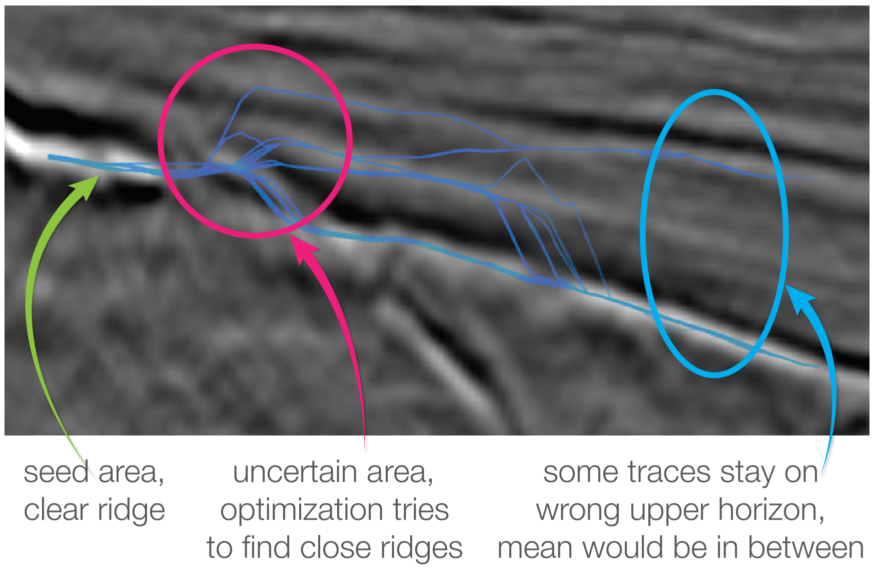
seed area, clear ridge
uncertain area, optimization tries to find close ridges
some traces stay on wrong upper horizon, mean would be in between

(c) Cut section of the complete ensemble

Figure 4.2: Comparison of the maximum likelihood surface (a) with synthetic mean surface (b). The color coding indicates the difference between the amplitude at the volume position passed by the surface and the targeted amplitude. Black means a small difference (better), red a bigger difference (worse). It is clearly visible why the mean surface is not suitable in this case. Whereas the maximum likelihood surface is a good fit for the ridge line for large parts of the surface, the front part of the mean surface shows large difference values. (c) shows cut sections of all surfaces of one ensemble rendered into a single slice view with reduced opacity. The multimodal distribution causing the bad results for the mean surface shown in (b) can be seen clearly.

However, simply displaying the maximum likelihood surface itself without any additional information does not provide much information about the ensemble. Therefore, we also depict the results of the statistical analysis described in Section 4.2. In the standard setting, we compute what we call *virtual* surfaces from the mean, median, and maximum mode from each (x, y)-position. *Virtual* here means that we do not render these as surfaces, but only use them in order to compute the distance to the maximum likelihood surface for each (x, y)-position. These distances are then color-coded and used to texture the maximum likelihood surface. If desired by the user, however, these virtual surfaces can also be rendered directly.

We allow pseudo-coloring the surface with these results, using one of several pre-defined, or user-defined color maps. These properties immediately provide a good idea about how the surface extraction behaves in different areas, i.e. very stable areas are clearly visible throughout all properties, indicated by small values in range, standard deviation, variance, close to zero values in the skewness, or very large values in the kurtosis. In addition, it is possible to automatically animate all surfaces in a pre-defined range. Animating the ensemble gives a nice impression of the parameters that result in similar surfaces, as well as of which areas in the dataset react more or less to changes in the parametrization of the cost function. Similar surfaces or surface parts in the ensemble will result in little variation in the animation, whereas areas of large variance will show more movement and thus automatically draw the user's attention. An example for this can be seen in Figure 4.3.

All the described techniques have in common that they can be used to visualize the complete ensemble or any user-defined subset. Using a set of sliders, the user can define a subrange for each parameter, and the statistical analysis is carried out on the fly for this range. This allows an interactive exploration of the parameter

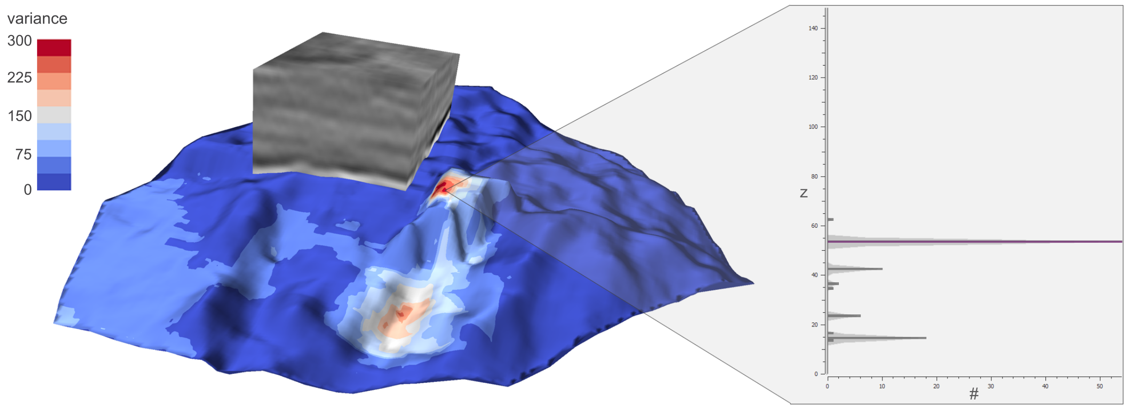

Figure 4.3: Visualization of a horizon ensemble using the representative surface augmented with the variance color-coded on the left and the histogram of a selected position on the right.

space, which is helpful to define interesting ranges for each parameter. To allow this live exploration of the parameter space, we implemented an efficient, completely GPU-based pipeline for computing the statistics as well as rendering the results, as presented in Section 4.4.

The same pipeline also allows efficient implementation of a number of other features. If desired, the user can choose to render any surface from the ensemble. This requires no data transfer to or from the GPU, except for the ID of the surface in the ensemble to render. In addition, it is possible to automatically animate all surfaces in a predefined range. In the presented application this can be useful in two ways; As shown by Brown [12], as well as Lundström et al. [57], animation is a powerful tool for visualizing uncertainty. The user can choose to animate through all members of a single time step to get an impression of the surface distribution.

The described visualization techniques can give a very good impression of the quantitative variation in the data. Detailed information on the surface distribution can be gained by animating through or manually selecting individual surfaces from the ensemble. However, it is hard to compare more than two surfaces this way. We therefore provide an additional view showing the histogram and probability distribution for a selected position. The position to investigate can be picked directly in the 3D view. To facilitate easy comparison, we color the bin corresponding to the current representative surface differently than the remaining bins. An example for the histogram is shown in Figure 4.3 on the right.

4.4 Computation and Visualization Pipeline

To allow interactive exploration of the parameter space, all updates of the statistical analysis must be computed in real time, or at least at interactive rates. For this reason, we employ a statistic computation and visualization pipeline that is entirely GPU-based, as presented in the next section.

Our GPU-based analysis and visualization pipeline is illustrated in Figure 4.4. In the remainder of this section, circled numbers refer to this figure. The pipeline is divided into two main parts: The statistical analysis and iso surface extraction is carried out using CUDA, while the visualization is based on OpenGL and GLSL shaders. All data are shared between the two parts of the pipeline, so that after the initial upload of the ensemble onto the GPU no expensive bus transfer is necessary.

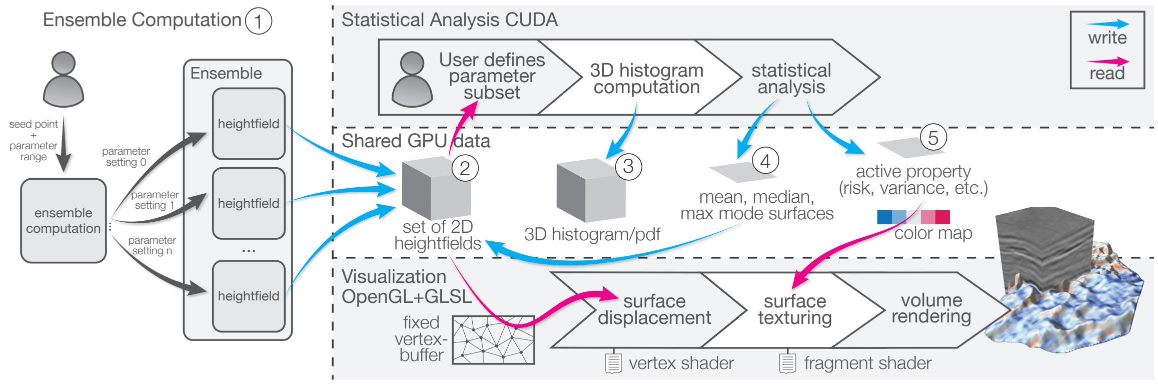

Figure 4.4: The pipeline for our framework is divided into three major blocks: The ensemble computation (left), the statistical analysis part at the top, and the rendering part shown at the bottom. The resulting surfaces of the ensemble computation are loaded into GPU memory where they are shared between the CUDA-based analysis and the OpenGL based visualization pipelines.

Since usually only a small part of the ensemble is required by the visualization, a streaming approach would be possible for datasets that are larger than GPU memory, but we currently assume that the dataset fits into GPU memory.

Ensemble Computation

The input to our system is a set of heightfields resulting from the ensemble computation ①. Even though we focus on heightfields in this work, our approach could also be applied to surfaces in n dimensions as long as the correspondences between all surfaces in the dataset are known for every nD-datapoint. In our framework, we assume the 2D spatial (x, y)-coordinate to be the correspondence between the surfaces.

Data Representation

Before computation of statistics or visualization, the ensemble is converted into a 3D texture ② and loaded onto the GPU. Every heightfield of the ensemble will be represented by one slice in this texture. Additionally, space for the mean, median and maximum mode heightfield will also be reserved in this texture. The surfaces are indexed using the original parametrization. If there is only a single parameter, for example the time steps in a time series, the surface ID corresponds to the texture index. For higher-dimensional parameter spaces, as in our case the three parameters from the cost function (Section 3.4.5), the linear texture index is computed from the original parameters. This allows the user to define subranges for each parameter separately in order to examine the influence of each of the parameters on the segmentation individually.

Statistical Analysis

The first step in the statistical analysis is the creation of the 3D histogram ③. Changes in the parameter range trigger an update of the 3D histogram and subsequently of the representative surface and property texture. Since each ensemble member provides exactly one entry to the histogram per (x, y)-position, rather than using a thread for each member, we use one thread per (x, y)-position. Each thread then loops over all selected surfaces and computes the complete 1D histogram for this position. This way, write conflicts can be avoided and no critical sections or atomic operations are needed. The kernels for the derived properties are set up in a similar fashion. The desired statistical property is computed by one thread per (x, y)-position. The main difference to the histogram computation is that this results in a single scalar per thread, all of which are then assembled into a 2D texture. While mean, median and maximum mode ④ are attached to the 3D heightfield texture to be used as representative surfaces, the other properties ⑤ are copied into a 2D texture available to the visualization pipeline for texturing the surface. Exploiting the parallelism of the GPU and eliminating costly bus transfers between CPU and GPU allows interactive modification of the parameter range even for ensembles containing several hundred surfaces.

Rendering

The rendering pipeline takes advantage of the fact that all ensemble data are already stored in GPU memory, which facilitates efficient surface rendering. Instead of creating new surface geometry every time a different surface of the ensemble is rendered, a single generic vertex buffer of fixed size is created. This buffer covers the entire (x, y)-domain, but does not contain any height information. The

z-value of each vertex is set later in the vertex shader. Before transforming the vertex coordinates into view space, the object space (x, y)-coordinates of the vertex in combination with the ID of the active surface are used to look up the z-value of the current vertex in the ensemble texture. At this point, the desired surface geometry is available. In order to be able to visualize the results of the statistical analysis, the object space coordinates are attached to each vertex as texture coordinates (x and y are sufficient). In the fragment shader, this information can then be used to look up the active statistical property in the 2D texture. This texture contains the raw information from the statistical analysis, which is then converted to the fragment color by a look up in a 1D color map. We provide a selection of several continuous, diverging cool-to-warm color maps, as presented by Moreland [65], but also allow the creation of custom color maps. These color maps minimally interfere with shading, which is very important in this case, as shading is an important feature to judge the shape of a surface. During testing we realized that using the continuous version made it very hard to relate an actual value to a color in the rendering so we decided to optionally provide a discrete version with ten steps. After the surface geometry has been rendered, the seismic cube can be rendered on top, providing spatial context. This is done in a second rendering pass in order to guarantee correct visibility [98].

Detailed Inspection

We enable the detailed inspection of the ensemble with the linked histogram view as described in Section 4.3. The histogram view shows the 1D histogram of any position picked by the user directly in the main view. In fact, the histogram refreshes automatically when the user moves the mouse cursor over the representative surface. All information that is required for picking is already available in our rendering pipeline: We use the same vertex shader as described before for rendering the surface into an off-screen buffer of the same size as the frame buffer. Instead of using the object space coordinates to look up the scalar values in the fragment shader, we use the coordinates directly as the vertex color. This way, we can look up the current mouse position directly in the downloaded off-screen buffer. With the (x, y)-part of the resulting volume position, we can then directly look up the histogram and probability density distribution for this position.

4.5 Results

Figure 4.5 shows an example where the standard parameter setting for the cost function produces a wrong result due to large uncertainty in the data. While the incorrect result could be fixed by placing a constraint and recomputing the surface, the color coding of the cost (Figure 4.5a), which could indicate an uncertain area by large costs, gives no indication of this area. Instead of the cost, we use the standard deviation to texture the maximum likelihood surface resulting from the ensemble computation (Figure 4.5b). Using the standard deviation of the computed ensemble immediately leads to the very prominent area in the center.

A cut section through this area is given in Figure 4.5c. The blue line corresponds to the original surface and the green line to the maximum likelihood surface. Once we identified this region we could find a third surface, corresponding to the magenta line, by narrowing the parameter range and skimming through the remaining surfaces. Even though the differences between the maximum likelihood surface and this third surface are subtle (compare the overlay in Figure 4.5c), this third surface represents the underlying data slightly better than the maximum likelihood surface.

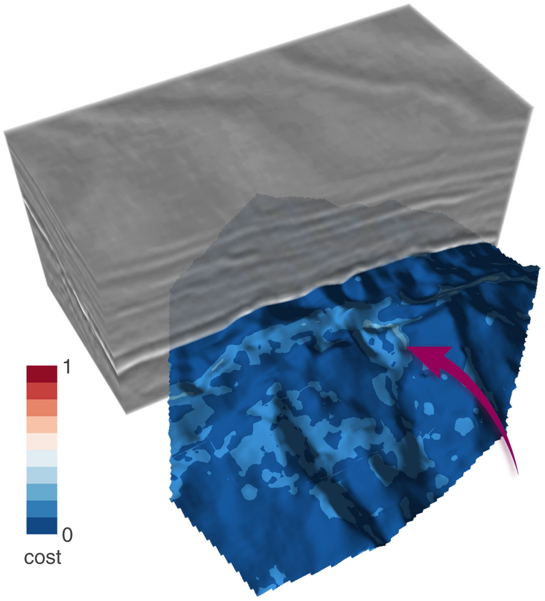

(a) Original surface.

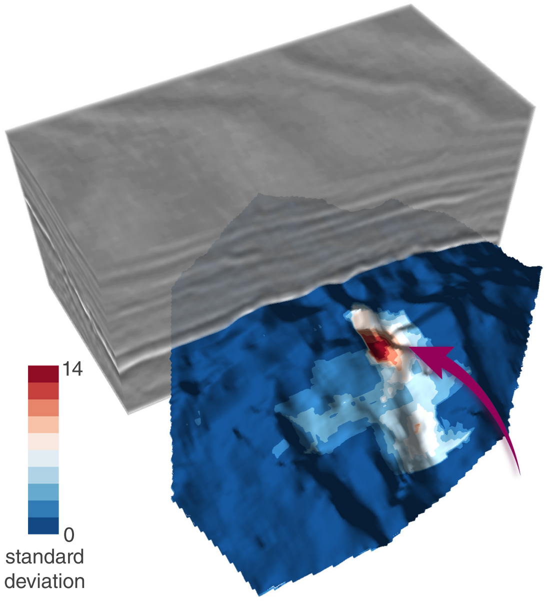

(b) Maximum likelihood surface.

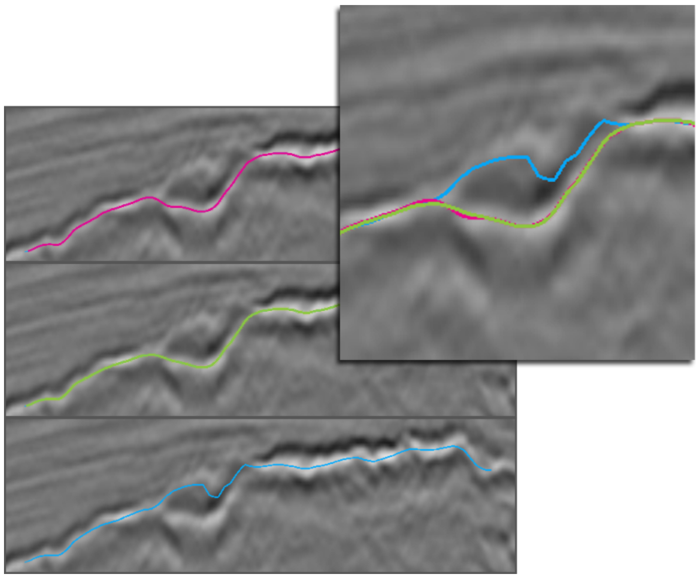

(c) Cut sections through the surfaces.

Figure 4.5: Surfaces extracted and visualized using our technique, described in Chapter 3 (a) and using the ensemble technique (b). While the cost (color coding in (a)) shows little variation over the surface and thus does not reveal problems in the segmentation, the standard deviation (b) clearly highlights an area in the center of the surface (compare the areas marked by the arrows). (c) shows a cut section of the surfaces, the blue line corresponds to (a) the green line to the maximum likelihood surface in (b). The magenta line corresponds to a third surface extracted from the ensemble using the proposed exploration framework.

Figure 4.6 shows visualizations of different ranges for the parameter p_1, with the other two parameters fixed. The variance is depicted by color coding the maximum likelihood surfaces of the respective parts of the ensemble. Judging from Figure 4.6a, which resembles the complete parameter range, it seems that there is quite a bit of variance as there are very few dark blue areas. By splitting up the parameter range into two sub-ranges, one from 0.9 to 1.0 (shown in Figure 4.6b),

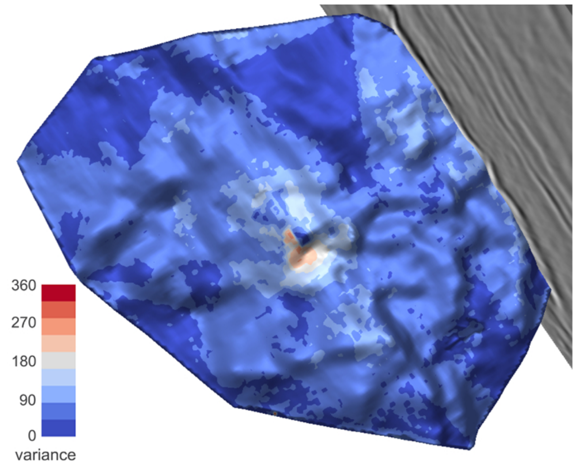

(a) $p_1 = [0.0..1.0]$

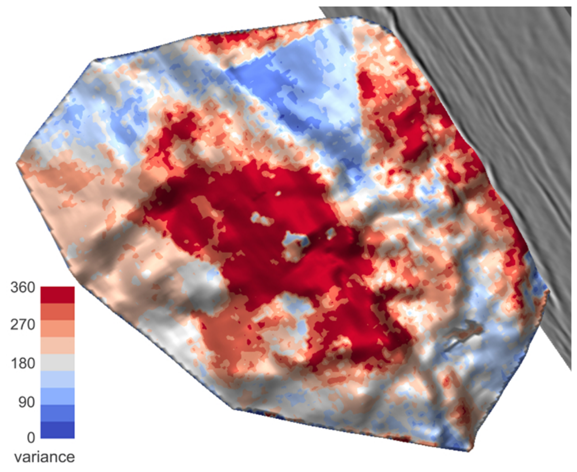

(b) $p_1 =]0.9..1.0]$

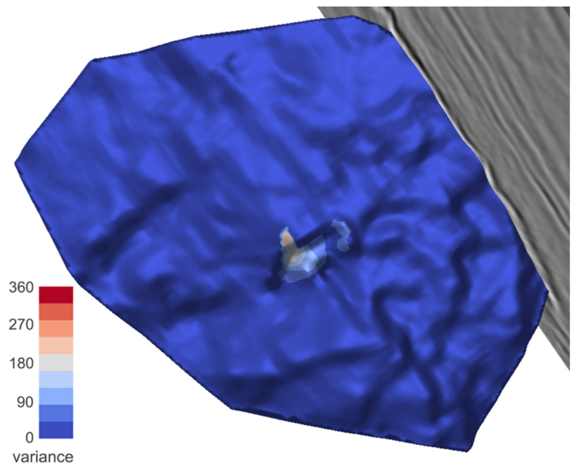

(c) $p_1 = [0.0..0.9[$

Figure 4.6: Exploration of the parameter p_1. 101 samples were taken in steps of 0.01 from 0.0 to 1.0. The color coding represents the variance of the ensemble. Only looking at (a), it seems that there is a quite large variance over the entire surface. However, by looking at the two different parameter sub-ranges in (b) and (c), respectively, it becomes clear that nearly all of the variation is related to the parameter range from 0.9 to 1.0.

and one from 0.0 to 0.9 (Figure 4.6c), it becomes clear that nearly all of the variation is in the upper ten percent of the parameter range.

By sweeping through the different subranges of p_1, we could quickly find out that the usable parameter range for p_0, for this specific dataset, is between 0.0 and 0.9, but also that a parameter in this range will have very little effect on the resulting surfaces, meaning that the user does not have to be very careful with this parameter, as long as it is between 0.0 and 0.9.

Finally, Figure 4.7 shows a selection of the computed statistical properties. Here the visualization shows all combinations of all three parameters sampled in steps of 0.1 from 0.0 to 1.0 for p_0 and p_2, while the range for p_1 was limited to $[0.0..0.9]$ for the reasons described above. This results in a total of 1210 surfaces examined. Figure 4.7a shows the range, Figure 4.7b shows the standard deviation, Figure 4.7c the variance, and Figure 4.7d the skewness. For the range, standard deviation and variance, the color map used indicates zero with blue, and large values with red. For the skewness, zero is set to white, blue tones indicate negative skew, and red tones positive skew. There are some notable differences between the range and the variance. Overall, there are a lot less very small values in the range texture Also, the large red region in the front left is not present in the variance. The variance helps filtering out small groups of outliers most likely leading to this region in the range texture. The highlighted area described in Figure 4.5 is also prominent in this ensemble for all four textures, even though not as strong for the range texture. Interesting is the distribution of the skewness. The mentioned highlight is clearly visible as a large area of negative skew. Another interesting feature in the skewness is also the strict clustering of negative and positive skewness.

To allow the interactive exploration of the parameter space, it is very important that the computation of the statistical analysis is possible at interactive rates.

With our GPU-based implementation we achieve these update rates on standard graphics hardware for hundreds of millions of data points.

Since the features of the computation pipeline presented in this chapter basically form a subset of the features used for our ocean forecasting application presented in Chapter 6, we refer to Section 6.5.1 for a detailed performance analysis.

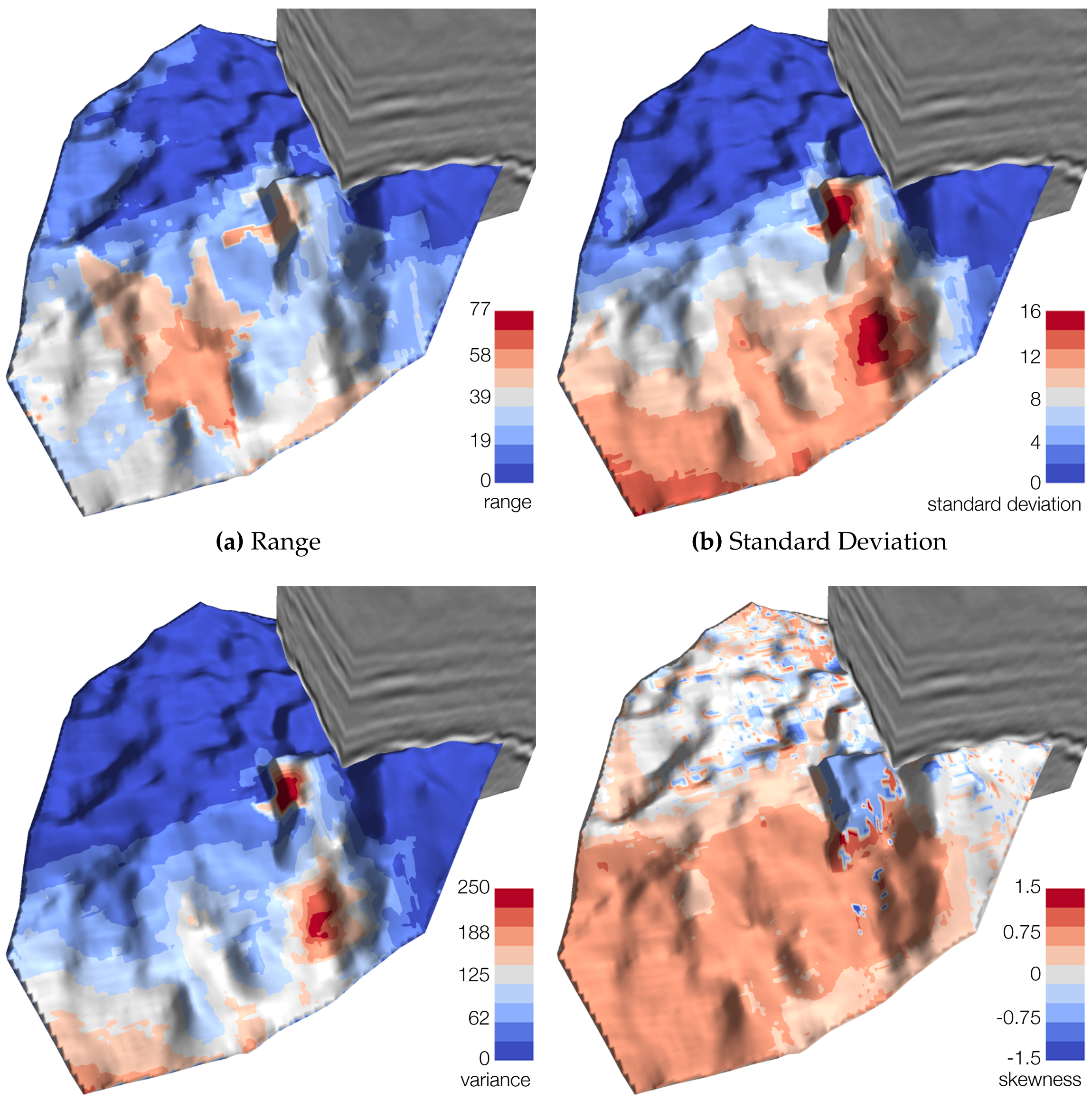

(a) Range **(b)** Standard Deviation

(c) Variance **(d)** Skewness

Figure 4.7: Comparing statistical properties of the ensemble, varying and sampling all three parameters.

4.6 Conclusion

In this chapter, we have presented a novel framework for the computation, analysis, and visualization of ensemble data consisting of extracted seismic horizon surfaces. By sampling the parameter space of the cost function, underlying the global optimization approach, presented in Section 3.4.3, we compute several segmentations for each horizon, which are then combined into an ensemble. These ensembles do not follow a Gaussian distribution. We perform a complete statistical analysis of the ensemble, and present a visualization pipeline for these ensemble data in combination with the results from the statistical analysis. The parameter space of the computed ensemble can be explored interactively to find optimal settings for the cost function. We have shown that our framework is helpful for identifying good parameter settings for the cost function, as well as for avoiding bad parameter settings. Our approach can also be used to find interesting features in the data, which might warrant closer manual interactive inspection.

Chapter 5

Enhancing Seismic Visualization

This chapter is based on the paper *SeiVis: An Interactive Visual Subsurface Modeling Application* [37].

Creating meaningful visualizations of seismic volume data is a hard task. Seismic volumes are dense, noisy and often exhibit ambiguous features. In this chapter we introduce two methods to enhance the visualization of these data. By adapting the cost function presented in Section 3.4.5 for the extraction of seismic horizons to rendering we created a shading technique (Section 5.1) that not only highlights these structures, but can also be used to prototype the cost function itself. In Section 5.2 we present an interactive single pass rendering technique to employ exploded views, an illustrative rendering technique that alleviates occlusion in dense data by cutting the data open.

5.1 Horizon Enhancing Shading

Inspired by the gradient magnitude-modulated shading presented by Levoy [53], and based on the cost function presented in Section 3.4.5, we have developed a shading approach that focuses on highlighting horizon structures. While in horizon extraction local waveform inspection is common, to our knowledge this is the first attempt to exploit the local waveform for enhancing volume rendering of seismic data.

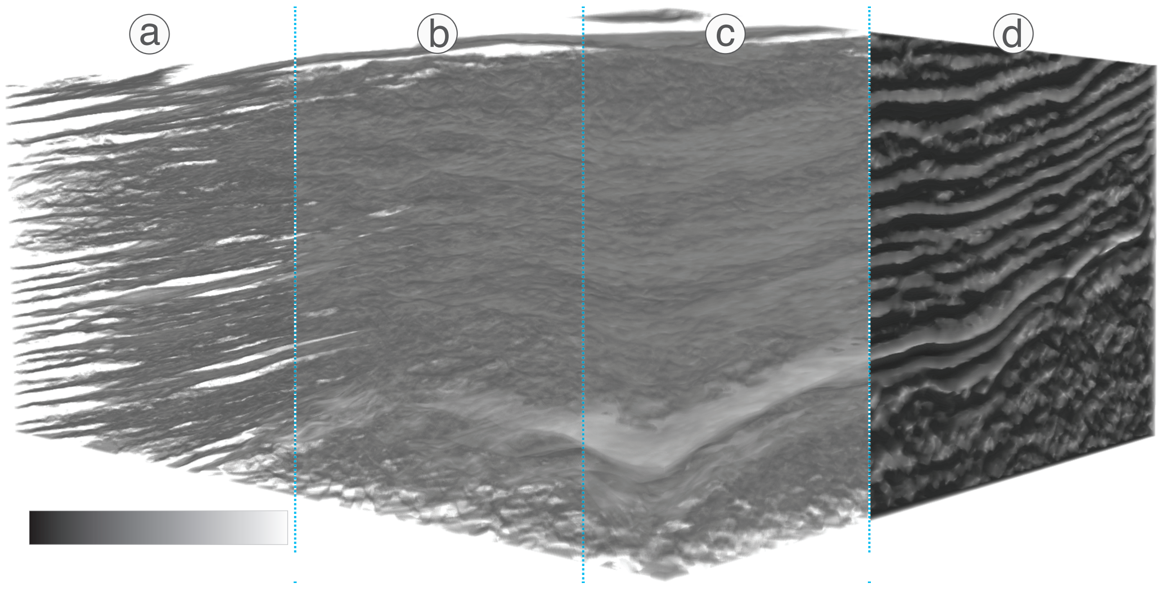

Figure 5.1: Different kernel sizes for the cost-modulated shading (ⓐ: $k = 1$, ⓑ: $k = 2$, ⓒ: $k = 3$), and comparison with Phong shading ⓓ.

Common illumination models use the gradient for shading. For visualizing horizons, this is not suitable as the gradient vanishes at the local extrema indicating the horizons. Instead, we compute the inverse of the wave form based component of the local cost on-the-fly during rendering, and use it to modulate the opacity from the transfer function, in the same way as the gradient magnitude is used for gradient magnitude-modulated shading [53].

Using the non-linear filter g_{wave} described by Equation 3.11 in Section 3.4.5, we can roughly estimate the distance of the current sample to a local minimum or maximum in the seismic trace. While the cost function term shown in Equation 3.11 maps extrema to low cost for the rendering, we would like to assign large opacity to the extrema and low opacity to the remaining data. Where Levoy uses the magnitude of the gradient in 3D directly to modulate opacity and shading intensity, we can use the term from Equation 3.12, describing the *peakness* in the trace direction, to modulate the opacity during volume rendering. Equation 3.12 contains the parameter k, defining the neighborhood size that is considered. For rendering, this

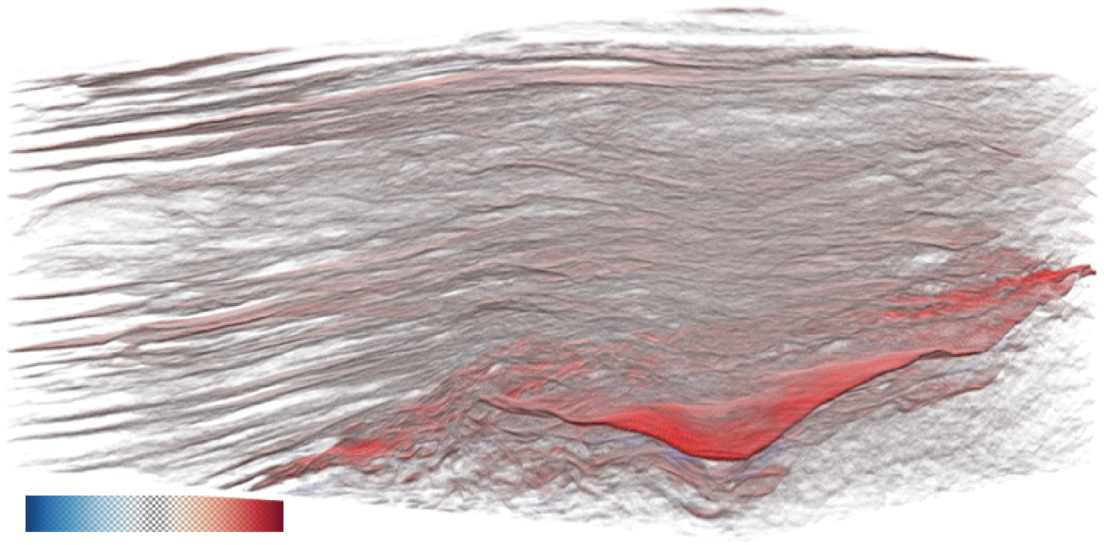

Figure 5.2: An example of a visualization of a seismic cube highlighting reflections of positive amplitude. With a very simple transfer function the most important features can be highlighted (Note the strong reflection in the bottom right area, as well as the distinct features on the left side.)

value influences the visual quality of the results, but since here the term needs to be evaluated on the fly during raycasting, it also has a notable effect on the rendering performance.

Figure 5.1 shows a comparison of the quality with different neighborhood sizes, as well as a comparison to standard Phong shading without any opacity modulation. The transfer function is a simple gray map with constant opacity for all renderings. A big advantage of this approach is that horizons can efficiently be highlighted without adjusting the transfer function. While similar results could be achieved with a carefully designed transfer function with amplitude-based shading, using the proposed render mode requires no user interaction at all.

Figure 5.2 shows another rendering of the same dataset. We used a diverging blue to red color map, typical for seismic applications, as transfer function with reduced opacity in the center. The shader was setup to only highlight local maxima. The visualization clearly shows the classified horizons as very distinct features,

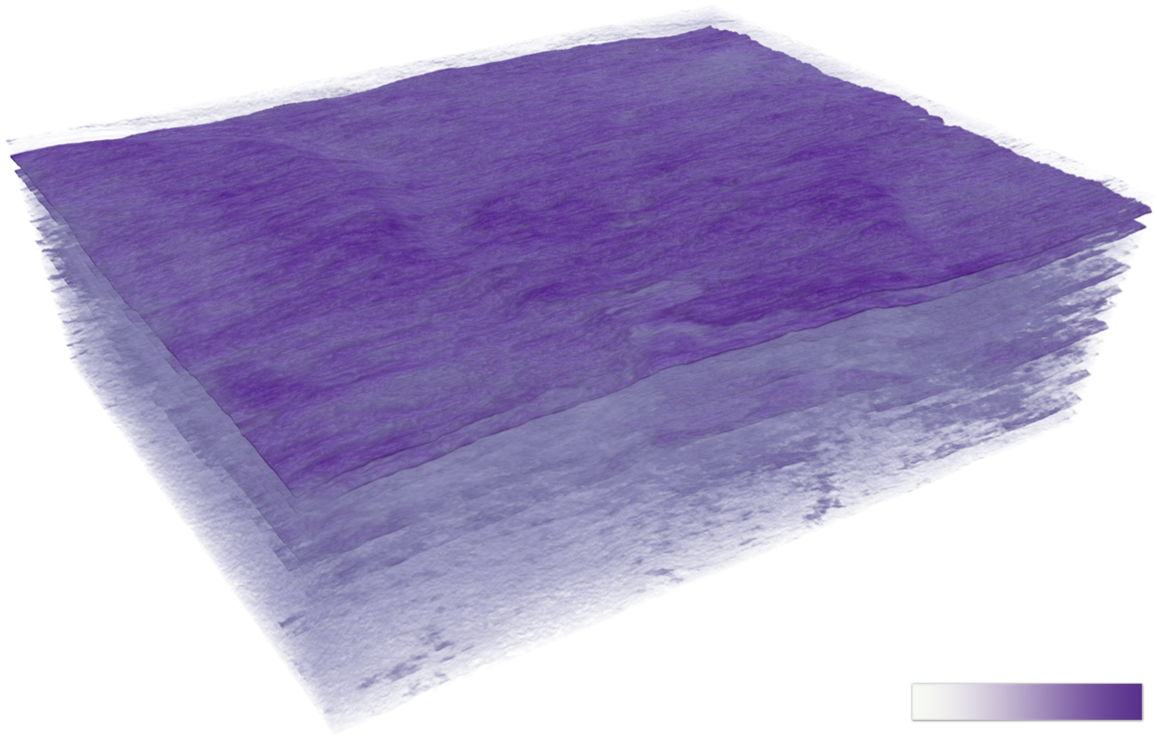

Figure 5.3: An example of a horizon extracted using the horizon enhancing shading only, without any preprocessing. The volume was clipped slightly above the horizon. The structure is clearly visible over the complete area of the dataset.

especially on the left side. A strong reflection on the right side is also very prominent in dark red. On major advantage of our waveform based classification over amplitude only based classification can be seen in this rendering. The highlighted features cover a wide range of amplitudes, visible in the coloring. Using a simple amplitude based transfer function, it would not be possible to highlight a lot of the lower amplitude features, indicated by gray coloring.

A performance comparison for $k = 1$, $k = 2$, and $k = 3$ is shown in Table 5.1, compared to a shader using standard Phong shading without modulation. It can be seen that, while there is a performance loss for neighborhoods larger than three voxels, rates are still interactive. For the performance comparison, we adjusted the transfer functions such that transparency was similar for the standard and

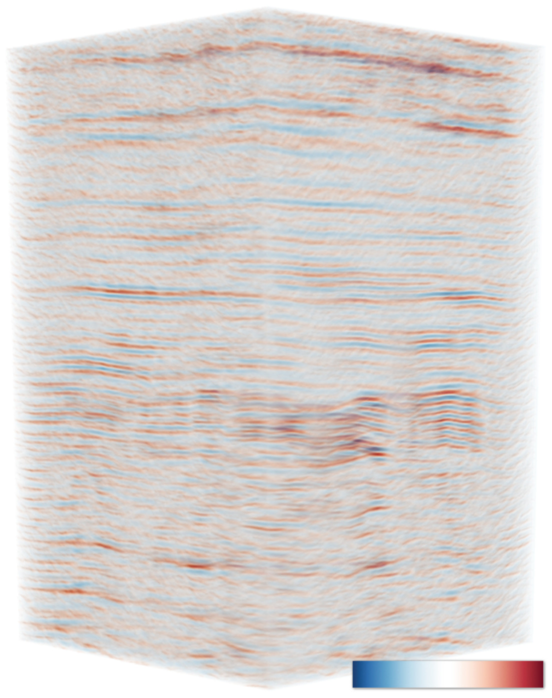

(a) $p_0 = 0.25$

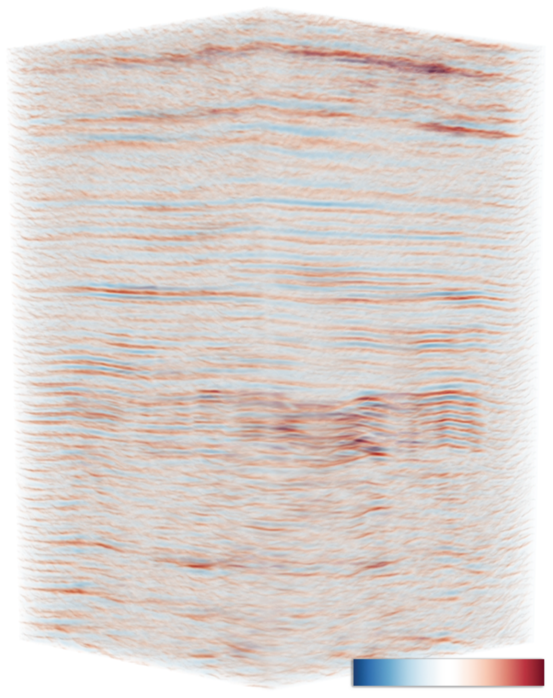

(b) $p_0 = 0.5$

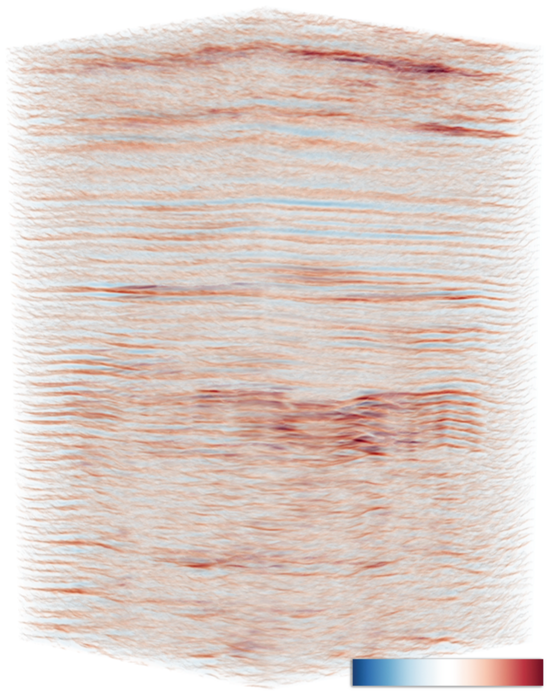

(c) $p_0 = 0.75$

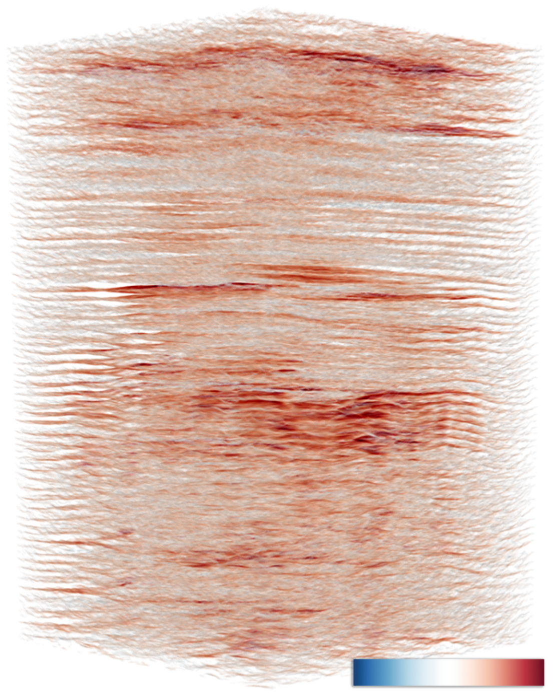

(d) $p_0 = 1.0$

Figure 5.4: Comparison of renderings with different settings for the parameter p_0 (Compare Equation 3.15). The shader was set up to highlight maxima, the same transfer function (without any transparency) was used for all renderings. All transparency is introduced by the cost based modulation.

Neighborhood Size	Base (Phong)	Horizon Enhancing	% of Base
3 ($k = 1$)	28fps	28fps	100%
5 ($k = 2$)	28fps	25fps	89%
7 ($k = 3$)	28fps	21fps	75%

Table 5.1: Performance for cost function-based, horizon enhancing rendering compared to Phong shading (*Base*). See Section 3.2.3 for measurement setup.

cost-modulated shading methods, as the modulation usually results in much more transparent images.

Prototyping the Cost Function

In addition to simply highlighting horizon structures in seismic reflection data the approach can also be used to locally show the results of changing the cost function parameter p_0. Therefore we allow the evaluation of the complete snappiness term (Equation 3.15) per voxel during raycasting instead of only the waveform term from Equation 3.12. Areas of low cost, corresponding to the horizon structures, are rendered opaque, while areas of high cost will be rendered transparently, allowing an approximation of the surfaces the optimization would extract. Even though this technique ultimately cannot replace the additional global optimization for extracting the horizons, it can give a good idea of how the global optimization will behave.

5.2 Exploded Views

Occlusion is a common problem when visualizing three-dimensional objects. Opacity adjustments are commonly used to reveal hidden structures in volume visualization. However, for very dense data, such as seismic data, this is often not

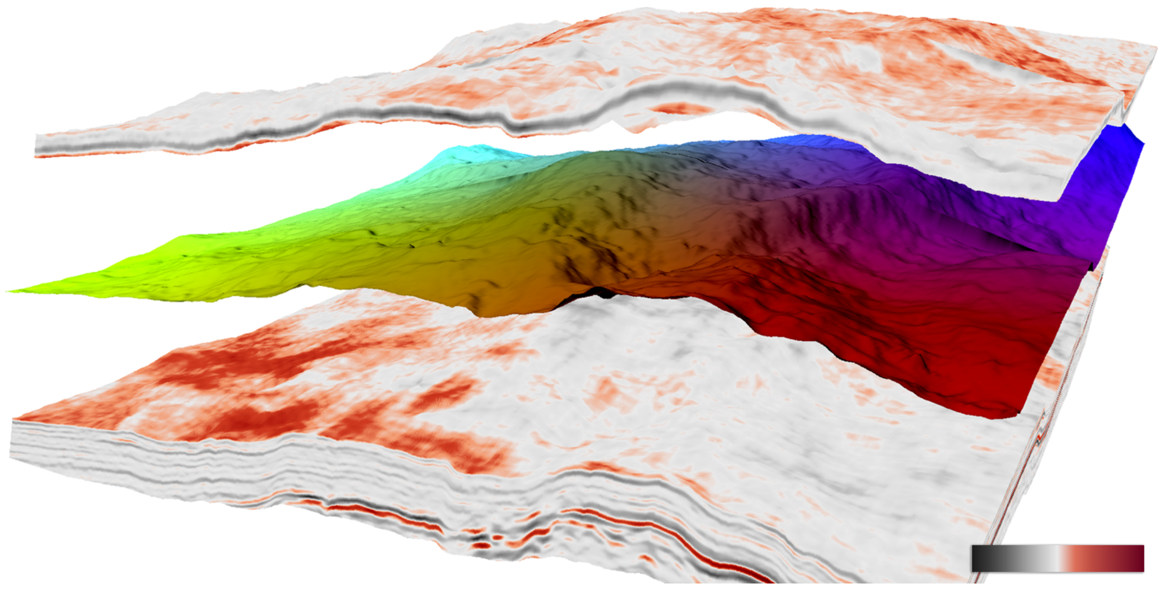

Figure 5.5: Rendering of a seismic cube with two interpreted horizons. The volume is clipped along the upper horizon, the second horizon is used to cut open the volume for the exploded view. The colormap for the surface geometry indicates the position in 3D.

sufficient. Cutaways or clipping can solve this problem, but at the cost of losing contextual information. Illustrators often employ exploded views to reveal hidden structures while retaining context information. An exploded view is basically created by cutting the data into several parts, which are then shown at displaced locations in order to reveal the structures of interest. Figur 5.5 shows an example for a combination of clipping and exploded views.

The general approach to exploded views [13, 62, 95] for volume rendering is setting up the bounding geometry around each part of the volume, rendering each of the parts separately, and then compositing the results. These techniques make very flexible exploded views possible, allowing translation and rotation of arbitrary cut planes along/around arbitrary axes. However, the same constraints of our application scenario, already described in Section 3.2.2, make much of this flexibility unnecessary. We use the seismic horizons as the cut geometry, and then for the explosion itself compute layers of piecewise translations along the z-axis.

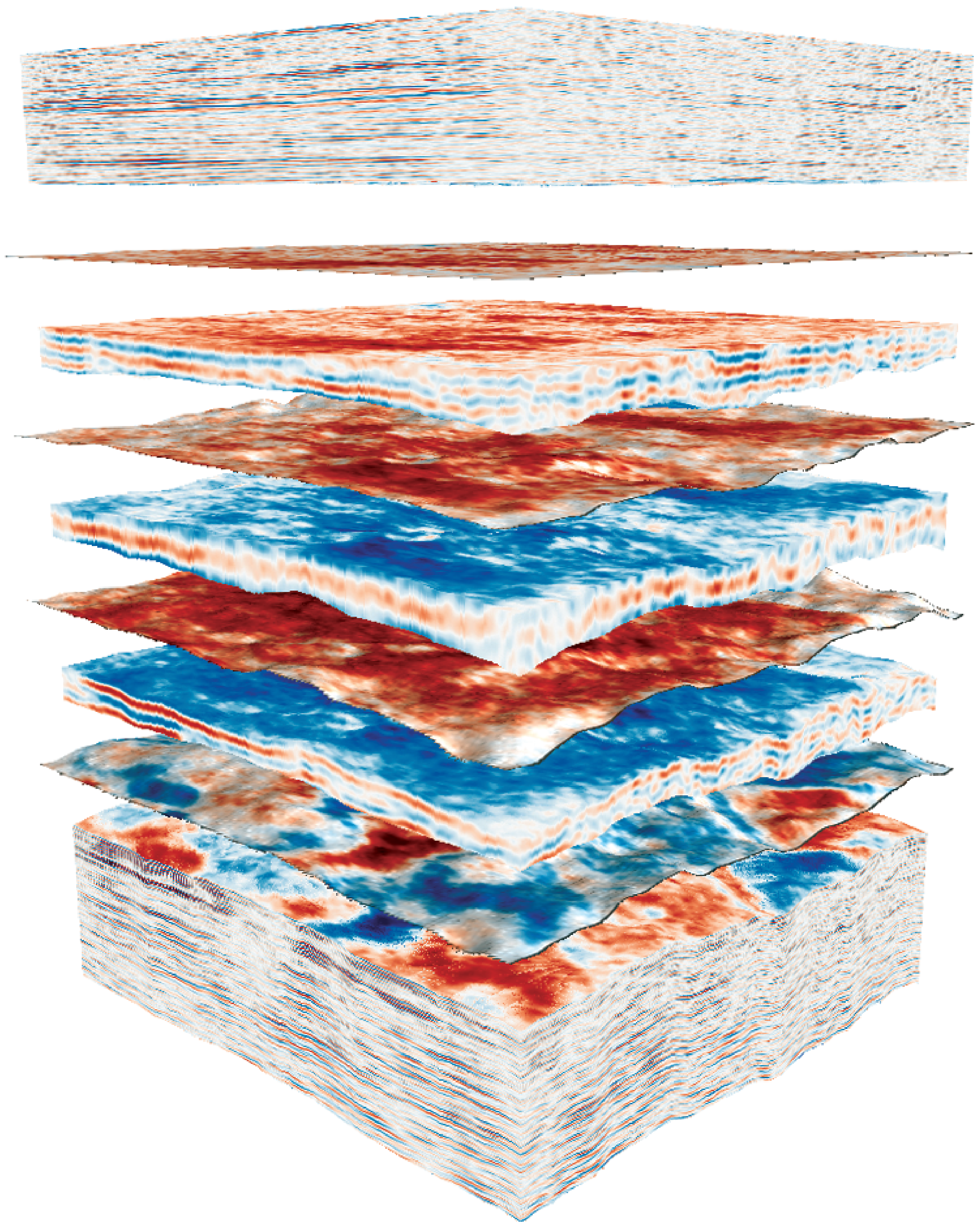

Figure 5.6: Rendering of a dataset with heavily compressed top and bottom layers, using exploded views in combination with standard direct volume rendering.

This is sufficient to enable unobstructed views onto the surfaces. Figure 5.6 shows a rendering of a partially interpreted seismic dataset with a combination of the volume deformation presented in Section 3.2.2 and exploded views. The exploded views allow inspection of the extracted horizon surfaces in context of the seismic data.

Integration into the Rendering Pipeline

Our exploded views approach integrates seamlessly into our framework for the on the fly volume deformation for live depth conversion (Section 3.2.2). The data already available for the deformed rendering makes it possible to deploy exploded views, using the z-axis for translation, and the horizons as cut surfaces. We use a single-pass ray casting approach without any additional setup besides a modified scale factor. Again, we set up a virtual volume with a modified size for the z-axis. To comply with the spacing between the different layers, here the combined spacing for all horizons is added to the scale factor for the volume's z-axis. Adding the spacing to the scale factor for the depth conversion allows us to combine the exploded views with the depth conversion.

Fragment Shader

The fragment shader for rendering the exploded view is only a slight modification of the shader described in Section 3.2.2. We interpret the spacing as empty space preceding each horizon. Thus, the offset to get to the deformed layer is not a direct look-up in the deformed boundaries texture, but the spacing corresponding to all preceding horizons has to be added. Assuming a uniform spacing, this is simply the number of preceding layers, multiplied with the spacing. To check whether the sample position is inside the spacing or in the volume, the deformed boundary

Dataset		Number of Surfaces	Base	Expl. Views	% of DC	% of Base
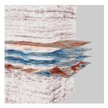	$240 \times 240 \times 1509$	3	117fps	68fps	69%	58%
		5		46fps	53%	39%
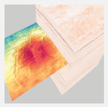	$1422 \times 667 \times 1024$	3	101fps	50fps	62%	50%
		5		27fps	35%	27%

Table 5.2: Performance comparison of the exploded views. We used standard ray casting without illumination for the comparison. % of DC compares to rendering with on the fly depth conversion as shown in Table 3.3.

value of the bottom boundary of the current layer has to be fetched. If the current sample position is larger than the size of the spacing subtracted from the deformed boundary value, the sample is inside the spacing. If that is the case, we can set the current sample's alpha value to zero and proceed with the next sample.

Performance

Performance for the single-pass ray casting with exploded views can be seen in Table 3.3. Compared to the depth-conversion shader, there is virtually no difference in computational complexity (the texture fetch, described above, to decide whether the sample is inside the spacing area can be cached when computing the current layer). However, we currently do not employ empty space skipping in the explosion spacing, which results in a performance loss.

Chapter 6

Visual Analysis of Uncertainties in Ocean Forecasts

This chapter is based on the paper *Visual Analysis of Uncertainties in Ocean Forecasts for Planning and Operation of Off-Shore Structures* [39].

In this chapter, we introduce a GPU-based interactive visualization system for the exploration and analysis of ensemble heightfield data, with a focus on the specific requirements of ocean forecasts. We propose a novel workflow for planning the placement and operation of off-shore structures needed by the oil and gas industry, based on an efficient GPU pipeline for on-the-fly statistical analysis of the ensemble data. While we focus on the visualization and analysis of ocean forecast data, the presented approach could also be used for the exploration of heightfield ensembles from other areas, such as weather forecasting or climate simulation.

The work presented in this chapter shares a foundation with the parameter space exploration framework presented in Chapter 4. Besides the first two sections, introducing the simulation- and application frameworks (Sections 6.1 and 6.2, respectively) the structure of this chapter is identical to the structure of Chapter 4. Statistical analysis (Section 6.3), ensemble visualization (Section 6.4) and Computation and Visualization Pipeline (Section 6.5) all extend their respective counterparts presented in Chapter 4 with additional functionality specific to the ocean forecast analysis application. Section 6.6 presents the results by means of use case scenarios for planning the placement as well as the operations of off shore rigs.

6.1 Ocean Forecast Simulation

The development of a reliable ocean forecasting system requires models capable of simulating ocean circulation and an efficient assimilation scheme that, given enough observations, provides accurate initial conditions for forecasting. High-resolution three-dimensional general circulation ocean models are necessary to reproduce complex mesoscale dynamics like in the Gulf of Mexico [16] (see Figure 6.1). However, such models cannot provide accurate forecasts of mesoscale variability, such as eddy shedding events, without data assimilation. A general circulation ocean model is subject to several sources of uncertainties, not only

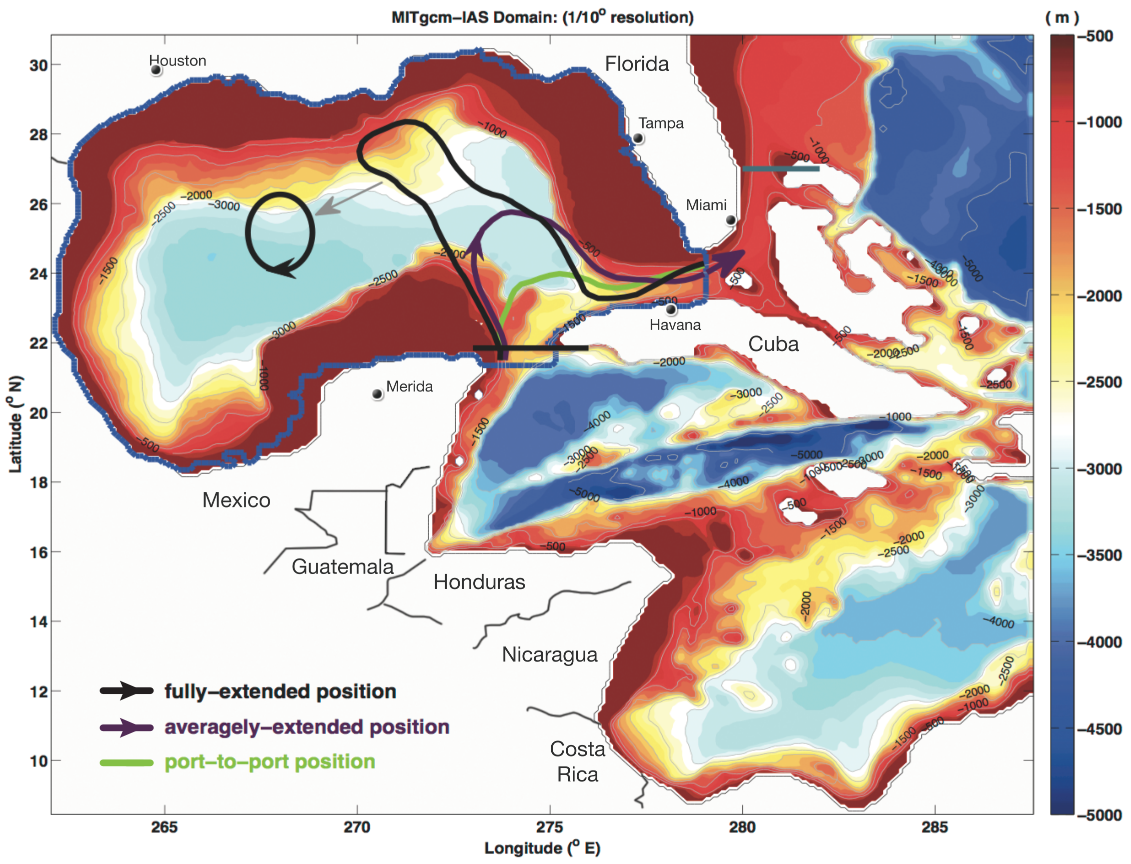

Figure 6.1: The Gulf of Mexico simulation area covered by the presented dataset. The colors denote water depth in meters. The spatial domain enclosed by the thick blue line in the Gulf of Mexico represents the area over which loop current indices were computed [40].

from the poorly known inputs such as the initial state, and atmospheric and lateral boundary conditions, but also from the use of approximate parameterization schemes of sub-grid physics and ocean mixing dynamics. The rapid growth of nonlinear instabilities in the loop current shedding events amplifies these uncertainties in time, which strongly limits the predictability of the system. Data assimilation methods address this issue by constraining model outputs with incoming data. This helps keeping the model evolution on a realistic trajectory and provides optimal initial states for initializing forecast runs, taking into account the model outputs, the available observations, and their respective uncertainties.

Data assimilation was historically cast as a weighted least-squares problem, in which an estimate of the ocean state at a given time is computed by optimizing a cost function measuring a weighted misfit between the model state and available observations, and constrained by some prior information [111]. The prior term, generally taken as a model forecast, is used as a regularization term as the ocean state estimation problem is underdetermined by design, due to the limited amount of available observations. A forecast is then obtained by integrating the estimated state forward in time with a general circulation ocean model. The "optimality" of an ocean state estimate determined by such an approach strongly depends on the prescribed weights, and also on the accuracy of the prior which is subject to the model uncertainties. This means that the estimate, and therefore the forecast, is subject to uncertainties, and these need to be also computed and analyzed as part of the forecasting step. The important role of uncertainties is now increasingly recognized in the ocean prediction community, and also in other communities as the weather prediction community, for proper decision making and efficient risk management.

New assimilation methods based on Bayesian filtering theory have been recently developed by the ocean and atmospheric communities for efficient propagation and quantification of uncertainties [2, 23, 40, 41, 82]. These methods, known as ensemble Kalman filter methods, follow a Monte Carlo approach to represent the uncertainties on a state estimate by an ensemble of model states. These are then integrated forward in time with the general circulation ocean model to quantify uncertainties in the forecast. The estimated forecast uncertainties are then combined with the observation uncertainties to assimilate the new incoming data using a Kalman filter correction step [23], before a new forecast cycle begins. Developing and implementing efficient ensemble Kalman filters with state-of-the-art ocean and atmospheric models is a very active area of research.

With the fast-growing high performance computing resources, the implementation of ensemble Kalman filters with large ensemble members is now practically feasible using highly sophisticated general circulation ocean models. When a filter's ensemble is available, it is customary to calculate various statistical measures of the ensemble spread as indicators of the uncertainties and of their evolution in space and time, which are then used in decision making.

Recently, Hoteit et al. [40] developed an ensemble forecasting system for the Gulf of Mexico circulation based on the Massachusetts Institute of Technology General Circulation Model (MITgcm) [60], and the Data Assimilation Research Testbed (DART) [2]. This system is capable of assimilating various sets of satellite and in-situ ocean observations. We use this system as a real-world scenario that illustrates the new capabilities for analysis and exploration provided by our visualization approach. Figure 6.1 gives an overview of the area covered by the forecasting system.

6.2 Application Framework

Our system targets the interpretation of forecasts from the planning phase of an off-shore structure to its operation. Since the different phases have different requirements, we provide a set of four main views, which are used in different combinations depending on the application scenario. Figure 6.2 shows our application with the main views plus a unified settings panel. The views are two spatial views showing the surface data themselves, one in 3D ⓐ, the other one in 2D ⓑ, a linked histogram view ⓒ as well as a time-series view ⓓ.

While the accessibility of an existing reservoir is the key factor when planning an oil platform, ocean forecasts can provide valuable additional information. Modern drilling techniques to some extent allow flexible paths and thus considerable flexibility for the actual placement of a platform. However, the complexity of the path has implications on the cost of drilling. On the other hand, slight changes of the position might move a platform from an area that is strongly affected by eddy

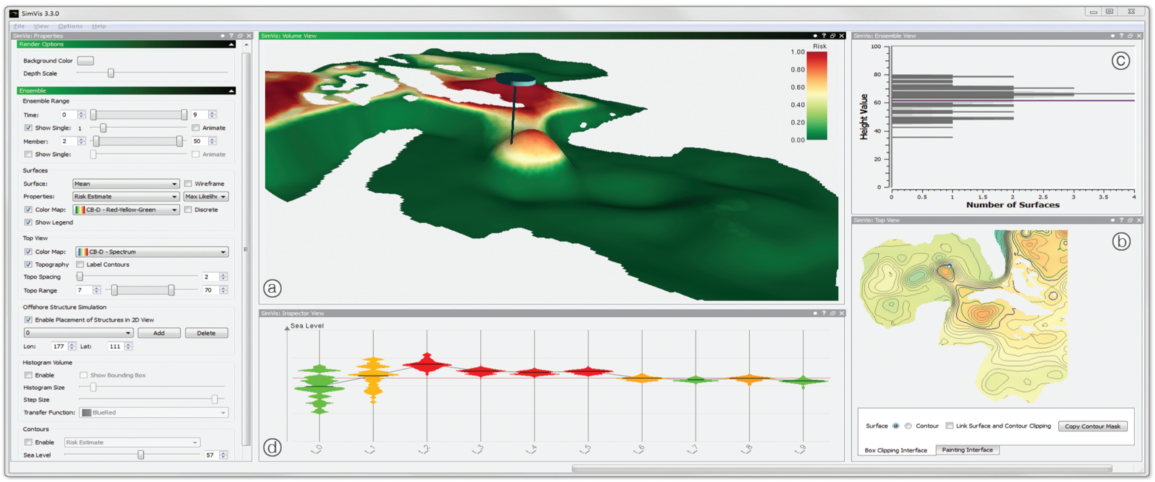

Render Options
Background Color
Depth Scale
Ensemble
Ensemble Range
Time: 0 9
☑ Show Single: 1 ☐ Animate
Member: 2 50
☐ Show Single: ☐ Animate
Surfaces
Surface: Mean ☐ Wireframe
Properties: Risk Estimate Max Likelih
☑ Color Map: CB-D - Red-Yellow-Green ☐ Discrete
☑ Show Legend
Top View
☑ Color Map: CB-D - Spectrum
☑ Topography ☐ Label Contours
Topo Spacing 2
Topo Range 7 70
Offshore Structure Simulation
☑ Enable Placement of Structures in 2D View
0 Add Delete
Lon: 177 Lat: 111
Histogram Volume
☐ Enable ☐ Show Bounding Box
Histogram Size
Step Size
Transfer Function: BlueRed
Contours
☐ Enable Risk Estimate
Sea Level 57
Surface ● ○ Contour ☐ Link Surface and Contour Clipping Copy Contour Mask
Box Clipping Interface Painting Interface

Figure 6.2: Our application for exploration of ocean forecast ensembles consists of four main views. The simulated ocean surface, or a derived version, like the mean surface for a time step, can be shown in 3D or 2D (ⓐ and ⓑ). The histogram view (ⓒ) shows the complete distribution of the ensemble at a selected position, while the time-series view (ⓓ) shows the distribution and the resulting operational risk at a selected position for multiple time steps.

shedding, which leads to long downtimes, to a less affected area, overall resulting in more efficient operations.

6.3 Statistical Analysis

The input to our framework is an ensemble of heightfields representing the sea surface height. The data is very similar to the horizon ensembles we extract and analyze in Chapter 4. Therefore we use the same statistics computations presented in Section 4.2 as the basis for our ocean forecast analysis framework and extend it by some details, specific to the planning of off-shore structures. The main difference to the framework presented above is the parameter-space exploration. Instead of mapping parameters for a cost function, in this case we have different starting conditions and different models for the simulation. In addition, we map time to one of the parameters. While in the standard setting the statistics are only computed for one time-step at a time, it would also be possible to compute the statistics over any desired timespan. Furthermore, since the distributions of the simulation results are mostly Gaussian, here it makes sense to use the mean surface as the main representative surface instead of the previously introduced maximum likelihood surface. The two main additions to the statistics are a discrete probability density function (pdf) volume for the ensemble distribution, derived from the histogram volume, as well as a risk estimate, defining a risk value for each position with respect to a predefined critical sea surface level.

Probability Density Function

We compute a discrete pdf for each (x, y)-position by applying a kernel density estimate to the 1D histograms at each position. Just like for the histograms, we combine the set of one dimensional pdfs to a 3D volume, which can be rendered alongside the representative surface to give an overview of the complete distribution of the ensemble.

Risk Estimate

We define and visualize a simple risk estimate as the percentage of ensemble members above the defined critical height. This value is computed for every (x, y)-position for every time step. The surface in Figure 6.2ⓐ, as well as the glyphs in Figure 6.2ⓓ are color-mapped with such a risk estimate. The risk value is not only dependent on the ensemble itself, but also the critical sea level. Therefore the user can interactively modify this value, just like it is possible to constrict the parameter range, and get live updates on the results for the defined value.

6.4 Ensemble Visualization

Similar to the statistical analysis, we base our visualization framework on the techniques developed for the visualization of horizon ensembles, presented in Section 4.3. We added a 2D view for overview, as well as a time-series view to inspect the complete time series for a single position to the existing linked 3D and histogram views. Furthermore, we extended the 3D surface rendering technique by the possibility to blend extracted iso contours onto the surface, as well as a volumetric cursor to locally show the distribution of the ensemble directly in the 3D view.

3D View

The 3D view provides a spatial overview of the data. Using the same techniques for surface rendering as described in Section 4.3, we allow rendering the representative for the sea surface, usually the mean of the ensemble, in 3D. In addition to

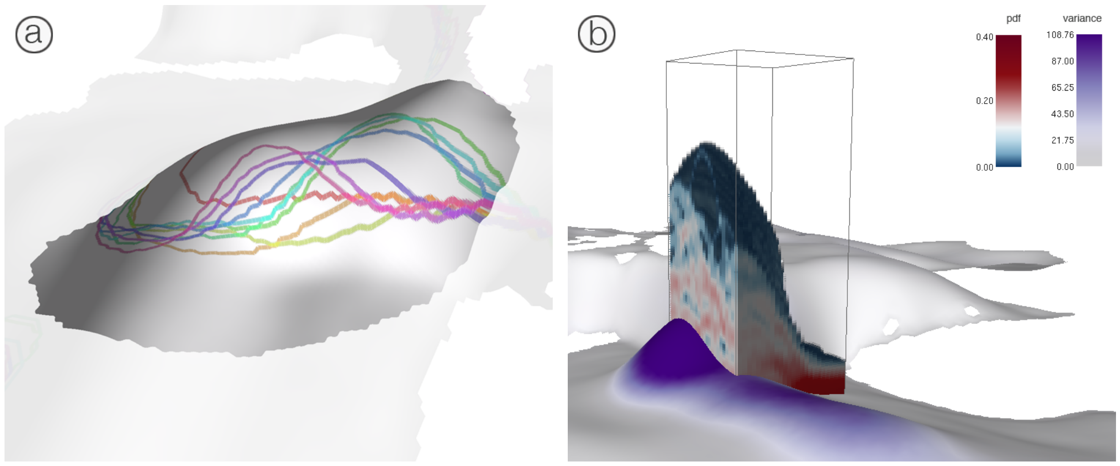

Figure 6.3: 3D View Detail. ⓐ shows iso contours of the mean surfaces for all time steps blended over the current surface. The area of interest is rendered with full opacity, while the context is preserved by rendering the remaining parts semi-transparently. ⓑ shows a volume rendering of the pdf around a user-selected position. The surface is color-mapped with the variance. The large spread in areas of high variance is clearly visible in the volume rendering.

the statistical properties described above, we can also use the risk estimate (Section 6.3) to color code the surface. To allow visualization of a second property resulting from the statistical analysis, or information from several time steps at once, we also added the extraction of iso contours from any of the scalar fields derived from the ensemble. Figure 6.3ⓐ shows an example, where iso contours corresponding to the critical sea level were extracted from the mean surfaces for all time steps and overlaid on the texture.

An additional benefit of the 3D view is that it is possible to use volume rendering for showing details of the distribution of the ensemble. Similar to approaches presented by Pöthkow et al. [87, 88], as well as Pfaffelmoser et al. [80], we depict the actual distribution of the ensemble as a volume around the surface. Instead of using a parametric representation of the data based on mean and variance, we allow rendering the full probability density function (pdf) of the distribution, to allow detailed inspection of the actual data. However, since rendering the complete volume would most likely result in the complete occlusion of the representative surface, we propose to render only a a small subset of the volume, which is of adjustable size. Similar to the linked histogram view, this allows showing details on demand, without occluding the context. The technique essentially works like a volumetric cursor (see Figure 6.3ⓑ). The user can simply probe the data by hovering with the mouse over a position of interest, and the probability density volume is then rendered around the picked position.

Time-Series View

Specifically for planning the operations of a platform at a defined position, we developed the time-series view, shown in Figures 6.2ⓓ and 6.4. This view always shows the complete time-series for a single lateral position. Once defined, or loaded, our application caches several positions of off-shore structures, from which one can be selected using a drop-down menu. The selected position is highlighted by markers in the spatial views. The view shows the ensemble distribution

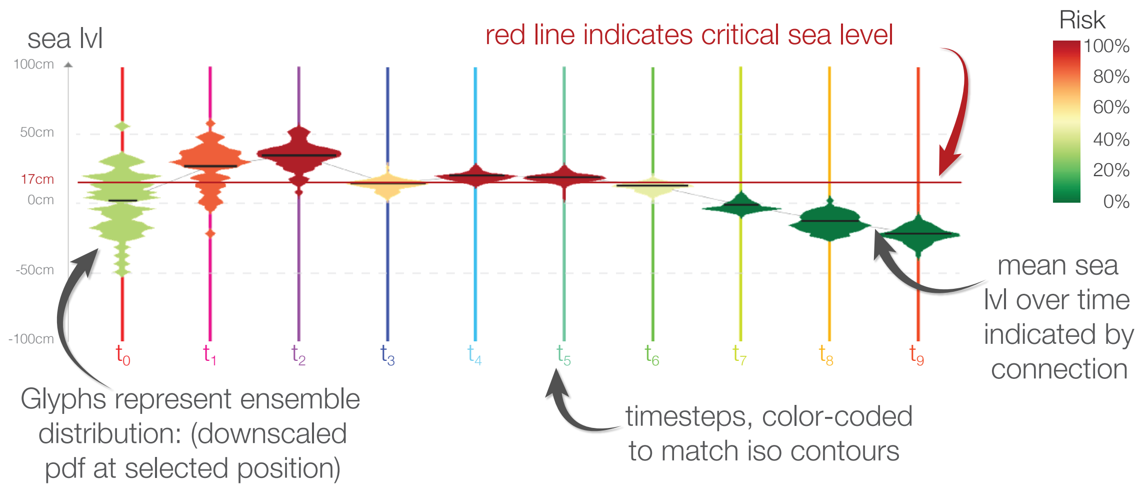

Figure 6.4: The Time-Series View in detail. The y axis corresponds to the sea level, the x axis to time. Each glyph shows the distribution of the selected position for one time step. Glyphs are colored using the associated risk, i.e., the fraction of the distribution above the selected critical sea level.

at the selected position for all time steps side by side using a simple glyph, per time step. To provide spatial context, the plots are arranged on the y-axis at their original depth positions and as such can be compared directly to each other, but also to the predefined critical sea level, which is indicated by a horizontal line. The glyphs show the complete ensemble distribution at the selected position. Figure 6.5 shows a detailed explanation of the glyph. The glyph is based on the design of violin plots [34]. We use the probability density function (pdf) for the outline of the glyph and indicate the mean value by a horizontal line at the appropriate position. To help identify the critical time steps, the glyphs are color-coded according to the risk estimate. The risk can easily be estimated by looking at the fraction of the glyph that is above the critical sea level. The uncertainty is also encoded in the glyph. A wide distribution of values, indicating a large degree of uncertainty, results in a scattered pdf and thus in a very long glyph. A certain result will exhibit a strong clustering of surface values and this will result in a very compact glyph

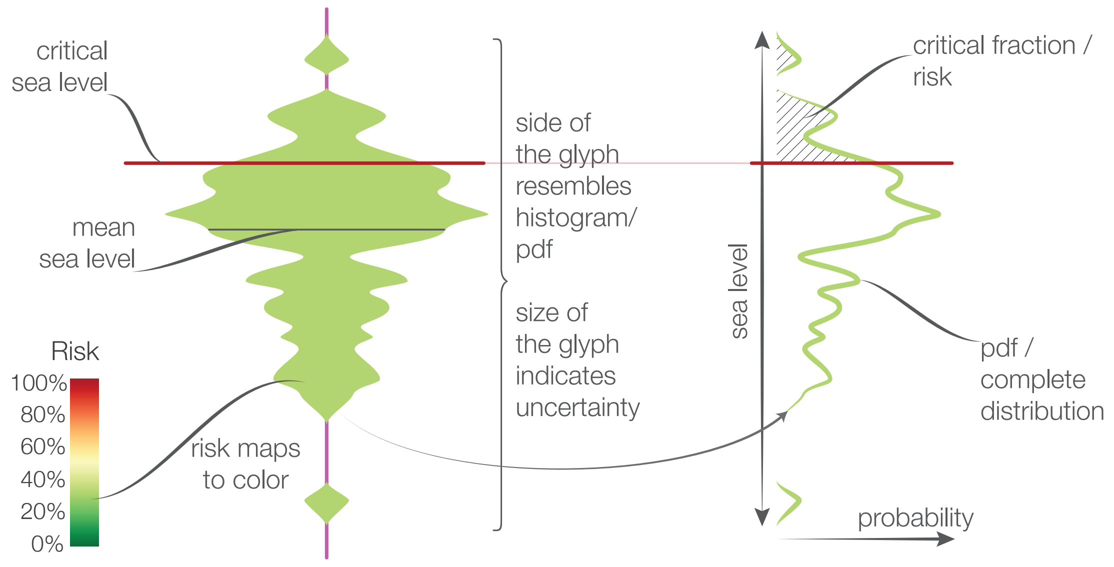

Figure 6.5: The glyph developed for visualizing the ensemble properties at a defined spatial position.

(compare for example time step t_0 and time step t_3 in Figure 6.4). In addition, we can show any of the derived statistical properties by coloring the glyph.

Using the time-series view, domain experts can then easily identify the points in time where operations should be halted. Without ensemble forecasts, rigs were operated based on a single simulation. However, even when ensemble forecasts are available, a visual exploration approach is necessary. Without our visualization system, our domain experts would define the safeness by simply looking at the mean and variance values of the ensemble. In each time step, we indicate the mean value of the distribution by a bold black bar, providing the same information as before, for all time steps in a single view. The user can immediately identify critical time steps, looking at the color and position of each glyph, and possibly order an unavoidable shutdown of operations. If the situation is unclear, the glyph provides the complete distribution to enable the expert to make a decision.

6.5 Computation and Visualization Pipeline

As described before, the ocean forecast visualization framework presented in this chapter and the horizon ensemble framework presented in Chapter 4 share

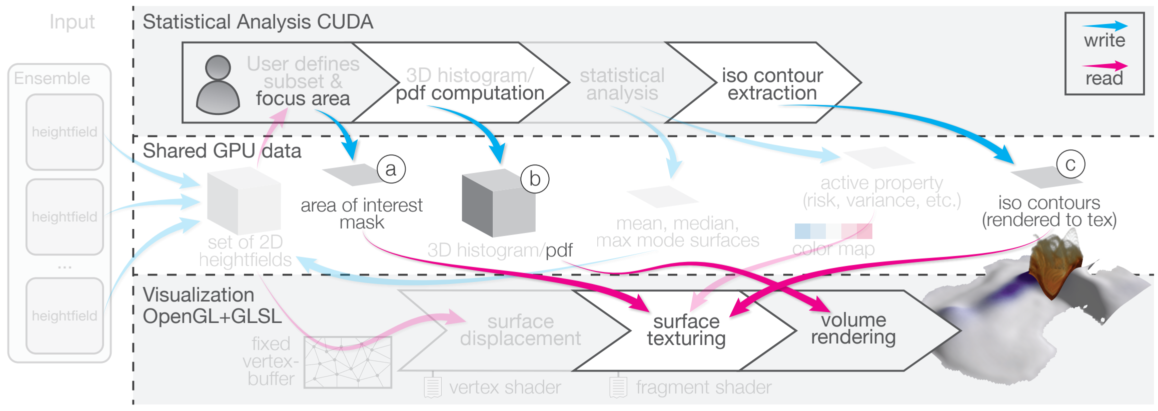

Figure 6.6: The extensions to the computation and rendering pipeline presented in Section 4.4.

large parts of the analysis and visualization pipeline. The additions specific to the pipeline used for the ocean forecasting are highlighted in Figure 6.6. Besides the addition of a risk estimate, described in Section 6.3, which integrates into the statistical analysis part of the pipeline, we added three major features to ease the planning of off-shore structures. We allow defining a focus area, which is highlighted in the spatial views (Figure 6.6ⓐ), we added the pdf (Figure 6.6ⓑ) which can be rendered as a volume on top of the representative surface to show the complete distribution of the ensemble, and finally we added the extraction of iso contours (Figure 6.6ⓒ) from all 2D scalar fields (statistical properties as well as surfaces) to allow the inspection of multiple properties as well as multiple times teps at once.

Area of Interest Definition

The focus area, or area of interest, can be defined by painting directly on the surfaces in the 2D view (Figure 6.2ⓑ). In the pipeline, the painted area is rendered into a texture, which is used as a mask during rendering. The focus area is then rendered with full opacity, while the context is rendered translucently (Compare Figure 6.3ⓐ).

Probability Density Volume

The pdf volume is derived from the 3D histogram when needed by applying a kernel density estimate for each of the 1D histograms. It is stored as an additional 3D texture in GPU memory, allowing it to be rendered directly using standard ray casting on top of the surface geometry similar to the seismic cube in the horizon extraction application. However, here we render the volume only on demand and only a small part of the complete volume. We use the same technique as described under *Detailed Inspection* in Section 4.4 to pick the position of the mouse cursor on the surface. The geometry for ray casting into the pdf is then set up as a small cube, centered around the picked position and with user adjustable size.

Iso Contouring

We have implemented marching squares using CUDA, based on the marching cubes example from the CUDA SDK, as well as a CPU version. The result of the iso contour extraction is a set of edges forming the contours. We keep the initial geometric representation of the contours, for example for use in the 2D view, but for overlaying the contours onto the 3D surfaces we render the contours into an offscreen buffer, which is then used for texturing. Just like the rest of the analysis pipeline, the iso contour extraction happens interactively, allowing adjustments of the parameter range, as well as the iso value with instant feedback.

6.5.1 Performance

The performance of the statistical analysis is crucial for interactive exploration of the parameter space. We used the dataset of the Gulf of Mexico, computed by the simulation system described above, for measuring the performance of the statistics computation. The dataset consists of a total of 500 surfaces spread over ten time steps. The spatial resolution is 275×325, resulting in $89,375$ data points per surface. Since usually one time step is investigated at a time, we show performance for a single time step, consisting of 50 surfaces, as well as the complete dataset. Table 6.1 shows the resulting computation times for a single time step.

The computations were performed using an NVIDIA GeForce GTX 580 with 1.5GB of graphics memory. The timings were averaged over 1000 kernel executions. As all data stays on the GPU, no bus transfer has to be considered. For comparison, we also show computation times of a single time step on the CPU. The computations were carried out on a workstation with two six-core Xeons (12 physical cores plus hyper threading) clocked at 3.33GHz and 48GB of main memory. The CPU computations were parallelized using OpenMP, utilizing 24 threads.

		CUDA		CPU		Speedup	
	Property	w/o	w dep	w/o	w dep	w/o	w dep
1	Histogram	3.23	3.23	19.24	19.24	6.0x	6.0x
2	PDF^{1}	12.93	16.16	45.70	64.94	3.5x	4.0x
3	Range	0.71	0.71	3.45	3.45	4.9x	4.9x
4	Mean	0.71	0.71	3.48	3.48	4.9x	4.9x
5	Median^{1}	0.70	3.93	8.78	28.02	12.5x	7.1x
6	Mode^{1}	1.40	4.63	4.65	23.89	3.3x	5.2x
7	Variance^{4}	0.72	1.43	3.85	7.33	5.3x	5.1x
8	Std Dev^{4,7}	0.02	1.45	0.14	7.47	7.0x	5.2x
9	Skewness^{1,4,6,7,8}	0.05	6.13	0.16	31.42	3.2x	5.1x
10	Kurtosis^{4,7}	0.74	2.17	4.05	11.38	5.5x	5.2x
11	Risk	1.70	1.70	27.93	27.93	16.4x	16.4x
12	Iso Contour$^{\text{any of } 3-11}$	5.20	n/a*	1.40	n/a*	0.27x	n/a*

*Computation time with dependencies varies, depending on the property used for iso contouring.

Table 6.1: Comparison of computation times between GPU (CUDA) and CPU. All times are in milliseconds. The first column shows ID and name of the property, the supercripts indicate the IDs of the properties that are required to compute the corresponding property. The columns titled *w/o* and *w dep* show the computation times for just this property assuming all dependencies are already cached and the computation time including all dependencies, respectively. We note that computing the dependencies is only needed once, after changing the parameter range. The last two columns show the speedup from CPU to GPU.

Compared to the CPU version, we achieved a speedup of roughly $5\times$ for all tasks when considering the dependencies with our GPU based pipeline.

Table 6.2 shows how computation times scale with larger data. We compare the standard case of a single time step with the complete ensemble consisting of 500 surfaces. In general, it can be seen that using the GPU even for 500 surfaces, the slowest update including skewness and all dependencies plus the probability

		50 Surfaces		500 Surfaces	
	Property	w/o	w dep	w/o	w dep
1	Histogram	3.23	3.23	38.56	38.56
2	PDF^{1}	12.93	16.16	12.78	51.34
3	Range	0.71	0.71	11.09	11.09
4	Mean	0.71	0.71	10.89	10.89
5	Median^{1}	0.70	3.93	0.70	39.26
6	Mode^{1}	1.40	4.63	1.41	39.97
7	Variance^{4}	0.72	1.43	10.87	21.76
8	Std Dev^{4,7}	0.02	1.45	0.02	32.78
9	Skewness^{1,4,6,7,8}	0.05	6.13	0.05	72.80
10	Kurtosis^{4,7}	0.74	2.17	10.76	32.52
11	Risk	1.70	1.70	21.00	21.00
12	Iso Contour$^{\text{any of } 3-11}$	5.20	n/a*	23.90	n/a*

*Computation time with dependencies varies, depending on the property used for iso contouring.

Table 6.2: Computation times for 50 and 500 surfaces. All times are in milliseconds. The first column shows ID and name of the property, the supercripts indicate the IDs of the properties that are required to compute the corresponding property. The columns titled *w/o* and *w dep* show the computation times for just this property assuming all dependencies are already cached and the computation time including all dependencies, respectively.

density function (which needs to be computed for the histogram and time series views) still allows for interactive update rates.

The histogram, range, mean, variance, kurtosis and the risk estimate are calculated directly from the ensemble and as such the complexity relies solely on the number of surfaces and valid data points per surface. We would expect the computation time for these values to scale linearly with the number of surfaces/-valid data points, which seems to be in line with the measured numbers. For even larger datasets, however, it would make sense to compute range, mean, variance, kurtosis and the risk estimate using the histogram. This would result in constant time, only depending on the size of the histogram. For the datasets here, however, the histogram computation is the limiting factor. The probability density function, median and mode are looked up using the histogram, and therefore there is no difference between the small and the large data set. Standard deviation and skewness are implemented as linear combinations of other surface properties, and thus computation times are also independent of the number of surfaces. With the dependencies precomputed, the computation of both properties is trivial, which results in very short computation times.

6.6 Results

The following Sections 6.6.1 and 6.6.2 illustrate workflows for planning placement as well as operations of off-shore structures using a real-world Gulf of Mexico ocean forecast dataset. The dataset covers the Gulf of Mexico basin between $8.5°$ N and $31°$ N, and $262°$ E and $287.5°$ E on a $1/10° \times 1/10°$ grid with 40 vertical layers. Forecasting experiments were performed over a six-month period in 1999 between May and October during which a strong loop current event occurred (Eddy "Juggernaut") [70]. The resulting dataset consists of ten time steps, each consisting of

50 ensemble members. The lateral dimensions are represented by a grid consisting of 275×325 samples.

6.6.1 Placement Planning

Planning the placement of an off-shore structure demands a complete overview of the ensemble in the spatial domain, but also over all available time steps. Figure 6.7 outlines all necessary steps. First, the user defines the area of interest (defined by factors not available in the ocean forecast, like reservoir reachability) in the 2D view (Figure 6.7a) either by a simple bounding rectangle, or completely free by painting directly on the map. In Figure 6.7b, the sea level of the mean surface for a single time step is mapped to the third dimension. The standard deviation is used for pseudo-coloring in the 3D view. By animating all time steps, the user can now get an overview of the mean sea level at the selected area of interest, as well as the corresponding uncertainties. Besides the 3D view, animation can also be used in the 2D view, showing the sea level using iso contours and pseudo-coloring (inset). While the animation is very effective to give a first impression of the changing sea level, it is challenging to derive qualitative results. Therefore, in the next step, the user can look at iso contours from the mean surfaces, or risk estimates of multiple time steps in a single view. The contour for a single selected sea level and maximum allowed risk is extracted for all time steps and rendered on the mean surface. The selected sea level, as well as the maximum risk, can be changed on the fly (compare the animation in Figure 6.7c). Starting with a low sea level and zero risk, the user can gradually approach a suitable compromise of available positions, critical sea surface height and resulting risk, to narrow down the area of interest to a few points. Once a compromise is found, the ensemble distribution can be probed interactively at the interesting positions, to verify the

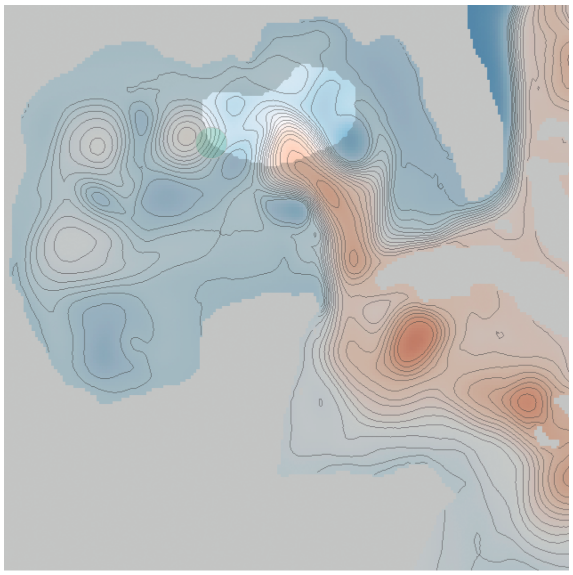

(a) Area of Interest Definition.

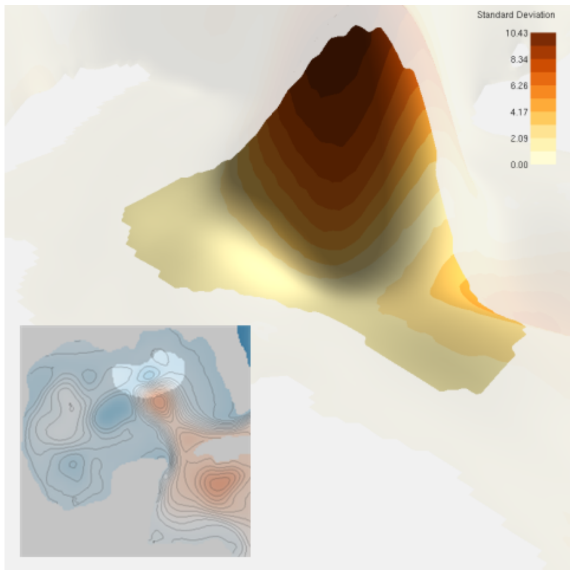

(b) Sea Level and Std. Deviation.

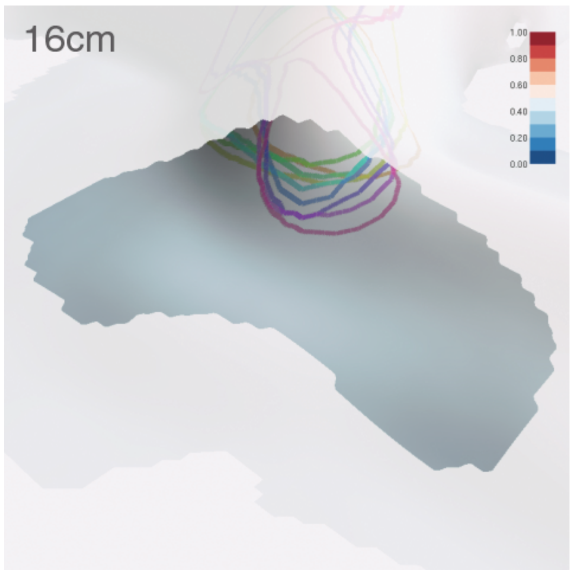

(c) Time Series Sea Level Contours.

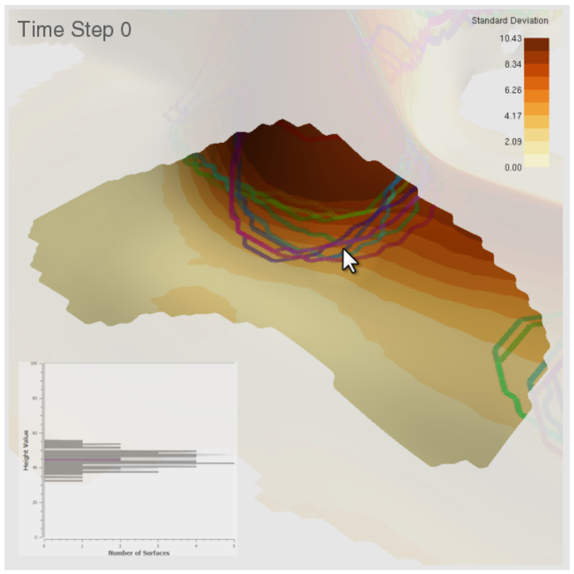

(d) Distribution Detail.

Figure 6.7: Spatial Exploration for placement planning consists of four main steps: Definition of the area of interest based for example on reservoir reachability (a), general overview (b), time series analysis (c) and detailed analysis for verification (d).

results (Figure 6.7d). At this point, the potential placement is narrowed down to a few positions. A detailed analysis of all time steps, identical to the analysis for operations (Section 6.6.2) can be performed.

6.6.2 Final Placement / Operational Phase

Most of the ensemble analysis for planning operations and unavoidable downtimes is carried out in the time-series view shown in Figure 6.8. After definition of a set of positions corresponding to the managed rigs, one position can be selected at a time from a drop-down box. This location is then depicted in the 2D and 3D views for spatial context. The critical sea level, as well as the acceptable risk, can be defined from the user interface. We provide a set of standard color maps for coloring the glyphs. The color map is also freely customizable, most importantly to adapt to the acceptable risk. A good color map should highlight three cases based on the risk estimate: Time steps which are safe for operation with a high certainty, time steps where the rig needs to be shut down with large certainty, and finally uncertain time steps.

In the final phase of planning the placement, when positioning is narrowed down to a few potential positions, the time-series view can be used to compare these positions. Figure 6.8 shows a comparison for two close positions. While Figure 6.8ⓐ indicates a position which would allow minimal downtimes (actually none of the time steps exhibits any risk) the position in Figure 6.8ⓑ, which is very close in space, exhibits a very different result. The sea level will certainly be above the critical level for six of the ten time steps. In addition even the first two time steps, which overall are less risky, expose a large amount of uncertainty. Using this

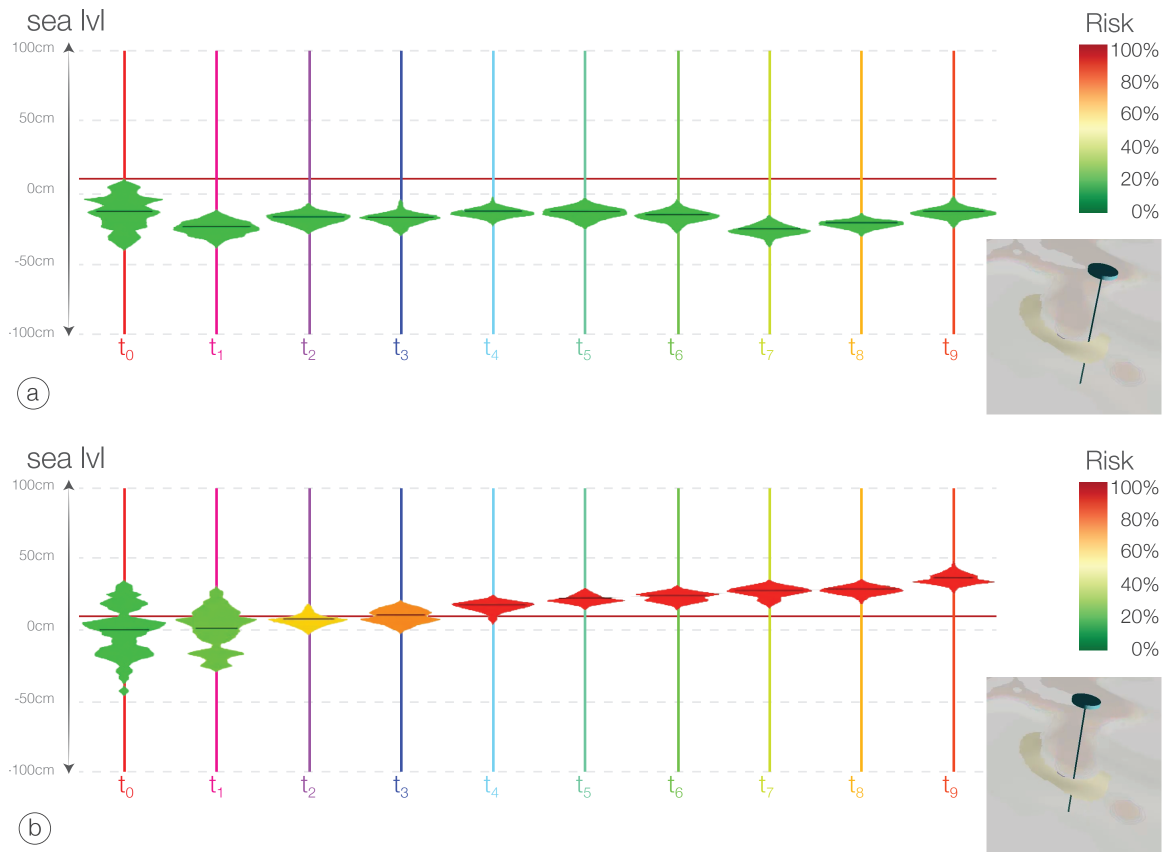

Figure 6.8: Comparison of the time series for two very close positions (indicated by the markers in the insets). ⓐ shows a position which does not exhibit any risk at all over the complete time series. Moving the position slightly results in several time steps which would definitely require a shutdown of operations ⓑ.

comparison one can immediately see that the position in ⓐ will allow much more efficient operations.

The actual operation planning is a recurring process with only a few future time steps available at a time. The parameters like position, critical sea level, acceptable risk and the corresponding color map, however, typically do not change. Hence all these settings can be loaded from a state file alongside new forecast data. Assuming a color map as described, after loading the data the user can immediately identify safe and unsafe time steps from the color of the corresponding glyphs. Only uncertain time steps need further investigation. The main factor to consider for these cases is the spread or uncertainty of the distribution. A compact glyph corresponds to a distribution with little uncertainty. Here, the risk estimate can immediately be used for making a decision to shut down the rig. A large glyph in general indicates large uncertainty. Here, the user must carefully weigh several properties: Are ensemble members in the critical range close to the critical sea level or far above, is the distribution skewed to either side, etc. While in general this information can be derived from the glyph, the user can also access the raw results from the statistical analysis at this point, before making a final decision.

6.7 Conclusion

In this chapter, we have presented an interactive system for the visualization, exploration and analysis of ocean forecasts in the form of heightfield ensemble data. The core of our framework, which consists of statistical analysis and rendering, is implemented in an efficient GPU-based pipeline. We show the utility of our framework for ocean forecasting in a case study based on real world forecast data of the Gulf of Mexico.

Chapter 7

Summary and Discussion

This thesis presents several visual, interactive techniques, to enhance workflows for oil and gas exploration. We introduce novel applications for the creation of subsurface models and the visual analysis of ocean forecasts. Both applications help to plan safe and efficient operations for oil and gas exploration.

Our application for subsurface modeling, for the first time, allows the integration of well data, recorded in spatial depth, into the seismic interpretation workflows, based on seismic reflection tomography data, recorded in time. Our novel joint/time depth domain workflow is made possible by an on the fly depth conversion technique. Additionally, rather than axis aligned, we set up slice views based on well positions, to maximize the availability of the information gathered from wells. We introduce an interactive global optimization technique for horizon extraction. Based on the horizon extraction technique we introduce ensemble computation to seismic interpretation, by automatically sampling the parameter space of the cost function, underlying the global optimization. Based on these ensembles, we present a framework for efficient exploration of the parameter space of the cost function. Finally we introduce a novel shading technique, based on the local waveform of seismic traces, to highlight horizon structures without preprocessing and present the application of exploded views for the visualization of seismic data.

The second application, presented in this thesis allows planning the placement and operations of off-shore structures, like oil rigs. We present a framework for the interactive visual analysis of ensemble simulations of the sea surface. The framework is based on an efficient, completely GPU-based framework, for statistical analysis and visualization of ensembles of surfaces. We present a case study, based on simulation data of the Gulf of Mexico, that shows the application of our framework in a real world scenario.

Limitations and Open Questions

The presented subsurface modeling application focuses on the extraction of seismic horizons only. A complete subsurface model includes additional structures, most importantly faults. Faults are areas where the rock slipped (Compare Figure 7.1), creating discontinuities in the subsurface layers. The integration of faults into our subsurface modeling workflow is left to future work. A possible approach could be integrating a term, describing the likeliness of an edge belonging to a fault, into our cost function, to guide the global optimization along faults. A good fit for such a term could be based on the work of Jeong et al. [42].

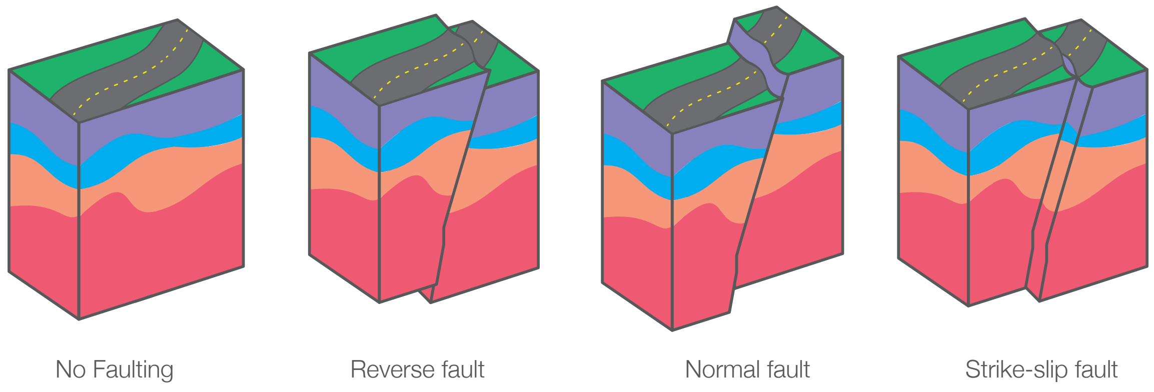

Figure 7.1: Different fault types. Horizons intersected by normal and strike slip faults can still be handled as height fields. Reverse faults would require splitting up the volume. Figure reproduced from the USGS Earthquake Glossary [105].

At first glance, representing the horizons as heightfields seems a major limitation for the inclusion of faults. However, our complete extraction pipeline can handle arbitrary geometry. Only after extracting the optimal surface from the graph, as described in Section 3.4.4, we convert it to a heightfield for efficient rendering. Additionally, as can be seen in Figure 7.1, only reverse faulting creates layers whose boundaries can not be represented as heightfields, the more common normal faults, as well as strike-slip faults result in horizons where no (x, y)-position maps to more than one depth value. The on the fly depth conversion, as presented in Section 3.2.2, does only work for subsurface layers bound by heightfields. However, once faults are extracted, the reverse faults could be used to divide the dataset into subsets, for which the depth conversion would work again.

We also use a property of heightfields for our statistical analysis of ensemble data, presented in Chapters 4 and 6. For both we compute the statistics for each (x, y)-position, knowing that each surface passes through each (x, y)-position exactly once. Such an approach would not work for comparing arbitrary geometry. However, if correspondences between ensemble members are known, these can be used as the basis for the statistics computation. As long as the connectivity of the vertices does not change even our rendering framework, which creates the final geometry on the fly, would still work, by simply using vertex indices to lookup the final position in the ensemble texture, instead of (x, y)-coordinates.

Finally our prism based workflow, presented in Section 3.3 approximates each well position with a single straight line, orthogonal to the surface. Modern drilling techniques allow complicated bore hole paths. When using well logs, we can not handle such paths in our framework, as is. As long as wells do not intersect, and the topology of the object, enclosed by three wells, corresponds to a prism, an approach, where the sides of the 'prism' are deformed for visualization and interaction, would be thinkable. For the use of well tops the trajectory of the bore hole is irrelevant. Since well tops are sparse, discrete samples along the well, we simply treat each top separately. When two or more tops from a single well correspond to separate (x, y)-positions we consider them separately during triangulation. While this results in prisms, where not all corners provide information for all hroizons, none of the well data is lost.

REFERENCES

[1] LEMON library for efficient modeling and optimization in networks. Available online at `http://lemon.cs.elte.hu` (Mar. 08 2013).

[2] J. Anderson, T. Hoar, K. Raeder, H. Liu, N. Collins, R. Torn, and A. Avellano. The data assimilation research testbed: A community facility. *Bulletin of the American Meteorological Society*, 90:1283–1296, 2009.

[3] C. Armstrong, B. Price, and W. A. Barrett. Interactive segmentation of image volumes with live surface. *Computers & Graphics*, 31(2):212–22, 2007.

[4] J. Beyer, M. Hadwiger, T. Möller, and L. Fritz. Smooth mixed-resolution GPU volume rendering. In *Proceedings of IEEE/EG International Symposium on Volume and Point-Based Graphics*, pages 163–170, 2008.

[5] Å. Birkeland, S. Bruckner, A. Brambilla, and I. Viola. Illustrative membrane clipping. *Computer Graphics Forum*, 31(3):905–914, 2012.

[6] J. F. Blinn. Models of light reflection for computer synthesized pictures. In *Proceedings of the 4th Annual Conference on Computer Graphics and Interactive Techniques*, SIGGRAPH '77, pages 192–198, 1977.

[7] A. Blinov and M. Petrou. Reconstruction of 3-d horizons from 3-d seismic datasets. *IEEE Transactions on Geoscience and Remote Sensing*, 43(6):1421–1431, 2005.

[8] H. G. Borgos, O. Gramstad, G. V. Dahl, P. L. Guern, L. Sonneland, and J. F. Rosalba. Extracting horizon patches and geo-bodies from 3d seismic waveform sequences. *SEG Technical Program Expanded Abstracts*, 25(1):1595–1599, 2006.

[9] Y. Boykov and M.-P. Jolly. Interactive organ segmentation using graph cuts. In *MICCAI '00: Proceedings of the Third International Conference on Medical Image Computing and Computer-Assisted Intervention*, pages 147–175, 2000.

[10] Y. Boykov and M.-P. Jolly. Interactive graph cuts for optimal boundary & region segmentation of objects in n-d images. In *Proceedings of IEEE International Conference on Computer Vision, 2001*, pages 105–112 vol.1, 2001.

[11] Y. Boykov, O. Veksler, and R. Zabih. Fast approximate energy minimization via graph cuts. *IEEE Transactions on Pattern Analysis and Machine Intelligence*, 23(11):1222–1239, 2001.

[12] R. A. Brown. Animated visual vibrations as an uncertainty visualisation technique. In *International Conference on Computer Graphics and Interactive Techniques in Australasia and South East Asia*, pages 84–89, 2004.

[13] S. Bruckner and M. E. Gröller. Exploded views for volume data. *IEEE Transactions on Visualization and Computer Graphics*, 12(5):1077–1084, 2006.

[14] L. Castanie, B. Levy, and F. Bosquet. Advances in seismic interpretation using new volume visualization techniques. *First Break Journal*, pages 69–72, 2005.

[15] L. Castanie, B. Levy, and F. Bosquet. VolumeExplorer: Roaming large volumes to couple visualization and data processing for oil and gas exploration. In *Proceedings of IEEE Visualization Conference '05*, pages 247–254, 2005.

[16] E. P. Chassignet, H. E. Hurlburt, O. M. Smedstad, C. N. Barron, D. S. Ko, R. C. Rhodes, J. F. Shriver, A. J. Wallcraft, and R. A. Arnone. Assessment of data assimilative ocean models in the gulf of mexico using ocean color. *Circulation in the Gulf of Mexico: Observations and Models*, 161:87–100, 2005.

[17] L. M. Cherubin, W. Sturges, and E. Chassignet. Deep flow variability in the vicinity of the yucatan straits from a high resolution MICOM simulation. *Journal of Geophysical Research*, 110:20–72, 2005.

[18] F. Counillon and L. Bertino. High-resolution ensemble forecasting for the gulf of mexico eddies and fronts. *Ocean Dynamics*, 59:83–95, 2009.

[19] E. Dijkstra. A note on two problems in connexion with graphs. *Numerische Mathematik*, 1(1):269–271, 1959.

[20] H. Doleisch, M. Gasser, and H. Hauser. Interactive feature specification for focus+context visualization of complex simulation data. In *Proceedings of the*

5th Joint IEEE TCVG - EUROGRAPHICS Symposium on Visualization (VisSym 2003), pages 239–248, 2003.

[21] K. Engel, M. Hadwiger, J. M. Kniss, C. Rezk-Salama, and D. Weiskopf. *Real-Time Volume Graphics*. A K Peters, 2006.

[22] E. L. Etris, N. J. Crabtree, J. Dewar, and S. Pickford. True depth conversion: More than a pretty picture. *CSEG Recorder*, 26:11–22, 2001.

[23] G. Evensen. *Data Assimilation: The Ensemble Kalman Filter*. Springer, 2006.

[24] A. X. Falcão and J. K. Udupa. Segmentation of 3d objects using live wire. In *Medical Imaging 1997: Image Processing*, pages 228–235, 1997.

[25] A. X. Falcão, J. K. Udupa, S. Samarasekera, S. Sharma, B. E. Hirsch, and R. de Lotufo. User-steered image segmentation paradigms: Live wire and live lane. *Graphical Models and Image Processing*, 60(4):233–260, 1998.

[26] A. X. Falcão and K. J. Udupa. A 3d generalization of user-steered live-wire segmentation. *Medical Image Analysis*, 4(4):389–402, 2000.

[27] M. Faraklioti and M. Petrou. Horizon picking in 3d seismic data volumes. *Machine Vision and Applications*, 15:216–219, 2004.

[28] D. Gao. 3d seismic volume visualization and interpretation: An integrated workflow with case studies. *Geophysics*, 74(1):W1–W12, 2009.

[29] L. Grady. Computing exact discrete minimal surfaces: Extending and solving the shortest path problem in 3d with application to segmentation. In *IEEE Conference on Computer Vision and Pattern Recognition, 2006*, volume 1, pages 69–78, 2006.

[30] L. Grady. Minimal surfaces extend shortest path segmentation methods to 3d. *IEEE Transactions on Pattern Analysis and Machine Intelligence*, 32(2):321–334, 2010.

[31] H. Griethe and H. Schumann. The visualization of uncertain data: Methods and problems. In *Proceedings of SimVis '06*, 2006.

[32] G. Grigoryan and P. Rheingans. Point-based probabilistic surfaces to show surface uncertainty. *IEEE Transactions on Visualization and Computer Graphics*, 10(5):564–573, 2004.

[33] C. G. Healey and J. Snoeyink. VisTRE: A visualization tool to evaluate errors in terrain representation. In *3D Data Processing, Visualization, and Transmission, Third International Symposium on*, pages 1056–1063, 2006.

[34] J. L. Hintze and R. D. Nelson. Violin plots: A box plot-density trace synergism. *The American Statistician*, 52(2):181–184, 1998.

[35] T. Höllt, J. Beyer, F. Gschwantner, P. Muigg, H. Doleisch, G. Heinemann, and M. Hadwiger. Interactive seismic interpretation with piecewise global energy minimization. In *Proceedings of the IEEE Pacific Visualization Symposium 2011*, pages 59–66, 2011.

[36] T. Höllt, G. Chen, C. D. Hansen, and M. Hadwiger. Extraction and visual analysis of seismic horizon ensembles. *To appear in Proceedings of Eurographics 2013 Short Papers*, 2013.

[37] T. Höllt, W. Freiler, F. M. Gschwantner, H. Doleisch, G. Heinemann, and M. Hadwiger. SeiVis: An interactive visual subsurface modeling application. *IEEE Transactions on Visualization and Computer Graphics*, 18(12):2226–2235, 2012.

[38] T. Höllt, M. Hadwiger, L. Fritz, P. Muigg, and H. Doleisch. Seismic horizon tracing with diffusion tensors. Poster Presentation IEEE Visualization 2009, Atlantic City, NJ, 2009.

[39] T. Höllt, A. Magdy, G. Chen, G. Gopalakrishnan, I. Hoteit, C. D. Hansen, and M. Hadwiger. Visual analysis of uncertainties in ocean forecasts for planning and operation of off-shore structures. In *Proceedings of the IEEE Pacific Visualization Symposium 2013*, pages 59–66, 2013.

[40] I. Hoteit, T. Hoar, G. Gopalakrishnan, J. Anderson, N. Collins, B. Cornuelle, A. Kohl, and P. Heimbach. A MITgcm/DART ensemble analysis and prediction system with application to the gulf of mexico. *Dynamics of Atmospheres and Oceans*, 63:1–23, 2013.

[41] I. Hoteit, D. T. Pham, and J. Blum. A simplified reduced order kalman filtering and application to altimetric data assimilation in tropical pacific. *Journal of Marine Systems*, 36:101–127, 2002.

[42] W.-K. Jeong, R. Whitaker, and M. Dobin. Interactive 3d seismic fault detection on the graphics hardware. In *Eurographics / IEEE VGTC Workshop on Volume Graphics*, pages 111–118, 2006.

[43] C. R. Johnson and A. R. Sanderson. A next step: Visualizing errors and uncertainty. *IEEE Computer Graphics and Applications*, 23(5):6–10, 2003.

[44] B. J. Kadlec, G. A. Dorn, and H. M. Tufo. Confidence and curvature-guided level sets for channel segmentation. In *SEG Annual Meeting 2008*, pages 879–883, 2008.

[45] B. J. Kadlec, G. A. Dorn, and H. M. Tufo. Interactive visualization and interpretation of geologic surfaces in 3-d seismic data. In *SEG Annual Meeting 2009*, pages 1147–1151, 2009.

[46] B. J. Kadlec, H. M. Tufo, and G. A. Dorn. Knowledge-assisted visualization and segmentation of geologic features. *Computer Graphics and Applications*, 30(1):30–39, 2010.

[47] D. Kao, J. Dungan, and A. Pang. Visualizing 2d probability distributions from EOS satellite image-derived data sets: a case study. In *Proceedings of the conference on Visualization '01. VIS '01.*, pages 457–560, 2001.

[48] D. Kao, M. Kramer, A. Love, J. Dungan, and A. Pang. Visualizing distributions from multi-return lidar data to understand forest structure. In *In Geoinformatics, Gavle Sweden*, 2004.

[49] N. Keskes, P. Zaccagnino, D. Rether, and P. Mermey. Automatic extraction of 3-d seismic horizons. *SEG Technical Program Expanded Abstracts*, 2(1):557–559, 1983.

[50] G. Kidd. Fundamentals of 3d seismic volume visualization. In *Offshore Technology Conference*, 1999.

[51] O. D. Lampe, C. Correa, K.-L. Ma, and H. Hauser. Curve-centric volume reformation for comparative visualization. *IEEE Transactions on Visualization and Computer Graphics*, 15(6):1235–1242, 2009.

[52] P. Lavest and Y. Chipot. Building complex horizons for 3-d seismic. *SEG Technical Program Expanded Abstracts*, 12(1):159–161, 1993.

[53] M. Levoy. Display of surfaces from volume data. *IEEE Computer Graphics and Applications*, 8(3):29–37, may 1988.

[54] E. M. Lidal, H. Hauser, and I. Viola. Design principles for cutaway visualization of geological models. In *Proceedings of Spring Conference on Computer Graphics 2012*, pages 53–60, 2012.

[55] E. M. Lidal, T. Langeland, C. Giertsen, J. Grimsgaard, and R. Helland. A decade of increased oil recovery in virtual reality. *IEEE Computer Graphics and Applications*, 27:94–97, 2007.

[56] A. Love, A. Pang, and D. Kao. Visualizing spatial multivalue data. *IEEE Computer Graphics and Applications*, 25(3):69–79, 2005.

[57] C. Lundström, P. Ljung, A. Persson, and A. Ynnerman. Uncertainty visualization in medical volume rendering using probabilistic animation. *IEEE Transactions on Visualization and Computer Graphics*, 13(6):1648–1655, 2007.

[58] A. Luo, D. Kao, and A. Pang. Visualizing spatial distribution data sets. In *VISSYM '03: Proceedings of the Symposium on Data Visualisation 2003*, pages 29–38, 2003.

[59] W. R. Mark, R. S. Glanville, K. Akeley, and M. J. Kilgard. Cg: a system for programming graphics hardware in a C-like language. In *SIGGRAPH '03: ACM SIGGRAPH 2003 Papers*, pages 896–907, New York, NY, USA, 2003. ACM.

[60] J. Marshall, A. Adcroft, C. Hill, L. Perelman, and C. Heisey. A finite-volume, incompressible Navier Stokes model for studies of the ocean on parallel computers. *Journal of Geophysical Research*, 102:5735–5766, 1997.

[61] K. Matkovic, D. Gracanin, B. Klarin, and H. Hauser. Interactive visual analysis of complex scientific data as families of data surfaces. *IEEE Transactions on Visualization and Computer Graphics*, 15(6):1351–1358, 2009.

[62] M. J. McGuffin, L. Tancau, and R. Balakrishnan. Using deformations for browsing volumetric data. In *Proceedings of IEEE Visualization 2003*, pages 401–408, 2003.

[63] U. Meyer and P. Sanders. Δ-stepping: A parallel single source shortest path algorithm. In *Proceedings of the 6th Annual European Symposium on Algorithms, 1998*, pages 393–404, 1998.

[64] U. Meyer and P. Sanders. Δ-stepping: a parallelizable shortest path algorithm. *Journal of Algorithms*, 49(1):114–152, 2003.

[65] K. Moreland. Diverging color maps for scientific visualization. In *Proceedings of the 5th International Symposium on Visual Computing*, pages 92–103, 2009.

[66] E. N. Mortensen and W. A. Barrett. Intelligent scissors for image composition. In *SIGGRAPH '95: Proceedings of the 22nd Annual Conference on Computer Graphics and Interactive Techniques*, pages 191–198, 1995.

[67] E. N. Mortensen and W. A. Barrett. Interactive segmentation with intelligent scissors. *Graphical Models and Image Processing*, 60(5):349–384, 1998.

[68] E. N. Mortensen, B. Morse, W. A. Barrett, and J. K. Udupa. Adaptive boundary detection using 'live-wire' two-dimensional dynamic programming. In *Proceedings of Computers in Cardiology, 1992*, pages 635–638, 1992.

[69] NVIDIA Corporation. CUDA C programming guide version 5.0, 2012. Available online at `http://docs.nvidia.com/cuda/pdf/CUDA_C_Programming_Guide.pdf` (Mar. 08 2013).

[70] L. Oey, T. Ezer, and H. Lee. Loop current, rings and related circulation in the gulf of mexico: A review of numerical models and future challenges. *Geophysical Monograph-American Geophysical Union*, 161:31, 2005.

[71] S. Osher and N. Paragios. *Geometric Level Set Methods in Imaging,Vision,and Graphics*. Springer-Verlag New York, Inc., 2003.

[72] A. T. Pang, C. M. Wittenbrink, and S. K. Lodha. Approaches to uncertainty visualization. *The Visual Computer*, 13:370–390, 1997.

[73] D. Patel, S. Bruckner, I. Viola, and M. E. Gröller. Seismic volume visualization for horizon extraction. In *Proceedings of the IEEE Pacific Visualization Symposium 2010*, pages 73–80, 2010.

[74] D. Patel, C. Giertsen, J. Thurmond, J. Gjelberg, and M. E. Gröller. The seismic analyzer: Interpreting and illustrating 2d seismic data. *IEEE Transactions on Visualization and Computer Graphics*, 14(6):1571–1578, 2008.

[75] D. Patel, T. Höllt, and M. Hadwiger. *To appear in Novel Visualization Tools in Geoscience and Petroleum Engineering*. Springer-Verlag GmbH, 2013.

[76] D. Patel, Ø. Sture, H. Hauser, C. Giertsen, and M. E. Gröller. Knowledge-assisted visualization of seismic data. *Computers & Graphics*, 33(5):585–596, 2009.

[77] S. I. Pedersen, T. Skov, T. Randen, and L. Sønneland. Automatic fault extraction using artificial ants. In A. Iske and T. Randen, editors, *Mathematical Methods and Modelling in Hydrocarbon Exploration and Production*, volume 7 of *Mathematics in Industry*, pages 107–116. 2005.

[78] R. Pepper and G. Bejarano. Advances in seismic fault interpretation automation. *Search and Discovery Article 40170, Poster presentation at AAPG Annual Convention*, pages 19–22, 2005.

[79] P. Perona and J. Malik. Scale-space and edge detection using anisotropic diffusion. *IEEE Transactions on Pattern Analysis and Machine Intelligence*, 12(7):629–639, 1990.

[80] T. Pfaffelmoser, M. Reitinger, and R. Westermann. Visualizing the positional and geometrical variability of isosurfaces in uncertain scalar fields. *Computer Graphics Forum*, 30(3):951–960, 2011.

[81] T. Pfaffelmoser and R. Westermann. Visualization of global correlation structures in uncertain 2d scalar fields. *Computer Graphics Forum*, 31(3):1025–1034, 2012.

[82] D. T. Pham. Stochastic methods for sequential data assimilation in strongly nonlinear systems. *Monthly Weather Review*, 129:1194–1207, 2001.

[83] H. Piringer, S. Pajer, W. Berger, and H. Teichmann. Comparative visual analysis of 2d function ensembles. *Computer Graphics Forum*, 31(3):1195–1204, 2012.

[84] M. Poon, G. Hamarneh, and R. Abugharbieh. Live-vessel: Extending livewire for simultaneous extraction of optimal medial and boundary paths in vascular images. In *Lecture Notes in Computer Science, Medical Image Computing and Computer-Assisted Intervention (MICCAI)*, pages 444–451, 2007.

[85] M. Poon, G. Hamarneh, and R. Abugharbieh. Segmentation of complex objects with non-spherical topologies from volumetric medical images using 3d livewire. In *SPIE Medical Imaging*, volume 6512-31, pages 1–10, 2007.

[86] M. Poon, G. Hamarneh, and R. Abugharbieh. Efficient interactive 3d livewire segmentation of objects with arbitrary topology. *Computerized Medical Imaging and Graphics*, 32(8):639–650, 2008.

[87] K. Pöthkow and H.-C. Hege. Positional uncertainty of isocontours: Condition analysis and probabilistic measures. *IEEE Transactions on Visualization and Computer Graphics*, 17(10):1393–1406, 2011.

[88] K. Pöthkow, B. Weber, and H.-C. Hege. Probabilistic marching cubes. *Computer Graphics Forum*, 30(3):931–940, 2011.

[89] K. Potter, A. Wilson, P.-T. Bremer, D. Williams, C. Doutriaux, V. Pascucci, and C. R. Johhson. Ensemble-Vis: A framework for the statistical visualization of ensemble data. In *IEEE Workshop on Knowledge Discovery from Climate Data: Prediction, Extremes and Impacts*, pages 233–240, 2009.

[90] C. Rezk-Salama, M. Scheuering, G. Soza, and G. Greiner. Fast volumetric deformation on general purpose hardware. In *Proceedings of the ACM Siggraph/Eurographics Workshop On Graphics Hardware*, HWWS '01, pages 17–24, 2001.

[91] P. J. Rhodes, R. S. Laramee, R. D. Bergeron, and T. M. Sparr. Uncertainty visualization methods in isosurface rendering. In *EUROGRAPHICS 2003 Short Papers*, pages 83–88, 2003.

[92] M. Riveiro. Evaluation of uncertainty visualization techniques for information fusion. In *Information Fusion, 2007 10th International Conference on*, pages 1–8, 2007.

[93] T. Ropinski, J. Meyer-Spradow, S. Diepenbrock, J. Mensmann, and K. H. Hinrichs. Interactive volume rendering with dynamic ambient occlusion and color bleeding. *Computer Graphics Forum (Eurographics 2008)*, 27(2):567–576, 2008.

[94] T. Ropinski, F. Steinicke, and K. H. Hinrichs. Visual exploration of seismic volume datasets. *Journal Proceedings of the 14th International Conference in Central Europe on Computer Graphics, Visualization and Computer Vision (WSCG06)*, 14:73–80, 2006.

[95] M. Ruiz, I. Viola, I. Boada, S. Bruckner, M. Feixas, and M. Sbert. Similarity-based exploded views. In *Proceedings of 8th International Symposium on Smart Graphics*, pages 154–165, 2008.

[96] A. Saad, G. Hamarneh, and T. Möller. Exploration and visualization of segmentation uncertainty using shape and appearance prior information. *IEEE Transactions on Visualization and Computer Graphics*, 16(6):1366–1375, 2010.

[97] J. Sanyal, S. Zhang, J. Dyer, A. Mercer, P. Amburn, and R. J. Moorhead. Noodles: A tool for visualization of numerical weather model ensemble uncertainty. *IEEE Transactions on Visualization and Computer Graphics*, 16(6):1421 – 1430, 2010.

[98] H. Scharsach, M. Hadwiger, A. Neubauer, and K. Bühler. Perspective isosurface and direct volume rendering for virtual endoscopy applications. In *Eurovis 2006*, pages 315–322, 2006.

[99] A. Schenk, G. Prause, and H. O. Peitgen. Efficient semiautomatic segmentation of 3d objects in medical images. In *MICCAI '00: Proceedings of the Third International Conference on Medical Image Computing and Computer-Assisted Intervention*, pages 186–195, 2000.

[100] Schlumberger Information Solutions. Petrel seismic to simulation software. Available online at `http://www.slb.com/services/software/geo/petrel.aspx` (Mar. 08 2013).

[101] F. Schulze, K. Bühler, and M. Hadwiger. Direct volume deformation. In *Computer Vision and Computer Graphics. Theory and Applications*, volume 21 of *Communications in Computer and Information Science*, pages 59–72. 2009.

[102] P. M. Silva, M. Machado, and M. Gattass. 3d seismic volume rendering. In *Eighth International Congress of The Brazilian Geophysical Society*, pages 181–193, 2003.

[103] P. Tu, A. Zisserman, I. Mason, and I. Cox. Identification of events from 3d volumes of seismic data. In *IEEE International Conference on Image Processing, ICIP '94*, volume 3, pages 309–313, 1994.

[104] U.S. Energy Information Administration. International energy outlook 2010, 2010.

[105] U.S. Geological Survey. Earthquake glossary, 2013. Available online at `http://earthquake.usgs.gov/learn/glossary/` (Mar. 08 2013).

[106] vsg Visualizaton Sciences Group. Avizo earth. Available online at `http://www.vsg3d.com/avizo/earth` (Mar. 08 2013).

[107] V. Šoltészová, D. Patel, and I. Viola. Chromatic shadows for improved perception. In *Proceedings of Non-photorealistic Animation and Rendering 2011*, pages 105–115, 2011.

[108] F. M. Vukovich. An updated evaluation of the loop current's eddy-shedding frequency. *Journal of Geophysical Research*, 100:8655–8659, 1995.

[109] J. Weickert. *Anisotropic Diffusion in Image Processing*. PhD thesis, University of Kaiserslautern, 1996.

[110] R. Westermann and C. Rezk-Salama. Real-time volume deformations. *Computer Graphics Forum*, 20(3):443–451, 2001.

[111] C. Wunsch. *The Ocean Circulation Inverse Problem.* Cambridge University Press, 1996.

APPENDICES

A Publications Relevant to this Dissertation.

- Daniel Patel, Thomas Höllt, and Markus Hadwiger, **Real-Time Algorithms for Visualizing and Segmenting Seismic Data**, in *Novel Visualization Tools in Geoscience and Petroleum Engineering*, Springer-Verlag GmbH, to appear, 2013.
- Thomas Höllt, Guoning Chen, Charles D. Hansen, and Markus Hadwiger, **Extraction and Visual Analysis of Seismic Horizon Ensembles**, *Proceedings of Eurographics 2013 Short Papers*, to appear, 2013.
- Thomas Höllt, Ahmed Magdy, Guoning Chen, Ganesh Gopalakrishnan, Ibrahim Hoteit, Charles D. Hansen, and Markus Hadwiger, **Visual Analysis of Uncertainties in Ocean Forecasts for Planning and Operation of Off-Shore Structures**, *Proceedings of IEEE Pacific Visualization 2013*, pp. 185–192, 2013. **Honorable mention for best paper award.**
- Thomas Höllt, Wolfgang Freiler, Fritz Gschwantner, Helmut Doleisch, Gabor Heinemann, and Markus Hadwiger, **SeiVis: An Interactive Visual Subsurface Modeling Application**, *IEEE Transactions on Visualization and Computer Graphics*, 18(12) (Proceedings IEEE Scientific Visualization 2012); pp. 2226–2235, 2012.
- Thomas Höllt, Johanna Beyer, Fritz Gschwantner, Philipp Muigg, Helmut Doleisch, Gabor Heinemann, and Markus Hadwiger, **Interactive Seismic Interpretation with Piecewise Global Energy Minimization**, *Proceedings of IEEE Pacific Visualization 2011*, pp. 59–66, 2011.

• Thomas Höllt, Markus Hadwiger, Laura Fritz, Philipp Muigg, and Helmut Doleisch, **Seismic Horizon Tracing with Diffusion Tensors**, *Poster Presentation IEEE Visualization 2009, Atlantic City, NJ*, 2009.

B Other Publications.

- Mathias Schott, Tobias Martin, A.V. Pascal Grosset, Carson Brownlee, Thomas Höllt, Benjamin P. Brown, Sean T. Smith, and Charles D. Hansen, **Combined Surface and Volumetric Occlusion Shading**, *Proceedings of IEEE Pacific Visualization 2012*, pp. 169–176 2012.
- Georg Geier, Thomas Pabel, Daniel Habe, Jördis Rosc, Markus Hadwiger, Thomas Höllt, and Laura Fritz, **Computertomographie als zerstörungsfreies Prüfverfahren für Gussteile**, *Druckguss*, 7(8), pp. 171–174, 2010.
- Markus Hadwiger, Laura Fritz, Christof Rezk-Salama, Thomas Höllt, Georg Geier, and Thomas Pabel, **Interactive Volume Exploration for Feature Detection and Quantification in Industrial CT Data**, *IEEE Transactions on Visualization and Computer Graphics*, 14(6) (Proceedings IEEE Visualization 2008); pp. 1507–1514, 2008.
- Georg Geier, Markus Hadwiger, Thomas Höllt, Laura Fritz, and Thomas Pabel, **Interaktive Exploration und Quantifizierung von Ungänzen in komplexen Bauteilen**, *Proceedings of Industrielle Computertomografie (CT Tagung Wels)*, pp. 103–108, 2008.